

A STUDY OF THE GLOBAL EVOLUTION  
OF MICROSTRUCTURES

By

ARUN MAHADEO GOKHALE

A DISSERTATION PRESENTED TO THE GRADUATE COUNCIL OF  
THE UNIVERSITY OF FLORIDA  
IN PARTIAL FULFILLMENT OF THE REQUIREMENTS FOR THE  
DEGREE OF DOCTOR OF PHILOSOPHY

UNIVERSITY OF FLORIDA

1977

Copyright by

Arun Mahadeo Gokhale

1977

To Aai and Dada

## ACKNOWLEDGMENTS

I would like to thank my supervisory committee members for their guidance and encouragement during this work. Appreciation is extended to Professor A. G. Guy for some very useful discussions. I would like to thank my wife, Sulu, for her patience and encouragement during this work. The financial support of The National Science Foundation during most of this work is gratefully acknowledged.

## TABLE OF CONTENTS

	<u>Page</u>
ACKNOWLEDGMENTS	iii
ABSTRACT	viii
CHAPTER I	
PROBLEM FORMULATION	1
CHAPTER II	
STEREOLOGICAL METHODS	5
2.1 Introduction	5
2.2 Measurement of Global Properties	6
2.2.1 Measurement of Volume Fraction	6
2.2.2 Measurement of Surface Area per Unit Volume	7
2.2.3 Total Curvature	8
2.2.4 Measurement of the Geometrical Properties of Lineal Features	10
2.3 Measurement of Particle Size Distribution	10
2.3.1 Techniques Based on the Measurement of Section Size Distribution	11
2.3.2 Distribution of Particle Sizes from the Distribution of Section Areas	13
2.3.3 Evaluation of P.S.D. from the Distribution of Linear Intercepts	13
2.4 Evolution of Particle Size Distributions	14
2.5 Derived Properties	18
CHAPTER III	
THEORETICAL DEVELOPMENT	20
3.1 Evolution of Particle Size Distributions	21
3.2 Calculation of the Extended Global Properties from the Kinetic Models	26
3.3 Evaluation of the Nucleation Rate and Growth Rate from the Global Properties	34

## Table of Contents - continued.

	<u>Page</u>
3.4 Growth Geometry	40
3.4.1 Shape Preserving Growth	40
3.4.2 Two Dimensional Growth	42
3.4.3 One Dimensional Growth	45
3.5 The Impingement Problem	47
3.5.1 Non-random Impingement	53
3.5.2 A Phenomenological Approach to Non-Random Impingement	55
3.6 Conclusions	57
CHAPTER IV	
RECRYSTALLIZATION	59
4.1 Introduction	59
4.2 The Experimental Work of Speich and Fisher [79]	60
4.2.1 Experimental Observations	61
4.2.2 Speich and Fisher's Interpretation of Their Data	62
4.3 Reanalysis of Speich and Fisher's Data	63
4.4 The Experimental Work of English and Backofen [92]	68
4.5 Reanalysis of English and Backofen's Data	69
CHAPTER V	
NUCLEATION AND GROWTH OF AUSTENITE FROM PEARLITE	82
5.1 Introduction	82
5.2 Literature Survey	82
5.3 Experimental Work	85
5.3.1 Starting Structure for the Austenitization Studies	86
5.3.2 Austenitization Experiments	86
5.4 Metallography	87
5.5 Data Processing	91
5.6 Data Analysis	99
5.7 Conclusions	108

Table of Contents - continued.

	<u>Page</u>
CHAPTER VI	
FORMATION OF AUSTENITE FROM "SPHERODIZED" CEMENTITE AND FERRITE AGGREGATES	
6.1 Introduction	109
6.2 Literature Survey	109
6.3 Experimental Work	110
6.3.1 Starting Structure	113
6.3.2 Austenitizing Experiments	114
6.3.3 Metallography	114
6.4 Data Processing	147
6.4.1 Data Processing of the Detailed Quantitative Microscopic Measure- ments Made on the D <sub>3</sub> Samples Austenitized at 750°C	171
6.5 Data Analysis	174
6.5.1 Analysis of the Global Properties of Austenite	183
6.6 Conclusions	197
CHAPTER VII	
CONCLUSIONS AND SUMMARY	200
BIBLIOGRAPHY	203
BIOGRAPHICAL SKETCH	211

Abstract of Dissertation Presented to the Graduate Council  
of the University of Florida in Partial Fulfillment  
of the Requirements for the Degree of Doctor of Philosophy

A STUDY OF THE GLOBAL EVOLUTION  
OF MICROSTRUCTURES

By

Arun Mahadeo Gokhale

March, 1977

Chairman: R. T. DeHoff

Major Department: Materials Science and Engineering

Mechanical and physical properties of crystalline materials depend on the geometrical properties of their microstructures. Thus, an understanding of the processes by which microstructures evolve is of great significance. In many cases, theoretical and experimental studies on the physics of microstructural evolution are done on a "local" basis. On the other hand, the experimental techniques of Stereology usually yield the "global" or average geometrical properties of microstructures. Thus, there is a need to bridge the gap between the local and the global description of the evolution of microstructures. This is the major objective of this dissertation.

An approach has been developed to evaluate the global



geometrical properties of an evolving microstructure from a given description of the local variables. Effects of various growth geometries on the kinematics of phase transformations have been explored in detail. A phenomenological approach is developed to evaluate the impingement equations for two and one dimensional growth geometries. This phenomenological approach is valid for both random and non-random impingements. A fairly general technique is developed to deduce the nucleation rate and growth rate from the time variation of the global properties.

The practical feasibility of the approach is demonstrated by applying it to the experimental data on recrystallization and austenitization processes. The analysis is used to deduce the nucleation rate and growth rate of austenite, during the austenitization of a pearlitic structure. It is concluded that the nucleation rate and growth rate of austenite remain constant at a given temperature during austenitization of pearlitic structures.

The kinetics of austenitization of some "spherodized" cementite structures is studied in detail. It is concluded that the "spherodized" cementite is present in the form of an incomplete grain edge network, which dissolves

in a one dimensional manner during the austenitization process. The austenite grains grow along the ferrite grain boundaries in a two dimensional manner. The present approach is successfully applied to explain the experimentally observed behavior of nine independent stereological properties.

## CHAPTER I PROBLEM FORMULATION

The properties of materials are to a large extent determined by their "structure." In crystalline materials, atoms or molecules of the constituents are arranged in a periodic array in space. This gives rise to crystal structure. The same material in two crystalline forms may have very different properties. On a coarser level, the structure is classified in terms of heterogeneity of its individual crystals or grains. Heterogeneity arises because more than one crystal may nucleate and grow when a material crystallizes or transforms from one crystalline form to another. This gives rise to microstructure. Mechanical and physical properties of materials depend on the geometrical properties of their microstructures. For example, yield stress varies linearly with the square root of the mean grain intercept [1]. It may be said that control of microstructure would lead to the control or optimization of some property or a set of properties. In order to control microstructures, it is necessary to control the processes by which microstructural changes occur. Thus the understanding of the processes by which microstructures evolve is of great significance.

In many cases, theoretical and experimental studies on the physics of microstructural evolution are done on a "local" basis. For example, diffusion controlled growth of a precipitate is described in terms of the local interface velocity or local growth rate. These theoretical models describe how a microstructure evolves locally [2-11]. On the other hand, quantitative structure-property correlations are usually obtained through the "global" or average properties of microstructures. Furthermore, the experimental techniques of quantitative microscopy usually yield only the global or average geometrical properties of microstructure. Thus, there is a need to bridge the gap between the local and the global description of the evolution of microstructures. This is the major objective of this thesis.

The "local" variables and the kinetic variables which affect the "global" geometrical properties of a microstructure, during and at the end of a phase transformation or a redistribution process, are as follows:

- (1) Nucleation rate
- (2) Growth or shrinkage rate
- (3) Particle shape
- (4) Growth or shrinkage geometry

In addition to these local and kinetic variables, the

global microstructural evolution is determined by the following variables:

(5) Starting microstructure

(6) Distribution of nuclei in space

The answers to the following questions provide the solution to the problem.

(A) If a quantitative description of these six variables is given, how are the geometrical global properties of a microstructure during its evolution evaluated?

(B) Given some global geometrical properties of microstructure at different times during a phase transformation or a redistribution process, how to evaluate the local variables?

An attempt will be made to answer these two questions in the third chapter of this thesis. However, some physically acceptable simplifying assumptions will be made to solve the problem. This, then, leads to the following question:

(C) Is such an approach practically feasible?

In order to demonstrate the feasibility of the approach, it will be applied to the experimental data on the recrystallization and austenitization processes. The fourth chapter deals with the interpretation of the experimental data on the recrystallization in some Fe-Si

alloys. The fifth chapter deals with the experimental measurements of the global properties of austenite during the austenitization of pearlite and the evaluation of the local variables from the time variation of the global properties of austenite. The sixth chapter is concerned with a detailed quantitative microscopic investigation of the austenitization of spherodized cementite structures. The present approach will be successfully applied to interpret the experimental data.

## CHAPTER II STEREOLOGICAL METHODS

### 2.1 Introduction:

In virtually every branch of science, there exists an interest in the quantitative characterization of structures that appear in nature. The method of observation of such structures always involves some biased sampling technique. For example, observation of a microstructure with an optical microscope presents a two dimensional section through the three dimensional structure contained in the sample. Measurements made upon such a two dimensional section are related to the geometry of the three dimensional structure which they represent. The process of quantitative evaluation of some properties of the three dimensional microstructure is called "Quantitative microscopy" or "Stereology." Apart from Metallurgy, quantitative microscopic techniques are used in a variety of fields such as Geology [12,13], Biological Sciences [14, 15], Ceramics [16], Concrete technology [17], Wood technology [18], etc. What follows is primarily a catalog of the basic relationships of quantitative microstructural analysis.

## 2.2 Measurement of Global Properties:

The global properties of a microstructure are classified into two categories, namely, metric and topological properties. The metric properties (for example, volume, surface area, etc.) can be evaluated from the measurements made on a two dimensional section, whereas the topological properties can not be evaluated from such measurements without making any simplifying assumptions. A serial sectioning of the structure is necessary for evaluating the topological properties of an opaque body. The metric properties describe the numerical extent of a particular feature in the structure. Each three, two and one dimensional feature in the structure has associated with it, respectively, volume, area and length, which can be measured unambiguously from the plane of polish. The procedure for such measurements will now be described briefly.

### 2.2.1 Measurement of Volume Fraction

The volume fraction of a particular phase in the structure can be measured by using areal analysis [19-24], linear analysis [20-22,24-26] or point counting [20,27]. The basic principles involved in these three methods are as follows.



Areal analysis: The expected value of the area fraction of a particular phase measured on the plane of polish is identically equal to its volume fraction in the three dimensional structure.

Lineal analysis: Suppose a number of test lines are superimposed on the plane of polish; then the expected value of the fraction of length of the test lines contained in a particular phase is identically equal to its volume fraction.

Point counting: If a point is placed at random on a random plane of polish, then the probability of the point falling within a particular phase is equal to the volume fraction of that phase.

A detailed analysis of these three techniques is given by DeHoff and Rhines [20] and Underwood [26] and will not be repeated here.

### 2.2.2 Measurement of Surface Area per Unit Volume

A statistically exact relationship for the evaluation of interfacial area per unit volume,  $S_V$ , was first developed by Saltykov [22] in 1945 and later by Smith and Guttman [28]. Alternative derivations are given by Underwood [26] and DeHoff and Rhines [20]. Suppose a number of test lines are superimposed on the plane of

polish. Let 'L' be the total length of these test lines and 'N' be the number of intersections of these test lines with a particular type of interface (e.g. grain boundaries, particle-matrix interface, etc.), then the surface area per unit volume,  $S_V$ , of that interface is given by

$$S_V = 2 \cdot \text{Expected value}\{N_L\} \quad (2.1)$$

where  $N_L = N/L$

If directional anisotropy exists in the structure, then different orientations of the test lines will give different values of  $S_V$ . This concept was used by Hilliard [29,30] in his treatment of oriented structures.

### 2.2.3 Total Curvature

Consider a small surface element,  $dS$ , of an arbitrarily curved surface. The local mean curvature,  $H$ , of this surface element is given by [31]

$$H = \frac{1}{2}[K_1 + K_2] \quad (2.2)$$

where  $K_1$  and  $K_2$  are the principal normal curvatures.

The total curvature,  $M_V$ , of a given type of interface per unit volume of the structure is given by

$$M_V = \iint_{S_V} H \, dS \quad (2.3)$$

where the integration is carried out over all the surface elements, of the interface under consideration, in a unit

volume of the structure. For a system of discrete convex particles, the total curvature is proportional to the first moment of the size distribution function.

DeHoff [32] has shown that for a tubule network, the total curvature is proportional to the length of the network. The total curvature of surfaces can be measured quantitatively by using the sampling procedure devised by Rhines [33] called the area tangent count. It was independently shown by DeHoff [34] and Cahn [35] that the total curvature of an interface is given by

$$\begin{aligned} M_V &= \pi \cdot \text{Expected value}\{(T_A)_{\text{net}}\} \\ &= 2\pi \cdot \text{Expected value}\{(N_A)_{\text{net}}\} \end{aligned} \quad (2.4)$$

$(T_A)_{\text{net}}$  is the net number of tangents per unit area formed by a random sweeping test line with the traces of the surfaces on the plane of polish. Tangents produced with the elements of traces of the surface that are convex with respect to the phase of interest are counted as positive and those produced with the concave elements are counted as negative.  $(N_A)_{\text{net}}$  is the net number of closed area loops per unit area of the plane of polish. Loops which enclose phases other than the phase of interest are counted as negative.

#### 2.2.4 Measurement of the Geometrical Properties of Lineal Features

The length of a lineal feature per unit volume of the structure,  $L_V$ , can be evaluated by using the following stereological relationship [22,28]:

$$L_V = 2 \cdot \text{Expected value}\{P_A\} \quad (2.5)$$

where  $P_A$  is the number of intersections of the lineal feature with the unit area of plane of polish.

DeHoff [36] has shown that the total curvature of an edge is given by the following expression:

$$[M_V]_{\text{edge}} = \frac{1}{2} \int_{L_V} \chi \, d\ell \quad (2.6)$$

The integration is carried out over the length of the edge in the unit volume of the structure and ' $\chi$ ' is the local dihedral angle. DeHoff and Gehl [45] have shown that the average dihedral angle,  $\bar{\chi}$ , is given by

$$\bar{\chi} = \frac{2(M_V)_{\text{edge}}}{(L_V)_{\text{edge}}} = \frac{2\pi(T_A)_{\text{edge}}}{(L_V)_{\text{edge}}} \quad (2.7)$$

where  $(T_A)_{\text{edge}}$  is obtained by applying the area tangent count [33] only to the edges. The problem of the measurement of average dihedral angle has been also analyzed by Harker and Parker [37].

#### 2.3 Measurement of Particle Size Distribution:

A particle size distribution can be evaluated from

the measurements made on the plane of polish if some simplifying assumptions are made regarding the particle shape. The techniques for the measurement of particle size distribution (henceforth called P.S.D.) assume a model shape for all the particles, and require a measurement of the distribution of some geometrical variable (e.g. linear intercepts, section sizes, etc.) on the plane of polish. This distribution function is then converted into the three dimensional P.S.D. by using the principles of geometrical probabilities.

### 2.3.1 Techniques Based on the Measurement of Section Size Distribution

Wicksell [38], Scheil [39,40], Schwartz [41] and Saltykov [22] have developed methods for evaluation of P.S.D. of spherical particles from the distribution of their section sizes. Saltykov's method [22] is more convenient and involves less computational errors. Excellent review articles on the subject are given by DeHoff and Rhines [20] and Underwood [26].

All these methods are essentially numerical solutions to the following integral equation [20]:

$$n_A(r) = r \int_r^{\infty} \frac{n_V(R) dR}{[R^2 - r^2]^{1/2}} \quad (2.8)$$

where  $n_A(r)$  is the section size distribution function and

$n_V(R)$  is the three dimensional P.S.D. An analytical solution to this integral equation is as follows:

$$N_{V>}(R) = \frac{1}{\pi} \int_R^{\infty} \frac{n_A(r) dr}{[r^2 - R^2]^{1/2}} \quad (2.9)$$

where

$$N_{V>}(R) = \int_R^{\infty} n_V(R) dR \quad (2.9a)$$

The direct use of equation (2.9) requires an analytical form for the section size distribution and furthermore one has to evaluate a derivative if the three dimensional P.S.D.,  $n_V(R)$ , is desired instead of  $N_{V>}(R)$ . Due to these limitations, the numerical solutions [38-41,22] to equation (2.8) are normally used.

In the general case of ellipsoids of revolution, with either prolate or oblate shape, integral equations similar to equation (2.8) can be set up [46]. DeHoff [43] has given a solution to this problem for ellipsoids of revolution. Recently Cruz-Orive [44] has shown that if there are oblate or prolate ellipsoids with a shape and size distribution then the bivariant three dimensional P.S.D. is related to the corresponding bivariant section size distribution through a double Abelian integral equation. Cruz-Orive [44] has also proved that if there is a mixture of oblate and prolate ellipsoids then the problem does not have a unique solution.

### 2.3.2 Distribution of Particle Sizes from the Distribution of Section Areas

Johnson [47] and Saltykov [22] have given algorithms for the evaluation of P.S.D. from the distribution of section areas. Both Johnson [47] and Saltykov [22] assume that the particles are of spherical shape. Recently, Lewis, Walters and Johnson [48] have extended and modified Saltykov's method. Lewis, Walters and Johnson [48] have presented an algorithm for a numerical solution to the general problem where the size class interval need not be constant and the particles need to be of the same shape only within a given size class. This is an excellent method for the evaluation of P.S.D., where the particle shape may be a direct function of its size.

### 2.3.3 Evaluation of P.S.D. from the Distribution of Linear Intercepts

It is possible to evaluate the P.S.D. of spheres from the distribution of their linear intercepts by using the methods developed by Spektor [49], Lord and Wills [17] and Cahn and Fullman [50]. DeHoff and Bousquet [51] have extended Cahn and Fullman's analysis [50] to triaxial ellipsoids of constant shape. Their results are summarized in the following equation:

$$n_V(\ell) = -\frac{d}{d\ell} \left[ \frac{n_L(\ell)}{K\ell} \right] \quad (2.10)$$

where  $n_L(\ell)$  is the linear intercept distribution function and  $n_V(\ell)$  is the three dimensional P.S.D. function. The shape factor,  $K$ , can be evaluated by the method given by DeHoff and Bousquet [51]. For spherical particles,  $K$  is equal to  $2/\pi$ . DeHoff and Bousquet [51] have developed an expression similar to this equation for oriented structures.

Exner and Lucas [52] have given a general formula for the calculation of the distribution of linear intercepts from a given P.S.D. function for particles of any shape, as long as all the particles are of the same shape (there is a typographical error in the formula given by Exner and Lucas). The input information required is the P.S.D. function and the distribution of intercept lengths for one particle. The expressions for the distribution of intercept lengths of one particle are available for the cube [53], sphere [54], cylinder [55] and ellipsoid [51]. Thus, if the formula given by Exner and Lucas [52] can be inverted then it will give a quite general solution for the evaluation of P.S.D. from the distribution of linear intercepts.

#### 2.4 Evolution of Particle Size Distributions:

The evolution of microstructural state of a given



particle is described by its growth path. In a simple case where the geometry of the particle can be completely described by one characteristic dimension, the growth path is simply the graph of particle size against time. If the growth paths of different particles do not cross, then the number of particles which are larger than a given particle will not change with time. Thus the number of particles larger than a given particle is equal to the particles that existed before the nucleation of this particle. The factor which identifies particles belonging to the same growth path, in a sequence of size distribution of an evolving structure, is that the  $N_{V>}(R,t)$  function [see equation (2.9a)] is constant. This basic principle was first used by Spektor [66] to evaluate the growth rate of carbides during the coarsening process. Lifshitz and Slyozov [62] and Markworth [63] used this principle in the theoretical analysis of the coarsening process. The systematic development of the formalism was first carried out by Woodhead [57] and later by DeHoff [58]. Woodhead's analysis [57] was used by Mukherjee et al. [61] in their experimental studies of particle coarsening.\* DeHoff [58]

\*Heckel and Degregrio [59] have used similar analysis to evaluate the growth rates of carbide particles during spheroidization process.

showed that

$$n_V(R, t) = -\dot{N}(\tau) \cdot \left(\frac{\partial \tau}{\partial R}\right)_t \quad (2.11)$$

where  $\tau$  is the nucleation of the particle whose size is  $R$  at time  $t$  and  $\dot{N}(\tau)$  is the nucleation rate at time  $\tau$ .

If the growth rate can be described by the functional form

$$(\text{Growth rate}) = \left(\frac{\partial R}{\partial t}\right)_\tau = f(R) \cdot g(t) \quad (2.12)$$

then equation (2.11) becomes

$$n_V(R, t) = \frac{\dot{N}(\tau)}{f(R) \cdot g(\tau)} \quad (2.13)$$

Equation (2.13) was first derived by DeHoff [58].

Recently Yost [64] has shown that equation (2.11) is a general solution to the continuity equation [62] for non-crossing growth paths.

The global properties of the structure can be evaluated from a model for nucleation rate and growth rate by using equation (2.11). For example, the volume fraction of the transformed phase is given by the following expression:

$$V_{V_{ex}}(t) = \int_0^{R_m} V(R) n_V(R, t) dR \quad (2.14)$$

where  $V(R)$  is the volume of a particle of size  $R$  and  $R_m$  is the maximum particle size. For a given model for the

nucleation rate and growth rate, one can evaluate  $n_V(R,t)$  at any time  $t$  during the transformation by using equation (2.11) and then equation (2.14) can be used to evaluate the volume fraction. The volume fraction evaluated in this manner is the extended volume fraction [the subscript "ex" on  $V_V$  in equation (2.14) signifies this fact] and it can not be compared directly with the experimental values. The calculation completely ignores the geometrical impingement between the growing particles. The impingement correction becomes increasingly important as the volume fraction increases. If the spatial distribution of the particles is random, then the following expressions can be used to convert the extended properties to their real values:

$$V_V = 1 - \text{Exp}(-V_{V_{\text{ex}}}) \quad (2.15)$$

$$S_V = (1 - V_V) S_{V_{\text{ex}}} \quad (2.16)$$

$$M_V = (1 - V_V) \left[ M_{V_{\text{ex}}} - \frac{1}{2} \frac{(\bar{v}_S)_{\text{ex}}}{(\bar{v}_H)_{\text{ex}}} S_{V_{\text{ex}}}^2 \right] \quad (2.16a)$$

where  $V_{V_{\text{ex}}}$ ,  $S_{V_{\text{ex}}}$  and  $M_{V_{\text{ex}}}$  are the extended volume fraction, surface area and total curvature calculated from a model and  $V_V$ ,  $S_V$  and  $M_V$  are their corresponding real values. The quantities  $(\bar{v}_S)_{\text{ex}}$  and  $(\bar{v}_H)_{\text{ex}}$  will be defined

in the next section. Equation (2.15) was first proposed by Kolmogorov [69] and later by Avrami [70] and Johnson and Mehl [71]. DeHoff [67] has derived equations (2.16) and (2.16a). Recently Serra [72] has derived these equations by using a Boolean scheme. An alternative derivation of equations (2.15) and (2.16) will be given in the next chapter.

## 2.5 Derived Properties:

Spektor [65] in 1949 showed that the surface area averaged interface velocity,  $\bar{v}_S$ , is given by the following equation:

$$\bar{v}_S = \frac{\int \int v dS}{\int \int dS} = \frac{1}{S_V} \frac{d V_V}{d\tau} \quad (2.17)$$

where  $v$  is the local interface velocity of a surface element  $dS$ . Cahn and Hagel [73] rederived this equation in 1963.

DeHoff [67] has shown that if the local interface velocity is averaged over the total curvature of the surface elements, then the resultant total curvature averaged interface velocity  $\bar{v}_H$  is given by

$$\bar{v}_H = \frac{\int \int v H dS}{\int \int H dS} = \frac{1}{2 M_V} \frac{d S_V}{d\tau} \quad (2.18)$$

In general,  $\bar{v}_S$  and  $\bar{v}_H$  are expected to have different values.

In addition to the interface velocity averages, it is possible to evaluate some other "average" properties from the global properties of a microstructure. The mean curvature,  $\bar{H}$ , of a phase is given by [34,35]

$$\bar{H} = \frac{\iint H dS}{\iint dS} = \frac{M_V}{S_V} \quad (2.19)$$

where  $H$  is the local mean curvature of a surface element  $dS$ .

For a system of discrete particles, the mean intercept  $\bar{\lambda}$  of the particulate phase is given by the following expression [74]:

$$\bar{\lambda} = \frac{4 V_V}{S_V} \quad (2.20)$$

where  $V_V$  and  $S_V$  are the volume fraction and surface area of the particles.

This completes the description of important stereological methods. The next chapter deals with the theoretical analysis developed during the present work.

### CHAPTER III THEORETICAL DEVELOPMENT

The geometrical properties of an evolving microstructure are determined by the following variables:

- (1) Starting microstructure
- (2) Spatial distribution of nuclei
- (3) Nucleation rate
- (4) Growth rate or shrinkage rate
- (5) Particle shape
- (6) Growth or shrinkage geometry

An attempt will now be made to answer the following questions:

(A) If a quantitative description of the above variables is given, how to evaluate the global properties of a microstructure?

(B) Given some global geometrical properties of microstructure at different times during a phase transformation, how to evaluate the local growth rate or shrinkage rate and the nucleation rate?

The first section deals with the analysis of particulate structures. More complicated microstructures and the impingement problem, etc. will be analyzed in the subsequent sections.

### 3.1 Evolution of Particle Size Distributions:

Consider an evolving distribution of discrete particles in a matrix. The particles can appear or disappear only at zero size. The mathematical statement of this condition is called the "continuity equation." Any size distribution function must obey the continuity equation. The continuity equation, as it is given in the literature [62,64,75] is valid only if the growth paths do not cross and it is given as follows:

$$\frac{\partial n_V(R,t)}{\partial t} + \frac{\partial}{\partial R} \{ n_V(R,t) \left( \frac{\partial R}{\partial t} \right)_\tau \} = 0 \quad (3.1)$$

A generalized continuity equation will now be derived.

Let us define [see equation (2.9a)]

$$N_{V>}(R,t) = \int_R^{R_m} n_V(R,t) dR \quad (3.2)$$

where  $R_m$  is the maximum particle size at time  $t$ . It follows that

$$\left( \frac{\partial N_{V>}(R,t)}{\partial R} \right)_t = -n_V(R,t) \quad (3.3)$$

Since the discrete particles can appear or disappear only at zero size, the function  $N_{V>}(R,t)$  is continuous in both  $R$  and  $t$  for  $t > 0$ . Thus,

$$\left( \frac{\partial N_{V>}(R,t)}{\partial R} \right)_R = - \left( \frac{\partial N_{V>}(R,t)}{\partial R} \right)_t \cdot \left( \frac{\partial R}{\partial t} \right)_{N_{V>}} \quad (3.4)$$

Substituting equation (3.3) into (3.4) and operating on the resulting equation by  $(\frac{\partial}{\partial R})_t$  leads to the following equation:

$$\frac{\partial}{\partial R} \left\{ \frac{\partial N_{V>}(R, t)}{\partial t} \right\} = \frac{\partial}{\partial R} \{ n_V(R, t) \cdot (\frac{\partial R}{\partial t})_{N_{V>}} \} \quad (3.5)$$

Reversing the order of differentiation on the left-hand side of this equation and again substituting equation (3.3) into the resulting equation gives the following expression:

$$\frac{\partial n_V(R, t)}{\partial t} + \frac{\partial}{\partial R} \{ n_V(R, t) \cdot (\frac{\partial R}{\partial t})_{N_{V>}} \} = 0 \quad (3.6)$$

DeHoff [58] has shown that, for the non-crossing growth paths,  $(\frac{\partial R}{\partial t})_t = (\frac{\partial R}{\partial t})_{N_{V>}}$ . Thus, for non-crossing growth paths, equation (3.6) reduces to the equation (3.1). However, if the growth paths do cross, then equation (3.6) must be used. In order to solve the problem of crossing growth paths, it is necessary to formulate  $(\partial R / \partial t)_{N_{V>}}$  in terms of the local growth rates and then solve equation (3.6) for  $n_V(R, t)$ .

For a system of discrete particles in a matrix, one can use the method developed by Woodhead [57] and DeHoff [58] to evaluate the growth rate or shrinkage rate of the particles if the size distribution is measured at different times during the evolution of such a structure.



Furthermore, one can use equation (2.11) to calculate the particle size distributions from a model. These calculated size distributions can then be directly compared with the experimental distributions to check the model. However, equation (2.11) can not be used for a dissolution process. A formalism will now be developed for the prediction of the particle size distributions during a dissolution process.

Let  $\phi_V(\xi)$  be the initial size distribution function. Thus, the  $\xi$  values represent the initial particle sizes which exist in the system. Let  $n_V(R, t)$  be the size distribution function at time  $t$  during the dissolution process. If the dissolution paths do not cross, then

$$\int_R^{R_m} n_V(R, t) dR = \int_{\xi[R, t]}^{\xi_m} \phi_V(\xi) d\xi \quad (3.7)$$

where  $\xi_m$  is the maximum particle size in the starting structure. Operating on the above equation by  $(\frac{\partial}{\partial R})_t$  gives

$$n_V(R, t) = \phi_V[\xi(R, t)] \left[ \frac{\partial \xi(R, t)}{\partial R} \right]_t \quad (3.8)$$

where  $\xi(R, t)$  is the size of the particle in the initial structure, whose size is  $R$  at time  $t$ . If the shrinkage rate can be modeled by the following functional form,

$$\left( \frac{\partial R}{\partial t} \right)_\xi = f(R) \cdot g(t) \quad (3.9)$$

then it can be shown that

$$\left(\frac{\partial \xi(R, t)}{\partial R}\right)_t = \frac{f(\xi)}{f(R)} \quad (3.10)$$

Combining equations (3.8) and (3.10) gives

$$n_V(R, t) = \frac{\phi_V[\xi(R, t)] \cdot f(\xi)}{f(R)} \quad (3.11)$$

It is possible to derive an expression for the annihilation rate. Suppose the particle which just disappeared at time  $t$  had a size  $\xi_0(t)$  in the initial distribution. For non-crossing dissolution paths, one may write

$$\int_{\xi_0(t)}^{\xi_m} \phi_V(\xi) d\xi = - \int_t^{\infty} \dot{A}(t) dt \quad (3.12)$$

where  $\dot{A}(t)$  is the annihilation rate at time  $t$ . Operating on this equation by  $\frac{d}{dt}$  yields

$$\dot{A}(t) = - \frac{d \xi_0}{dt} \phi_V(\xi_0) \quad (3.13)$$

Since  $\xi_0$  and  $\frac{d \xi_0}{dt}$  are completely determined by the shrinkage rate, equation (3.13) demonstrates that the annihilation rate is not an independent variable. One can write the following expression for the volume fraction of the particles:

$$V_V(t) = \int_{\xi_0(t)}^{\xi_m} V(\xi, t) \phi_V(\xi) d\xi \quad (3.14)$$

where  $V(\xi, t)$  is the volume of particle at time  $t$ , whose

size was  $\xi$  in the initial distribution. Suppose that the particles are of spherical shape and the shrinkage rate can be modeled by the following functional form,

$$\left[\frac{dR}{dt}\right]_{\xi} = \frac{G_o}{n \cdot R^{n-1}} \quad (3.15)$$

where  $G_o$  is the constant determined by the kinetic parameters such as the diffusion coefficient and the exponent  $n$  is determined by the rate controlling mechanism. Integration of equation (3.15) yields

$$R = [\xi^n - \xi_o^n]^{1/n} \quad (3.16)$$

and

$$\xi_o^n = G_o \cdot t \quad (3.17)$$

For spherical particles, combining equations (3.14) and (3.16) yields

$$V_V(t) = \frac{4\pi}{3} \int_{\xi_o}^{\xi_m} [\xi^n - \xi_o^n]^{3/n} \phi_V(\xi) d\xi \quad (3.18)$$

If  $\phi_V(\xi)$  is known then the parameters  $n$  and  $G_o$  can be evaluated as follow.

(1) Assume a value of  $n$  and calculate  $V_V(t)$  for different values of  $\xi_o$  by using equation (3.18) Let  $V_V^1$ ,  $V_V^2$ , ..., etc. be the experimentally measured values of the volume fraction at times  $t_1$ ,  $t_2$ , ..., etc. One can calculate

$\xi_0^1, \xi_0^2, \dots$ , etc. at times  $t_1, t_2, \dots$ , etc. by comparing the experimental values of volume fraction with the calculated values. Now plot  $\xi_0^n$  vs.  $t$  for the values of  $\xi_0$  calculated in this manner. If the plot is linear, then the assumed value of  $n$  is correct and the slope of the straight line gives the parameter  $G_0$ . If the plot of  $\xi_0^n$  vs.  $t$  is nonlinear then assume a different value of  $n$  and repeat the calculations.

Similar procedures can be developed for more complicated shrinkage rate models. This algorithm is superior to the growth path analysis because it requires measurement of only one particle size distribution. However, the technique is limited to the dissolution process.

This work together with Woodhead's [57] and DeHoff's [58] analysis presents answers to the questions (A) and (B) posed in the beginning of this chapter for a system of discrete particles, provided that the growth paths do not cross and the particle size distributions can be measured.

### 3.2 Calculation of the Extended Global Properties from the Kinetic Models:

Let  $V(t, \tau)$ ,  $S(t, \tau)$  and  $M(t, \tau)$  be the volume, surface area and total curvature of a particle at time  $t$ , whose

nucleation time is  $\tau$ . Let  $\dot{N}(\tau)$  be the nucleation rate at time  $\tau$ . One can write the following expressions for extended volume fraction,  $V_{V_{ex}}$ , surface area,  $S_{V_{ex}}$ , and total curvature,  $M_{V_{ex}}$ , of a product phase at time  $t$  during a phase transformation:

$$V_{V_{ex}}(t) = \int_0^t V(t, \tau) \dot{N}(\tau) d\tau \quad (3.19)$$

$$S_{V_{ex}}(t) = \int_0^t S(t, \tau) \dot{N}(\tau) d\tau \quad (3.20)$$

$$M_{V_{ex}}(t) = \int_0^t M(t, \tau) \dot{N}(\tau) d\tau \quad (3.21)$$

It will be assumed that the kinetic state of a particle can be completely described by two size parameters,  $R$  and  $\ell$ . One may write the expressions for volume,  $V$ , surface area,  $S$ , and total curvature,  $M$ , of a particle in terms of  $R$  and  $\ell$ , if the quantitative particle shape is known.

However, almost all the simple shapes (sphere, cube, cylinder, ellipsoid of revolution, etc.) and growth geometries can be treated as the special cases of the following model for which the volume, surface area and total curvature are given by

$$V = (K_V R_o^2 \ell_o) \left[ \frac{R}{R_o} \right]^P \cdot \left[ \frac{\ell}{\ell_o} \right]^Q \quad (3.22)$$

$$S = K_{S1} R_o^2 \left[ \frac{R}{R_o} \right]^P + K_{S2} R_o \ell_o \cdot \left[ \frac{R}{R_o} \right]^a \cdot \left[ \frac{\ell}{\ell_o} \right]^Q \quad (3.23)$$

$$M = K_{M_1} R_o \left[ \frac{R}{R_o} \right]^a + K_{M_2} \ell_o \left[ \frac{\ell}{\ell_o} \right]^Q \quad (3.24)$$

where  $K_V$ ,  $K_{S_1}$ ,  $K_{S_2}$ ,  $K_{M_1}$  and  $K_{M_2}$  are the shape factors, while  $R_o$  and  $\ell_o$  are the constants which have dimensions of length. The exponents  $P$ ,  $Q$  and  $a$  are constants.

The following kinetics model will be assumed for the nucleation and growth.

(1) The following expression gives the total number of particles per unit volume,  $N_V(t)$ , at any given time,  $t$ :

$$N_V(t) = N_{V_o} + \frac{N}{(\alpha+1)} t^{\alpha+1} \quad (3.25)$$

where  $N_{V_o}$ ,  $N$  and  $\alpha$  are constants.

(2) The following kinetic model gives the time variation of  $R$  and  $\ell$ .

$$R = [G_R(t^m - \tau^m)]^{1/n} \quad (3.26)$$

$$\ell = [G_L(t^\omega - \tau^\omega)]^{1/\beta} \quad (3.27)$$

where  $G_R$  and  $G_L$  are the kinetic constants determined by the diffusion coefficient, equilibrium concentrations, etc. and the exponents  $m$ ,  $n$ ,  $\omega$  and  $\beta$  are constants. Different values of these constants give different physical models. For example, values of  $m = 1$  and  $n = 2$  describe semi-infinite diffusion controlled growth.

Combining equations (3.22), (3.26) and (3.27) gives

$$V(t, \tau) = \{K_V R_O^{2-P} \ell_O^{1-Q} G_R^{P/n} G_L^{Q/\beta}\} [t^m - \tau^m]^{P/n} [t^\omega - \tau^\omega]^{Q/\beta} \quad (3.28)$$

The extended volume fraction consists of two contributions; one from the particles,  $N_{V_0}$ , present at  $t = 0$  and the second from the particles which nucleate as the transformation proceeds [see equation (3.25)]. Let these two contributions be  $V_{ex}^{(1)}$  and  $V_{ex}^{(2)}$ . The first contribution,  $V_{ex}^{(1)}$ , is given by

$$V_{ex}^{(1)} = N_{V_0} \cdot V(t, 0)$$

where  $V(t, 0)$  is the volume of particles at time  $t$ , which were present at  $t = 0$ . Substituting  $\tau = 0$  in equation (3.28) gives  $V(t, 0)$ . Thus,

$$V_{ex}^{(1)} = N_{V_0} C_{PQ} t^{\left[\frac{Pm}{n} + \frac{Q\omega}{\beta}\right]} \quad (3.29)$$

where

$$C_{PQ} = K_V R_O^{2-P} \ell_O^{1-Q} \cdot G_R^{P/n} \cdot G_L^{Q/\beta} \quad (3.29a)$$

Differentiating equation (3.25) gives the nucleation rate. Thus, the nucleation rate,  $\dot{N}(\tau)$ , at time,  $\tau$ , is given by

$$\dot{N}(\tau) = N \cdot \tau^\alpha \quad (3.30)$$

Combining equations (3.19), (3.28) and (3.30) gives

$$V_{ex}^{(2)} = N C_{PQ} D_V t^{\left[\frac{Pm}{n} + \frac{Q\omega}{\beta} + \alpha + 1\right]} \quad (3.31)$$

where

$$D_V = \int_0^1 [1-u^m]^{P/n} [1-u^\omega]^{Q/\beta} \cdot u^\alpha du \quad (3.31a)$$

Note that  $D_V$  is just a number.

The total extended volume fraction,  $V_{V_{ex}}$ , is given by

$$V_{V_{ex}} = V_{V_{ex}}^{(1)} + V_{V_{ex}}^{(2)} \quad (3.32)$$

Combining equations (3.29), (3.31) and (3.32) gives

$$V_{V_{ex}} = C_{PQ} \{N_{V_0} + N D_V t^{\alpha+1}\} \cdot t^{\left(\frac{Pm}{n} + \frac{Q\omega}{\beta}\right)} \quad (3.33)$$

From equation (3.28), the volume of the particle of maximum size,  $V(t,0)$ , is given by

$$V(t,0) = C_{PQ} \cdot t^{\left(\frac{Pm}{n} + \frac{Q\omega}{\beta}\right)} \quad (3.34)$$

Substituting equation (3.34) into the equation (3.33) yields

$$V_{V_{ex}} = V(t,0) \{N_{V_0} + N D_V t^{\alpha+1}\} \quad (3.35)$$

Similar calculations for the extended surface area give the following result:



$$S_{V_{ex}} = A_P t^{mP/n} \cdot [N_{V_0} + N_{D_{S_1}} t^{\alpha+1}] \\ + B_{aQ} t^{(\frac{am}{n} + \frac{Q\omega}{\beta})} \cdot [N_{V_0} + N_{D_{S_2}} t^{\alpha+1}] \quad (3.36)$$

where

$$A_P = K_{S_1} R_O^{2-P} G_R^{P/n} \quad (3.36a)$$

$$B_{aQ} = K_{S_2} R_O^{1-a} \ell_O^{1-Q} G_R^{a/n} G_L^{Q/\beta} \quad (3.36b)$$

$$D_{S_1} = \int_0^1 (1-u^m)^{P/n} \cdot u^\alpha du \quad (3.36c)$$

$$D_{S_2} = \int_0^1 (1-u^m)^{a/n} (1-u^\omega)^{Q/\beta} \cdot u^\alpha du \quad (3.36d)$$

Note that  $A_P$ ,  $B_{aQ}$ ,  $D_{S_1}$  and  $D_{S_2}$  are constants. For most of the physically meaningful growth models, either

- (1) one of the two terms on the right-hand side of equation (3.36) is negligible, or
- (2) both the terms on the right-hand side of equation (3.36) have comparable values but  $D_{S_1} \approx D_{S_2}$ .

Thus one can approximate

$$S_{V_{ex}} \approx [A_P t^{mP/n} + B_{aQ} t^{(\frac{am}{n} + \frac{Q\omega}{\beta})}] \cdot [N_{V_0} + N_{D_S} t^{\alpha+1}] \quad (3.37)$$

Note that

$$S(t,0) = A_P t^{mP/n} + B_{aQ} t^{(\frac{am}{n} + \frac{Q\omega}{\beta})} \quad (3.38)$$

where  $S(t,0)$  is the surface area of a particle nucleated at  $t = 0$ . Combining equation (3.37) and (3.38) gives

$$S_{V_{ex}} = S(t,0) [N_{V_0} + N D_S t^{\alpha+1}] \quad (3.39)$$

where  $D_S$  is equal to  $D_{S_1}$  if the second term in equation (3.36) is negligible and it is equal to  $D_{S_2}$  if the first term can be neglected.  $D_S$  is approximately equal to either  $D_{S_1}$  or  $D_{S_2}$  if both the terms on the right-hand side of equation (3.36) have comparable values.

Calculations for the extended total curvature yield the following result:

$$\begin{aligned} M_{V_{ex}} &= E_a t^{\frac{a m}{n}} [N_{V_0} + N D_{M_1} t^{\alpha+1}] \\ &+ E_Q t^{\frac{Q \omega}{\beta}} [N_{V_0} + N D_{M_2} t^{\alpha+1}] \end{aligned} \quad (3.40)$$

where

$$E_a = K_{M_1} R_o^{1-a} G_R^{a/n} \quad (3.40a)$$

$$E_Q = K_{M_2} \ell_o^{1-Q} G_L^{Q/\beta} \quad (3.40b)$$

$$D_{M_1} = \int_0^1 [1-u^m]^{a/n} u^\alpha du \quad (3.40c)$$

$$D_{M_2} = \int_0^1 [1-u^\omega]^{Q/\beta} u^\alpha du \quad (3.40d)$$

Note that  $E_a$ ,  $E_Q$ ,  $D_{M_1}$  and  $D_{M_2}$  are constants. Again using the similar arguments as those used in the case of extended surface area, one can approximate

$$M_{V_{ex}} = M(t,0) [N_{V_0} + N D_M t^{\alpha+1}] \quad (3.41)$$

where  $M(t,0)$  is the total curvature of a particle nucleated at  $t = 0$ .

The various special cases of this model will be applied to real systems in the next three chapters. It is possible to develop more sophisticated models by assuming some other functional forms for the nucleation rate and growth rate. For example, if the total number of particles per unit volume,  $N_V(t)$ , has the following functional form,

$$N_V(t) = N_{V_0} + \frac{N}{(\alpha+1)} t^{\alpha+1} + \frac{C}{(\gamma+1)} t^{\gamma+1} \quad (3.42)$$

then the expression for the extended volume fraction is given by

$$V_{V_{ex}} = V(t,0) [N_{V_0} + N D_V t^{\alpha+1} + C D_C t^{\gamma+1}] \quad (3.43)$$

where

$$D_C = \int_0^1 (1-u^m)^{P/n} (1-u^\omega)^{Q/\beta} u^\gamma du \quad (3.43a)$$

and  $C$  and  $\gamma$  are constants. However, the present model is flexible enough to be valid for most of the cases.

### 3.3 Evaluation of the Nucleation Rate and Growth Rate from the Global Properties:

In this section, an attempt will be made to answer the question (B) posed in the beginning of this chapter. It may be said that in most of the physically meaningful cases a given microstructure at time  $t$  during a phase transformation contains a complete history of the following variables:

- (1) Starting microstructure
- (2) Nucleation rate
- (3) Growth rate
- (4) Spatial distribution of nuclei
- (5) Particle shape and Growth geometry

If this is so, then, in principle, it should be possible to invert this problem. Thus it should be possible to evaluate the nucleation and growth rate, etc. if all the global properties of the growing phase are measured at different times as the transformation proceeds. However, at present the stereological techniques have not been developed to measure all the global properties of the growing phase from the plane of polish. Thus some simplifying assumptions regarding these five variables may be needed to solve the problem.

A technique will now be developed to evaluate the

nucleation rate and growth rate from the measured values of the volume fraction, surface area and total curvature. In order to make the problem mathematically tractable the following assumptions will be made.

- (1) It is possible to convert the measured values of the global properties to their corresponding extended values.
- (2) The growth rate of a given particle is independent of the nucleation and growth of the other particles. This implies that the growth rate of a given particle depends only on the amount of time for which the particle is present in the system. If a particle nucleated at time,  $\tau$ , then its growth rate, at any time  $t$  during the transformation, depends only on  $(t-\tau)$ . It follows that, the volume, surface area and total curvature of the particle will be functions of  $(t-\tau)$  only. Thus,

$$V(t, \tau) = V(t-\tau) \quad (3.44)$$

$$S(t, \tau) = S(t-\tau) \quad (3.45)$$

$$M(t, \tau) = M(t-\tau) \quad (3.46)$$

Note that many theoretical models for growth assume this situation [3,6,8-11].

Combining equations (3.19) and (3.44) gives

$$V_{V_{ex}}(t) = \int_0^t V(t-\tau) \dot{N}(\tau) d\tau \quad (3.47)$$

Similarly,

$$S_{V_{ex}}(t) = \int_0^t S(t-\tau) \dot{N}(\tau) d\tau \quad (3.48)$$

and

$$M_{V_{ex}}(t) = \int_0^t M(t-\tau) \dot{N}(\tau) d\tau \quad (3.49)$$

The integrals on the right-hand side of these equations are called "convolution integrals." If the particle shape is known or at least can be modeled, then the functions  $V(t-\tau)$ ,  $S(t-\tau)$  and  $M(t-\tau)$  are not independent of each other. For a given particle shape, they are completely determined by the growth rate. In such a case, there are two unknown functions (nucleation rate and growth rate) in the above three integral equations. If one can solve these integral equations, then both the nucleation rate and growth rate can be obtained.

It is possible to solve the integral equations (3.47) to (3.49) by using Laplace transform techniques. A Laplace transform [80] of a function,  $\psi(t)$ , is defined as

$$L[\psi(t)] = \int_0^{\infty} e^{-St} \psi(t) dt \quad (3.50)$$

The transform,  $L[\psi(t)]$ , is a function of the parameter,  $S$ , only. An inverse,  $L^{-1}$ , of a Laplace transform [81] is defined as follows:

$$L^{-1}[L\{\psi(t)\}] = \psi(t) \quad (3.51)$$

The Laplace transform of a convolution integral has the following interesting properties [82]:

$$L\left\{\int_0^t V(t-\tau)\dot{N}(\tau)d\tau\right\} = L\{V(t)\} \cdot L\{\dot{N}(t)\} \quad (3.52)$$

Taking the Laplace transform of both sides of equation (3.47) gives

$$L\{V_{V_{ex}}(t)\} = L\left\{\int_0^t V(t-\tau)\dot{N}(\tau)d\tau\right\} \quad (3.53)$$

Combining equations (3.52) and (3.53) gives

$$L\{V_{V_{ex}}(t)\} = L\{V(t)\} \cdot L\{\dot{N}(t)\} \quad (3.54)$$

Rearranging the terms in equation (3.54) and taking the inverse,

$$\dot{N}(t) = L^{-1}\left\{\frac{L[V_{V_{ex}}(t)]}{L[V(t)]}\right\} \quad (3.55)$$

Similarly equations (3.48) and (3.49) give the following result:

$$\dot{N}(t) = L^{-1}\left\{\frac{L[S_{V_{ex}}(t)]}{L[S(t)]}\right\} \quad (3.56)$$

$$\dot{N}(t) = L^{-1}\left\{\frac{L[M_{V_{ex}}(t)]}{L[M(t)]}\right\} \quad (3.57)$$

Thus if the growth rate is known then the nucleation rate can be evaluated by using any of these three equations.

Combining the above equations for  $\dot{N}(t)$ , two at a time

and using the convolution theorem [82], leads to the following expressions

$$\int_0^t V(t-\tau) S_{V_{ex}}(\tau) d\tau = \int_0^t S(t-\tau) V_{V_{ex}}(\tau) d\tau \quad (3.58)$$

$$\int_0^t S(t-\tau) M_{V_{ex}}(\tau) d\tau = \int_0^t M(t-\tau) S_{V_{ex}}(\tau) d\tau \quad (3.59)$$

$$\int_0^t M(t-\tau) V_{V_{ex}}(\tau) d\tau = \int_0^t V(t-\tau) M_{V_{ex}}(\tau) d\tau \quad (3.60)$$

A careful examination of these equations leads to the following conclusions:

- (1) Only two of these three equations are independent.
- (2) The nucleation rate does not appear explicitly in these equations. The quantities  $V_{V_{ex}}$ ,  $S_{V_{ex}}$  and  $M_{V_{ex}}$  are obtained from the experimental data, while  $V(t-\tau)$ ,  $S(t-\tau)$  and  $M(t-\tau)$  are determined by the growth rate. Thus the quantitative evaluation of the local growth rate is possible without any knowledge of the nucleation behavior.

If the particle shape is known, then  $V(t-\tau)$ ,  $S(t-\tau)$  and  $M(t-\tau)$  are not independent unknown functions. For example, if the particles have a spherical shape then

$$S(t-\tau) = \frac{1}{4\pi} [M(t-\tau)]^2 \quad (3.61)$$

and

$$V(t-\tau) = \frac{1}{48\pi^2} [M(t-\tau)]^3 \quad (3.62)$$



In such a case, substituting equations (3.61) and (3.62) in equations (3.58) and (3.59) gives

$$\int_0^t [M(t-\tau)]^3 S_{V_{ex}}(\tau) d\tau = 12\pi \int_0^t [M(t-\tau)]^2 V_{V_{ex}}(\tau) d\tau \quad (3.63)$$

$$\int_0^t [M(t-\tau)]^2 M_{V_{ex}}(\tau) d\tau = 4\pi \int_0^t M(t-\tau) S_{V_{ex}}(\tau) d\tau \quad (3.64)$$

The third equation given by equation (3.60) is not an independent equation. There is only one unknown function,  $M(t-\tau)$ , in the above two equations. One can now solve equation (3.63) by numerical techniques [84] to get the values of  $M(t-\tau)$  for the different values of the argument. The solution can be checked by using equation (3.64). Alternatively, if several models are available for the growth process, then they can be checked by using these equations. Note that this technique does not require any knowledge or assumption regarding the nucleation behavior. Furthermore, the data processing involved in the equations (3.63) and (3.64) is the integration of the experimental data. Thus, the processing errors are expected to be small. This approach will be used in the fourth chapter to deduce the growth rate and the nucleation rate of austenite during an inverse eutectoid transformation.

### 3.4 Growth Geometry:

Various growth geometries will be described in this section. The importance of the growth geometry in the interpretation of experimental data will be demonstrated. In what follows, the growth geometries will be described for a cylindrical particle of radius  $R$  and length  $\ell$ . The description can be extended to some other particle shapes.

#### 3.4.1 Shape Preserving Growth

During shape preserving growth, the quantitative particle shape does not change with time. It follows that spherical growth is a special case of shape preserving growth. If the growth of a cylindrical particle occurs in such a way that  $(\ell/R)$  does not change with time, then it can be called a shape preserving growth. The model developed in section 3.2 will now be analyzed for the shape preserving growth of cylinders.

$$\frac{\ell}{R} = \text{Constant} = A_S \quad (3.65)$$

Comparing equations (3.26), (3.27) and (3.65) gives

$$m = w; \quad n = \beta \quad \text{and} \quad G_L = A_S G_R \quad (3.66)$$

Furthermore, since the particles have a cylindrical shape, the shape factors in equations (3.22) to (3.24) take the following values:

$$\left\{ \begin{array}{l} K_V = \pi ; \quad K_{S_1} = K_{S_2} = 2\pi \\ K_{M_1} = \pi^2; \quad K_{M_2} = \pi \end{array} \right\} \quad (3.67)$$

The exponents in equations (2.22) to (2.24) take the following values:

$$\{P = 2; \quad Q = a = 1\} \quad (3.68)$$

Substituting these values in the equation (3.33) gives

$$V_{V_{ex}} = C_{21} t^{3m/n} [N_{V_O} + N D_V t^{\alpha+1}] \quad (3.69)$$

where  $C_{21} = (A_S)^{1/n} G_R^{3/n} \cdot \pi$

and  $D_V = \frac{1}{\int_0^1 [1-u^m]^{3/n} \cdot u^\alpha du}$

Similarly for this particular case, equations (3.36) and (3.40) give the following results:

$$S_{V_{ex}} = \{2\pi[1+A_S] \cdot G_R^{2/n}\} t^{2m/n} [N_{V_O} + N D_S t^{\alpha+1}] \quad (3.70)$$

Note that  $D_S = D_{S_1} = D_{S_2}$  for the shape preserving growth.

$$M_{V_{ex}} = \{[\pi^2 + A_S] G_R^{1/n}\} t^{m/n} [N_{V_O} + N D_M t^{\alpha+1}] \quad (3.71)$$

One can now calculate  $(\bar{v}_S)_{ex}$  and  $(\bar{v}_H)_{ex}$  by using equations (3.69) to (3.71). The behavior of  $(\bar{v}_S)_{ex}$  and  $(\bar{v}_H)_{ex}$  is determined by all the parameters of the model ( $G_R$ ,  $m$ ,  $n$ , etc.). Thus in this case the interface velocities may be used to get information about the growth rate; it will now be shown that this is not always true.

### 3.4.2 Two Dimensional Growth

If a cylindrical particle grows in such a manner that its radius  $R$  increases with time, while its length remains constant, then such a growth behavior is called "two dimensional growth." The concept of two dimensional growth can be extended to some other particle shapes. Let us denote the constant length of the cylindrical particle by  $\ell_0$ . One can write the following expressions:

$$V(t, \tau) = [\pi \ell_0] [R(t, \tau)]^2 \quad (3.72)$$

$$S(t, \tau) = 2\pi [R(t, \tau)]^2 + 2\pi \ell_0 \cdot R(t, \tau) \quad (3.73)$$

Since the radius of the particle increases with time while its length remains constant, soon after nucleation the first term on the right-hand side of the equation (3.73) will be much larger than the second term. Thus,

$$S(t, \tau) = 2\pi [R(t, \tau)]^2 \quad (3.74)$$

Substituting equations (3.72) and (3.74) into the equations (3.19) and (3.20) gives

$$V_{\text{ex}}(t) = \pi \ell_0 \int_0^t [R(t, \tau)]^2 \dot{N}(\tau) d\tau \quad (3.75)$$

and

$$S_{\text{ex}}(t) = 2\pi \int_0^t [R(t, \tau)]^2 \dot{N}(\tau) d\tau \quad (3.76)$$

Substituting equation (3.76) into (3.75) gives

$$V_{V_{ex}}(t) = \left(\frac{\ell_o}{2}\right) S_{V_{ex}}(t) \quad (3.77)$$

Since  $\ell_o$  does not change with time, equation (3.77) predicts a linear relationship between the extended volume fraction and surface area. Equation (3.77) is a direct consequence of the assumed two dimensional growth geometry. No assumptions regarding the nucleation rate or growth rate were made in deriving equation (3.77).\*

The extended surface area averaged interface velocity,  $(\bar{v}_S)_{ex}$ , is given by

$$(\bar{v}_S)_{ex} = \frac{1}{S_{V_{ex}}} \frac{d V_{V_{ex}}}{dt} \quad (3.77a)$$

For two dimensional growth, substituting equation (3.77) into equation (3.77a) yields

$$(\bar{v}_S)_{ex} = \frac{\ell_o}{2} \cdot \frac{d \ln V_{V_{ex}}}{dt} \quad (3.78)$$

The behavior of  $(\bar{v}_S)_{ex}$  will now be analyzed for the model developed in section 3.2. For two dimensional growth of cylindrical particles, the parameters P, Q and a in the equations (3.22) to (3.24) take the following values:

$$\{P = 2; \quad Q = 0; \quad a = 1\} \quad (3.79)$$

---

\*Note that for a two dimensional growth, equation (2.58) becomes redundant.

For these values of the parameters, equation (3.33) takes the following form:

$$V_{V_{ex}}(t) = [\pi \ell_o G_R^{2/n}] [N_{V_o} + N D_V t^{\alpha+1}] \cdot t^{2m/n} \quad (3.80)$$

Substituting equation (3.80) into (3.78) gives

$$(\bar{v}_S)_{ex} = \left(\frac{\ell_o m}{2n}\right) \cdot \left[\frac{1}{t} + \frac{n N D_V (\alpha+1) t^{\alpha}}{m(N_{V_o} + N D_V t^{\alpha+1})}\right] \quad (3.81)$$

If  $N_{V_o} = 0$ , then

$$(\bar{v}_S)_{ex} = \left(\frac{\ell_o m}{2n}\right) \left(1 + \frac{n(\alpha+1)}{m}\right) \cdot \frac{1}{t} \quad (3.82)$$

If  $N = 0$  (i.e. site saturation), then

$$(\bar{v}_S)_{ex} = \left[\frac{\ell_o m}{2n}\right] \cdot \frac{1}{t} \quad (3.83)$$

The coefficients of  $1/t$  in equations (3.82) and (3.83) do not depend on temperature. These equations predict that  $(\bar{v}_S)_{ex}$  should be independent of temperature.

Furthermore, the hyperbolic time dependence of  $(\bar{v}_S)_{ex}$  is not affected by the parameters of the growth mode (i.e.  $G_R$ ,  $m$  and  $n$ ).

This analysis of two dimensional growth will be used in the next chapter for the interpretation of some experimental data.

### 3.4.3 One Dimensional Growth

If a cylindrical particle grows in such a manner that its length,  $\ell$ , increases with time while its radius remains constant, then such a behavior is called "one dimensional growth." This concept can be extended to some other particle shapes. Let us denote the constant radius of the cylindrical particle by  $R_0$ . One can write the following expressions:

$$V(t, \tau) = [\pi R_0^2] \ell(t, \tau) \quad (3.84)$$

$$S(t, \tau) \approx [2\pi R_0] \ell(t, \tau) \quad (3.85)$$

$$M(t, \tau) \approx \pi \cdot \ell(t, \tau) \quad (3.86)$$

Combining equations (3.84) and (3.19) gives

$$V_{V_{ex}}(t) = \pi R_0^2 \int_0^t \ell(t, \tau) \dot{N}(\tau) d\tau \quad (3.87)$$

Similarly,

$$S_{V_{ex}}(t) = 2\pi R_0 \int_0^t \ell(t, \tau) \dot{N}(\tau) d\tau \quad (3.88)$$

and

$$M_{V_{ex}}(t) = \pi \int_0^t \ell(t, \tau) \dot{N}(\tau) d\tau \quad (3.89)$$

Combining equations (3.87) and (3.89) gives

$$V_{V_{ex}}(t) = \left(\frac{R_0}{2}\right) S_{V_{ex}}(t) = R_0^2 M_{V_{ex}}(t) \quad (3.90)$$

Since  $R_o$  does not change with time, equation (3.90) predicts a linear relationship between the extended volume fraction, surface area and total curvature. Again, the derivation of equations (3.90) do not require any assumptions regarding the nucleation rate or growth rate. Combining equations (3.78) and (3.90) gives

$$(\bar{v}_S)_{ex} = \frac{R_o}{2} \frac{d \ln V_{V_{ex}}}{dt} \quad (3.91)$$

The extended total curvature averaged interface velocity,  $(\bar{v}_H)_{ex}$ , is given by

$$(\bar{v}_H)_{ex} = \frac{1}{2 M_{V_{ex}}} \cdot \frac{d S_{V_{ex}}}{dt} \quad (3.92)$$

Substituting equation (3.90) into (3.92) gives

$$(\bar{v}_H)_{ex} = R_o \cdot \frac{d \ln S_{V_{ex}}}{dt} = R_o \frac{d \ln V_{V_{ex}}}{dt} \quad (3.93)$$

or

$$(\bar{v}_H)_{ex} = 2(\bar{v}_S)_{ex} \quad (3.94)$$

The behavior of  $(\bar{v}_S)_{ex}$  and  $(\bar{v}_H)_{ex}$  will now be analyzed for the model developed in section 3.2. For one dimensional growth,

$$\{P = 0; \quad Q = 1; \quad a = 0\} \quad (3.95)$$

Substituting these values of P, Q and a together with shape factors for the cylindrical [equation (3.67)] in



equation (3.33) gives

$$V_{V_{ex}}(t) = [\pi R_O^2 G_L^{1/\beta}] \cdot t^{\omega/\beta} \cdot [N_{V_O} + N D_V t^{\alpha+1}] \quad (3.96)$$

Substituting equation (3.96) in (3.91) gives

$$(\bar{v}_S)_{ex} = \left(\frac{R_O \omega}{2\beta}\right) \cdot \frac{1}{t} + \frac{R_O N D_V (\alpha+1) t^\alpha}{2(N_{V_O} + N D_V t^{\alpha+1})} \quad (3.97)$$

Combining equations (3.94) and (3.97) yields

$$\frac{(\bar{v}_H)_{ex}}{2} = (\bar{v}_S)_{ex} = \left(\frac{R_O \omega}{2\beta}\right) \cdot \frac{1}{t} + \frac{R_O N D_V (\alpha+1) t^\alpha}{2(N_{V_O} + N D_V t^{\alpha+1})} \quad (3.98)$$

If  $N_{V_O} = 0$ ,

$$\frac{(\bar{v}_H)_{ex}}{2} = (\bar{v}_S)_{ex} = \left[\frac{R_O}{2}(\frac{\omega}{\beta} + \alpha + 1)\right] \cdot \frac{1}{t} \quad (3.99)$$

If  $N = 0$  (i.e. site saturation),

$$\frac{(\bar{v}_H)_{ex}}{2} = (\bar{v}_S)_{ex} = \left[\frac{R_O \omega}{2\beta}\right] \cdot \frac{1}{t} \quad (3.100)$$

The quantities in the square brackets in equations (3.99) and (3.100) do not depend on the temperature. These equations predict that  $(\bar{v}_S)_{ex}$  and  $(\bar{v}_H)_{ex}$  should be independent of temperature. Furthermore, the hyperbolic time dependence of  $(\bar{v}_S)_{ex}$  and  $(\bar{v}_H)_{ex}$  is not affected by the parameters of the growth model (i.e.  $G_L$ ,  $\omega$  and  $\beta$ ).

### 3.5 The Impingement Problem:

Imagine a structure calculated from some model based

upon an assumed nucleation rate and growth rate (for example, the model in section 3.2). If the standard methods for calculating the global properties of the structure are used, such calculations will over estimate the corresponding properties in the real structure. The magnitude of this over estimation increases with the increase in the volume fraction of the growing phase. The over estimates result because the geometrical impingement of the growing particles is not taken into account. As mentioned in the second chapter, the modeled structure in which the particles may grow through one another is called the "extended structure." If the particles are distributed randomly in the structure, then equations (2.15) and (2.16) give relations between some real and extended global properties. A simple derivation of these equations will be first given.

It will be assumed that the particle centers are distributed randomly in the matrix. For such a case, Chandrasekhar [76] and Hertz [77] have given the following expression:

$$\phi(x) = 4\pi x^2 N_V \text{Exp}\left\{-\frac{4\pi}{3} x^3 N_V\right\} \quad (3.101)$$

where  $\phi(x)dx$  is the probability that the first nearest neighbor of a given particle center is in the spherical

shell of radii  $x$  and  $(x + dx)$  and  $N_V$  is the total number of particles per unit volume.

The derivation will be first given for a simple case where all the particles are spheres of radius  $R(t)$ . Let  $dV_V$  and  $dV_{V_{ex}}$  be the changes in the real and extended volume fractions during a small increment in time,  $dt$ . Focus upon a small part,  $\delta(dV_{V_{ex}})$ , of an incremental layer,  $(4\pi R^2 dR)$ , on one particle. Now,  $\delta(dV_{V_{ex}})$  will contribute to the real volume only if there is no particle center in a sphere of radius  $R(t)$  around it. The probability of this event is  $[1 - \int_0^{R(t)} \phi(x) dx]$ . This probability is the same for all such volume elements in the structure at a given time  $t$  and it gives fraction of such elements which contribute to the real structure. Hence,

$$\Sigma \delta(dV_V) = [1 - \int_0^{R(t)} \phi(x) dx] \Sigma \delta(dV_{V_{ex}})$$

or

$$dV_V = [1 - \int_0^{R(t)} \phi(x) dx] \cdot dV_{V_{ex}} \quad (3.102)$$

Substituting equation (3.101) into (3.102) and invoking the fact that  $V_{V_{ex}}$  is equal to  $\frac{4\pi}{3}[R(t)]^3 N_V$  gives the following result:

$$dV_V = e^{-V_{V_{ex}}} \cdot dV_{V_{ex}} \quad (3.103)$$

Integration of this equation gives

$$V_V = 1 - \text{Exp}(-V_{V_{\text{ex}}})$$

This equation is identical to equation (2.15) proposed by Kolmogorov [69] and Avrami et al. [70].

Consider a small elemental area,  $\delta(S_{\text{ex}})$ , on the extended surface of any particle. This element will contribute to the real surface area only if there is no particle center in a sphere of radius  $R(t)$  around it. The probability of this event is again  $[1 - \int_0^{R(t)} \phi(x)dx]$ . This probability is equal to the fraction of such elements which contribute to the real surface area. Thus

$$\Sigma \delta(S) = [1 - \int_0^{R(t)} \phi(x)dx] \Sigma \delta(S)_{\text{ex}}$$

or

$$S_V = [1 - \int_0^{R(t)} \phi(x)dx] S_{V_{\text{ex}}}$$

But,

$$[1 - \int_0^{R(t)} \phi(x)dx] = e^{-V_{V_{\text{ex}}}} = (1-V_V)$$

Hence,

$$S_V = (1-V_V) S_{V_{\text{ex}}}$$

This equation is identical to equation (2.16).

Now let us consider the case where all the particles are not of same size in the extended structure. Let  $E(R,t)$  be the extended particle size distribution function of the spherical particles. Let us divide this distribution function into  $N_e$  equally spaced histograms and let  $\Delta R$  be the size class interval. Note that

$$V_{V_{ex}} = \lim_{\substack{N_e \rightarrow \infty \\ \Delta R \rightarrow 0}} \left\{ \sum_{i=1}^{N_e} \frac{4\pi}{3} R_i^3 E(R_i, t) \Delta R \right\} \quad (3.104)$$

Again, consider an element,  $\delta(dV_{V_{ex}})$ , on any particle. The probability,  $P_r$ , that this volume element will contribute to the real structure is a product of  $N_e$  probabilities. The probability,  $P_{r_i}$ , that there is no particle of radius  $R_i$  inside a sphere of radius  $R_i$  around this volume element is given by

$$P_{r_i} = [1 - \int_0^{R_i} \phi_i(x) dx]$$

where

$$\phi_i(x) = 4\pi x^2 E(R_i, t) \Delta R \cdot \text{Exp}\left\{-\frac{4\pi x^3}{3} E(R_i, t) \Delta R\right\}$$

Thus

$$P_{r_i} = e^{-\frac{4\pi R_i^3}{3} E(R_i, t) \Delta R}$$

The probability,  $P_r$ , that the incremental volume element,  $\delta(dV_{V_{ex}})$ , will contribute to the real structure is given by

$$P_r = \prod_{i=1}^{N_e} P_{r_i} = \prod_{i=1}^{N_e} \text{Exp}\left\{-\frac{4\pi R_i^3}{3} E(R_i, t) \Delta R\right\}$$

or

$$P_r = \text{Exp}\left\{-\sum_{i=1}^{N_e} \frac{4\pi R_i^3}{3} E(R_i, t) \Delta R\right\}$$

As  $N_e \rightarrow \infty$  and  $\Delta R \rightarrow 0$ , the summation is exactly equal to  $V_{V_{ex}}$  [see equation (3.104)]. Thus,

$$P_r = \text{Exp}(-V_{V_{ex}}) \quad (3.105)$$

Again, the probability,  $P_r$ , is equal to the fraction of the incremental elements,  $\delta(dV_{V_{ex}})$ , which contribute to the real structure. Hence,

$$\sum \delta(dV_V) = \{\text{Exp}(-V_{V_{ex}})\} \sum \delta(dV_{V_{ex}})$$

or

$$dV_V = e^{-V_{V_{ex}}} dV_{V_{ex}}$$

The integration of this equation gives equation (2.15).

To derive equation (2.16), consider a small surface element,  $\delta(S_{ex})$ , on the extended surface of any particle.

The probability that this element will contribute to the

real structure is exactly equal to  $P_r$ . Thus,

$$\Sigma \delta(S) = \{\text{Exp}(-V_{V_{\text{ex}}})\} \Sigma \delta(S_{\text{ex}})$$

or

$$S_V = \{\text{Exp}(-V_{V_{\text{ex}}})\} S_{V_{\text{ex}}}$$

or

$$S_V = (1 - V_V) S_{V_{\text{ex}}}$$

The approach can be generalized for convex particles of other shapes if their orientation is also random.

### 3.5.1 Non-random Impingement

Let us assume that all the particles are spheres of radius  $R(t)$ , but the distribution of their particle centers is non-random. Consider an incremental element,  $\delta(dV_{V_{\text{ex}}})$ , on the surface of a particle. Let the spatial coordinates of this element be  $(u, v, w)$ . The probability that there is no particle center in a sphere of radius  $x$  and there is at least one particle in a spherical shell of radii  $x$  and  $(x + dx)$  is given by

$$\phi(x)dx = [1 - \int_0^x \phi(x)dx] P_{uvw}(x)dx \quad (3.106)$$

where the first term on the right-hand side of this equation is the probability that there is no particle center in a sphere of radius  $x$ . The second term,  $P_{uvw}(x)dx$ , is

the probability that there is at least one particle center in the spherical shell of radii  $x$  and  $(x + dx)$ . The subscript "uvw" signifies that this probability will depend on the spatial coordinates  $(u, v, w)$  of the incremental element,  $\delta(dV_{V_{ex}})$ . Let  $V_0$  be the total volume of the sample. An average value,  $\bar{P}(x)$ , of  $P_{uvw}(x)$  can now be defined as follows:

$$\bar{P}(x) = \frac{1}{V_0} \iiint P_{uvw}(x) du dv dw \quad (3.107)$$

Since we are interested only in the average properties, a "spatial average" value of  $\phi(x)$  can be evaluated by using the following equation:

$$\phi(x) = [1 - \int_0^x \phi(x) dx] \bar{P}(x) \quad (3.108)$$

The solution to this integral equation gives the following result:

$$\phi(x) = \bar{P}(x) \text{Exp}\left\{-\int_0^x \bar{P}(x) dx\right\} \quad (3.109)$$

The probability that there is no particle in a sphere of radius  $R(t)$  is given by

$$pr = \text{Exp}\left\{-\int_0^{R(t)} \bar{P}(x) dx\right\} \quad (3.110)$$

Thus, if all the particles are spheres of radius  $R(t)$ , then



$$dV_V = 4\pi[R(t)]^2 N_V [\text{Exp}\{-\int_0^{R(t)} \bar{P}(x) dx\}] dR \quad (3.111)$$

or

$$V_V = \int_0^{R(t)} 4\pi[R(t)]^2 N_V \text{Exp}\{-\int_0^{R(t)} \bar{P}(x) dx\} dR(t) \quad (3.112)$$

The development can be generalized if there is a distribution of spheres in the extended space. Thus, if quantitative information about  $\bar{P}(x)$  is available, then the non-random impingement problem can be solved. However, physically meaningful models for  $\bar{P}(x)$  must be developed for the further analysis of this approach.

### 3.5.2 A Phenomenological Approach to Non-Random Impingement

A simple approach will now be presented which is extremely useful for two dimensional and one dimensional growth. It may be conjectured that the physical factors responsible for these growth geometries may also give rise to non-random distribution of particle centers in space. For two dimensional or one dimensional growth [see equations (3.77) and (3.90)],

$$V_{V_{\text{ex}}} = K \cdot S_{V_{\text{ex}}} \quad (3.113)$$

where  $K$  is a geometrical constant.

It will be assumed that

$$dV_V = \psi(V_V) dV_{V_{ex}} \quad (3.114)$$

where  $\psi(V_V)$  is the impingement function to be evaluated.

Now,

$$V_{V_{ex}} = \int_0^{V_V} \frac{dV_V}{\psi(V_V)} \quad (3.115)$$

Using the same arguments as used earlier,

$$S_{V_{ex}} = \frac{S_V}{\psi(V_V)} \quad (3.116)$$

Combining equations (3.113), (3.115) and (3.116) yields

$$\int_0^{V_V} \frac{dV_V}{\psi(V_V)} = K \frac{S_V}{\psi(V_V)} \quad (3.117)$$

The solution to this integral equation is as follows:

$$\psi(V_V) = K S_V e^{-\int \frac{dV_V}{K S_V}} + B \quad (3.118)$$

where B is a constant and can be evaluated as follows:

$$B = -\lim_{V_V \rightarrow 1} \left\{ K S_V e^{-\int \frac{dV_V}{K S_V}} \right\}$$

### 3.6 Conclusions:

(1) A generalized continuity equation has been derived and an approach to the solution of the problem of crossing growth paths is suggested.

(2) An expression is derived for the particle size distribution function, during a dissolution process, in terms of the initial particle size distribution function and shrinkage rate.

(3) An algorithm is developed for the evaluation of shrinkage rate during a dissolution process. The input information required is the initial particle size distribution function and the values of the global properties of the dissolving phase at various times during the dissolution process.

(4) A systematic approach has been developed for the evaluation of the global properties of a growing phase from a given description of the local variables. A flexible but simple model is developed for the calculation of global properties.

(5) A fairly general technique has been developed to deduce the nucleation rate and growth rate from the time variation of the global properties.

(6) Effects of various growth geometries on the kinematics of phase transformation are explored in detail.

(7) A simple derivation of the impingement equations is given for the case of random impingement.

(8) A solution to the general non-random impingement problem is suggested. A phenomenological approach is developed for the evaluation of the non-random impingement function for two dimensional and one dimensional growth.

## CHAPTER IV RECRYSTALLIZATION

### 4.1 Introduction:

The purpose of this chapter and the next two chapters is to demonstrate the applicability of the analysis developed in the previous chapters. In this chapter, the data of some other research workers [79,92] on the kinetics of the recrystallization process will be reanalyzed and reinterpreted by using the present approach. It will be shown that some apparent "paradoxes" which exist in the literature can be resolved by using some simple explanations based only on the geometry of the microstructural evolution.

General reviews of the detailed treatments on the topic of recrystallization can be found in different works [95-97]. Nucleation in recrystallization is defined as the formation of a strain-free region whose boundary can transform the strained matrix into a strain-free material as it moves. Two mechanisms are identified for the process; one involving the existing grain boundaries (strain induced boundary migration), and the second involving the regions of sharp lattice curvature (sub-

grain growth). Theoretical models for the kinetics of grain boundary migration have been developed [98-101].

In experimental studies, the kinetics of recrystallization may be monitored by measuring the global properties of the microstructure during the process. Speich and Fisher [79] have studied the recrystallization of 3% silicon steel by using quantitative microscopic techniques. The experimental data of Speich and Fisher [79] will now be reanalyzed.

#### 4.2 The Experimental Work of Speich and Fisher [79]:

The experiments were performed on a 3.27% silicon steel with 0.019% carbon. The grain size of the starting material was about fifty microns. The material was cold rolled 60% to produce a strained matrix. The recrystallization of this strained matrix was studied at various temperatures between 500°C to 1000°C. A laser heating technique was used for short annealing times (0.002 sec to 0.1 sec used at high temperatures). The volume fraction,  $V_V$ , and the surface area,  $S_V$ , of the recrystallized regions was measured by using the standard stereological techniques.

#### 4.2.1 Experimental Observations

(1) The recrystallized grain size was found to be independent of the annealing temperature. Note that the experiments were performed at various temperatures ranging from 500°C to 1000°C. The recrystallized grain size was about 11 microns.

(2) The relationship between the volume fraction,  $V_V$ , and surface area,  $S_V$ , could be described for all the times and temperatures studied by a single empirical equation:

$$S_V = K_0 V_V(1 - V_V) \quad (4.1)$$

where  $K_0 = 3600 \text{ cm}^2/\text{cm}^3$ .  $K_0$  was found to be independent of temperature.

(3) The time dependence of the volume fraction, at all the annealing temperatures, could be described by the empirical equation

$$\text{Log}\left\{\frac{V_V}{(1-V_V)}\right\} = 3.08 \text{ Log}\left\{\frac{t}{t_0}\right\} - 1.679 \quad (4.2)$$

where  $t_0$  is the time required for 2% recrystallization;  $t_0$  depends on the annealing temperature.

(4) The surface area averaged interface velocity,  $\bar{v}_S$ , could be described by the following equation:

$$\bar{v}_S = \frac{8.5 \times 10^{-4}}{t} \text{ cm/sec} \quad (4.3)$$

This equation was obeyed by the experimental data at all the annealing temperatures. Thus, the surface area averaged interface velocity,  $\bar{v}_s$ , was found to be independent of temperature.

(5) The activation energy for the process was found to be 70.1 K cal/mole.

#### 4.2.2 Speich and Fisher's Interpretation of Their Data

Speich and Fisher [79] developed a model to explain the experimental behavior of the surface area averaged interface velocity, described by equation (4.3). Their assumptions are as follows:

(1) Recovery occurs concurrently with the recrystallization process, not only in the initial stages, but til the process is complete.

(2) The decrease in the stored energy,  $E_s$ , due to the recovery process is given by

$$\frac{dE_s}{dt} = -K_r E_s^2 \quad (4.4)$$

where  $K_r = A_r \text{Exp}\{-Q_r/RT\}$  and  $Q_r$  is the activation energy for the recovery process, while  $A_r$  is a constant.

(3) The activation energy for the recovery process,  $Q_r$ , is equal to the activation energy for the growth of the recrystallized regions.

Using these assumptions, together with an expression



for the local interface velocity of the recrystallized regions developed by Gordon [102], Speich and Fisher derived an equation similar to the empirical equation (4.3). Note that it is not possible to explain the other experimental observations by using this model. Furthermore, the assumptions made by Speich and Fisher, in their model, are physically unrealistic.

All the experimental observations of Speich and Fisher will now be explained by using the present approach. This interpretation does not require any of the assumptions made by Speich and Fisher.

#### 4.3 Reanalysis of Speich and Fisher's Data:

Assume that the recrystallized grains nucleate at the grain edges of the cold worked matrix (Vandermeer and Gordon's work [87] on the recrystallization in aluminum supports this assumption) and they have a cylindrical shape. Each cylindrical grain reaches a certain length,  $l_0$ , soon after nucleation. Once the grain has achieved this length,  $l_0$ , its length does not increase. Thus, soon after nucleation a grain grows in a two dimensional fashion in the sense that its radius increases with time, while the length remains constant. The radial growth of recrystallized grains takes place at a constant growth

rate,  $G_R$ . It will be further assumed that the nucleation takes place at a constant rate,  $N$ .

For this special case, the parameters in the model developed in section 3.2 take the following values:

$$\begin{aligned} P &= 2; \quad Q = 0; \quad a = 1 \\ K_V &= \pi; \quad K_{S_1} = K_{S_2} = 2\pi \\ \{ K_{M_1} &= \pi^2; \quad K_{M_2} = \pi \} \end{aligned} \quad (4.5)$$

and  $m = n = 1; \quad N_{V_0} = 0; \quad \alpha = 0$

For these values of the parameters, equations (3.33), (3.36) and (3.82) give the following results:

$$V_{V_{ex}} = \left[ \frac{\pi \ell_0 N G_R^3}{3} \right] t^3 \quad (4.6)$$

$$S_{V_{ex}} = \left[ \frac{2 N G_R^3}{3} \right] t^3 \quad (4.7)$$

and  $(\bar{V}_S)_{ex} = \left( \frac{3 \ell_0}{2} \right) \cdot \frac{1}{t} \quad (4.8)$

In order to compare the experimental behavior [equations (4.1) to (4.3)] with these predictions of the model, it is necessary to evaluate the impingement function.

This can be done as follows.

For the two dimensional growth, equation (3.77) gives

$$V_{V_{ex}} = \frac{\ell_0}{2} S_{V_{ex}} \quad (3.77)$$

and the impingement function,  $\psi(V_V)$ , is given by equation (3.118):

$$\psi(V_V) = \frac{\ell_0}{2} S_V \text{Exp}\left\{-\frac{2}{\ell_0} \int \frac{dV_V}{S_V}\right\} + B \quad (3.118)$$

Substituting equation (4.1) into the equation (3.118) gives

$$\psi(V_V) = \left(\frac{3600\ell_0}{2}\right) V_V^{\left(1 - \frac{3600\ell_0}{2}\right)} [1 - V_V]^{\left(1 + \frac{3600\ell_0}{2}\right)} + B$$

since  $\lim_{V_V \rightarrow 1} (\psi(V_V)) \rightarrow 0$  thus  $B = 0$

Furthermore, the function  $\psi(V_V)$  must be monotonic, and  $\psi(V_V) \rightarrow 1$  as  $V_V \rightarrow 0$ . Hence,

$$1 - \frac{3600\ell_0}{2} = 0$$

$$\text{or} \quad \ell_0 = 5.55 \times 10^{-4} \text{ cm} \quad (4.9)$$

$$\text{and} \quad \psi(V_V) = (1 - V_V)^2 \quad (4.10)$$

Substituting equation (4.10) into equations (3.115) and (3.116) gives

$$\frac{V_V}{1 - V_V} = V_{V_{\text{ex}}} \quad (4.11)$$

and

$$\frac{S_V}{(1 - V_V)^2} = S_{V_{\text{ex}}} \quad (4.12)$$

Furthermore, equations (4.11) and (4.12) give

$$\bar{v}_S = (\bar{v}_S)_{\text{ex}} \quad (4.13)$$

Combining equations (4.6) and (4.11) yields

$$\frac{v_V}{1-v_V} = \left[ \frac{\pi l_0 N_R^3}{3} \right] t^3 \quad (4.14)$$

Let  $t_0$  be the time required for 2% recrystallization.

Then,

$$0.02 = \left[ \frac{\pi l_0 N_R^3}{3} \right] t_0^3 \quad (4.15)$$

Combining equations (4.14) and (4.15) gives

$$\frac{v_V}{1-v_V} = 0.02 \left( \frac{t}{t_0} \right)^3$$

or

$$\text{Log} \left[ \frac{v_V}{1-v_V} \right] = 3 \text{Log} \left[ \frac{t}{t_0} \right] - 1.699 \quad (4.16)$$

Equation (4.16) which is derived from the present model is in excellent agreement with the empirical equation (4.2) which describes the experimental behavior.

Combining equations (4.8), (4.9) and (4.13) yields

$$\bar{v}_S = \frac{8.33 \times 10^{-4}}{t} \text{ cm/sec} \quad (4.17)$$

Again, equation (4.17), derived from the model, is in excellent agreement with the empirical equation (4.3) which describes the experimental behavior.

Combining equations (2.77), (2.11) and (4.12) gives

$$S_V = 3600V_V(1-V_V) \quad (4.1)$$

It is important to note that  $\ell_0$  is not expected to change with the annealing temperature. The mean grain intercept or the grain size at the end of the recrystallization process can now be predicted. Due to two dimensional nature of the growth, the mean grain intercept of the recrystallized grains should be equal to  $(2\ell_0)$ . This result is independent of the number of recrystallized grains or their volume fraction. Thus one can say that the grain size, at the end of the process, should be equal to  $(2\ell_0)$ . Hence,

$$\text{Recrystallized grain size} = 2\ell_0 = 11.1 \text{ microns} \quad (4.19)$$

The recrystallized grain size, measured by Speich and Fisher, was 11 microns. Thus the prediction is again in excellent agreement with the experimental value. Since  $\ell_0$  is not expected to change with the annealing temperature, the model predicts that the recrystallized grain size should be independent of the annealing temperature, which is precisely what is observed.

The present model explains every qualitative and quantitative experimental observation. The assumptions regarding the constant nucleation rate and growth rate are

the simplest assumptions one can make and are supported by the theoretical models for the nucleation and growth of the recrystallized regions. The peculiar experimental behavior of  $\bar{v}_S$  of the recrystallized grains is mainly due to the two dimensional nature of the growth. It seems that the complicated model developed by Speich and Fisher based on physically unrealistic assumptions is rather unnecessary.

English and Backofen [92] have studied the recrystallization behavior in the same system and their data will now be reanalyzed.

#### 4.4 The Experimental Work of English and Backofen [92]:

Recrystallization was studied in Fe-3.19% Si alloy. The composition of the alloy was very close to the alloy used by Speich and Fisher [79]. However, English and Backofen used uniaxial hot compression as a mode of deformation to introduce the prestrain rather than the cold rolling used by Speich and Fisher [79]. The volume fraction,  $V_V$ , and the surface area,  $S_V$ , of the recrystallized regions was measured at different annealing times, prestrains and temperatures.

English and Backofen [92] presented a qualitative and quantitative metallographic evidence for grain edge

nucleation. Their experimental observations are as follows.

(1) The recrystallized grain size was found to be independent of the annealing temperature.

(2) The surface area averaged interface velocity,  $\bar{v}_S$ , could be described by the empirical equation

$$\bar{v}_S = \frac{1}{\frac{1}{G} + \frac{t}{c}} \quad (4.18)$$

where  $c = 4.0 \times 10^{-3}$  cm. The constant,  $c$ , was found to be independent of the annealing temperature but the constant,  $G$ , was temperature dependent.

Their explanation for the experimental behavior of  $\bar{v}_S$  is very similar to that presented by Speich and Fisher [79].

#### 4.5 Reanalysis of English and Backofen's Data:

It will be assumed that the recrystallized grains nucleate at the grain edges of the strained matrix and then quickly spread along the grain boundaries of the matrix. The further growth of the recrystallized regions occurs by the "thickening" of the recrystallized grains. This amounts to an assumption of one dimensional growth. It will be further assumed that all the nuclei appear at zero time. Thus there is a site saturation. Let  $N_{V0}$  be

the number of recrystallized grains per unit volume. In order to develop a quantitative model, it will be assumed that the recrystallized grains are of cylindrical shape. Each grain reaches a certain radius,  $R_0$ , soon after nucleation. Once the grain has achieved this radius, its radius does not increase. Thus, soon after nucleation the recrystallized grain grows in a one dimensional fashion such that its length increases with time, while the radius remains constant. It will be further assumed that the longitudinal growth of the recrystallized grains takes place at a constant rate,  $G_L$ . Thus

$$l = G_L \cdot t \quad (4.19)$$

where  $t$  is the annealing time and  $l$  is the length of a recrystallized grain.

For this special case, the parameters in the model developed in section 3.2 take the following values:

$$\begin{aligned} P &= 0; \quad Q = 1; \quad a = 0 \\ \{N &= 0; \quad \omega = \beta = 1 \quad \} \\ K_V &= \pi; \quad K_{S1} = K_{S2} = 2\pi \end{aligned} \quad (4.20)$$

For these values of the parameters, equations (3.33) and (3.36) give the following results:

$$V_{V_{ex}} = (\pi R_0^2 N_V G_L) t \quad (4.21)$$

and



$$S_{V_{ex}} = 2\pi R_0^2 N_{V_0} + (2\pi R_0 N_{V_0})t \quad (4.22)$$

Combining equations (4.21) and (4.22) gives

$$S_{V_{ex}} = (2\pi R_0^2 N_{V_0}) + \frac{2}{R_0} V_{V_{ex}} \quad (4.23)$$

Furthermore,

$$(\bar{v}_S)_{ex} = \frac{1}{2} \left[ \frac{1}{\frac{1}{G_L} + \frac{t}{R_0}} \right] \quad (4.24)$$

To compare the predictions of the model with the experimental behavior, it is necessary to solve the impingement problem. This can be done as follows.

Figure 4.1 shows a plot of  $\left(\frac{S_V}{1-V_V}\right)$  vs.  $V_V$  for the experimental data. The behavior can be satisfactorily described by a straight line. Thus we have the following empirical equation:

$$S_V = (1 - V_V)(a V_V + b) \quad (4.25)$$

where  $a$  and  $b$  are constants and  $V_V$  and  $S_V$  are the volume fraction and surface area of the recrystallized regions. The values of  $a$  and  $b$  for different values of prestrains are given in Table 4.1. Note that  $a$  does not depend on the prestrain but  $b$  systematically increases with the prestrain. It is not possible to verify equation (4.25) for other annealing temperatures because English and Backofen have not presented their surface area data at other

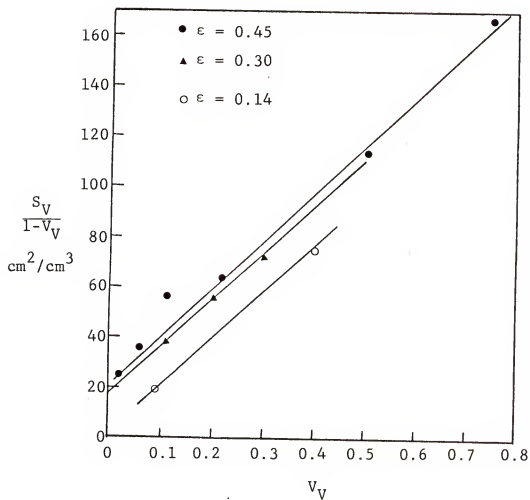


Fig. 4.1. A graph of  $\frac{S_V}{1-V_V}$  vs.  $V_V$  at 812°C.

Table 4.1  
Annealing Temperature: 812°C

Prestrain	b	cm <sup>2</sup> /cm <sup>3</sup>	a	cm <sup>2</sup> /cm <sup>3</sup>
0.14		3		193.33
0.30		18		193.33
0.45		21		193.33

annealing temperatures. However, equation (4.25) can be used to evaluate the impingement function at 812°C. Combining equations (4.25), (4.22), (3.115) and (3.116) gives the following result for the functional form of the impingement function,  $\psi(V_V)$ :

$$\psi(V_V) = (1 - V_V)^2 \quad (4.26)$$

Strictly speaking, this impingement function should be used only for the annealing temperature, 812°C [since only the data at 812°C were used to obtain equation (4.25)]. However, it may be said that the impingement function is not expected to change with the annealing temperature; thus equation (4.26) will be used for all the experimental data.

Equations (4.26), (3.115) and (3.116) give the following results:

$$\frac{V_V}{1-V_V} = V_{V_{ex}} \quad (4.27)$$

$$\frac{S_V}{(1-V_V)^2} = S_{V_{ex}} \quad (4.28)$$

$$\text{and} \quad (\bar{v}_S) = (\bar{v}_S)_{ex} \quad (4.29)$$

Substituting equations (4.27) and (4.28) into (4.23) gives

$$\frac{S_V}{(1-V_V)} = \left[ \left\{ \frac{2}{R_0} - 2\pi R_0^2 N_{V_0} \right\} V_V + 2\pi R_0^2 N_{V_0} \right] \quad (4.30)$$

Since  $R_0$  and  $N_{V_0}$  are constants for given temperature and prestrain, comparing equations (4.25) and (4.30) gives

$$a = \frac{2}{R_0} - 2\pi R_0^2 N_{V_0} \quad (4.31)$$

$$\text{and} \quad b = 2\pi R_0^2 N_{V_0} \quad (4.32)$$

Solving these equations for  $R_0$  and  $N_{V_0}$  gives

$$R_0 = \frac{2}{(a+b)} \quad (4.33)$$

$$\text{and} \quad N_{V_0} = \frac{b(a+b)^2}{8\pi} \quad (4.34)$$

Using equations (4.33) and (4.34) together with Table 4.1 gives the following results:

Table 4.2 Annealing Temperature: 812°C		
Prestrain	$R_0$ (cm)	$N_{V_0}$ per $\text{cm}^3$
0.14	$100 \times 10^{-4}$	$0.48 \times 10^4$
0.30	$94.7 \times 10^{-4}$	$3.19 \times 10^4$
0.45	$93.4 \times 10^{-4}$	$3.83 \times 10^4$

Note that  $R_0$  does not change appreciably with the pre-strain but  $N_{V_0}$  increases as the prestrain increases. This is expected because the number of active nucleation sites should increase with increasing strain. The higher prestrain gives rise to a finer grain structure after recrystallization. However,  $R_0$  is determined by the grain structure of the cold worked matrix (it is proportional to the average grain face area); thus it is not expected to vary with the prestrain or annealing temperature. In all the subsequent calculations, a value of  $94 \times 10^{-4}$  cm will be used for  $R_0$ .

Combining equations (4.24) and (4.29) and using  $R_0$  equal to  $94 \times 10^{-4}$  cm gives

$$\bar{v}_S = \frac{1}{\frac{1}{2G_L} + \frac{(4.67 \times 10^{-3})}{t}} \quad (4.35)$$

This behavior of  $\bar{v}_S$  is predicted by the model is in excellent agreement with the experimental behavior described by the empirical equation (4.18). For comparison, equation (4.18) is given as follows:

$$(\bar{v}_S) = \frac{1}{\frac{1}{G} + \frac{4 \times 10^{-3}}{t}} \quad (4.18)$$

Thus,

$$G = 2G_L \quad (4.36)$$

Since  $G_L$  depends on the annealing temperature,  $G$  should also depend on the annealing temperature. This is precisely what is observed. On the other hand, the coefficient of  $(1/t)$  in the equation (4.35) is  $(\frac{R_0}{2})$  and hence it is not expected to change with the prestrain or annealing temperature. Again, this is in excellent agreement with the observed behavior.

Combining equations (4.21) and (4.27) gives

$$\frac{V_V}{1-V_V} = [\pi R_0^2 N_{V_0} G_L] t \quad (4.37)$$

Substituting equation (4.32) into (4.37) gives

$$\frac{V_V}{1-V_V} = [2bG_L] t \quad (4.38)$$

Since the quantity in the square bracket is independent of time, the model predicts that the plot of  $(\frac{V_V}{1-V_V})$  vs.  $t$  should be linear and the straight line should pass through the origin. Figure 4.2 shows a plot of  $\frac{V_V}{1-V_V}$  vs.  $t$  for the experimental data at 812°C. The plot is linear and the straight line goes through the origin. Thus the experimental behavior is in excellent agreement with the predictions of the model. Let  $t_0$  be the time required for total recrystallization. Then, equation (4.38) gives

$$0.11 = [2bG_L] t_0 \quad (4.39)$$

Substituting equation (4.39) into (4.38) gives

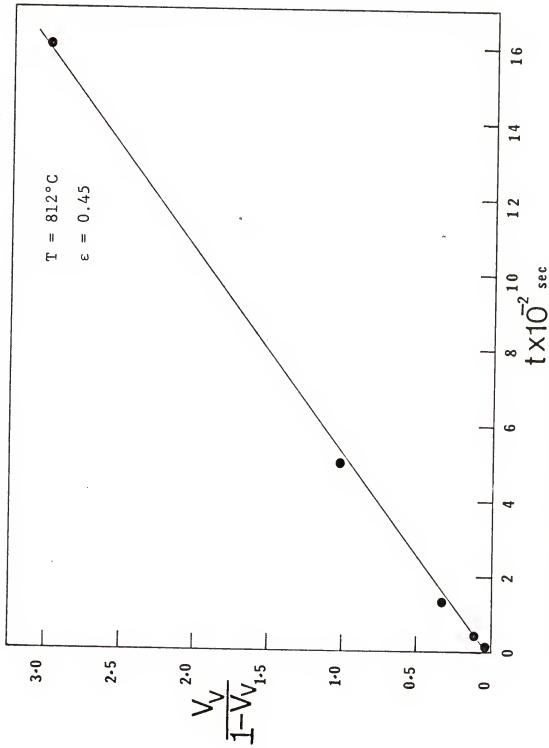


Figure 4.2 A graph of  $\{V_V/(1-V_V)\}$  vs.  $t$ .

$$\frac{V_V}{1-V_V} = 0.11 \left[ \frac{t}{t_0} \right] \quad (4.40)$$

Thus, the model predicts that a plot of  $\left[ \frac{V_V}{1-V_V} \right]$  vs.  $\left( \frac{t}{t_0} \right)$  should be linear and the data points at all the prestrains and annealing temperatures should fall on a single straight line of slope 0.111. Furthermore, the straight line should pass through the origin. Figure 4.3 shows such a plot for the experimental data at various prestrains and annealing temperatures. Again the agreement between the experimental behavior and prediction of the model is very good. Equation (4.39) can now be used to evaluate the values of the growth rate constant,  $G_L$ , if  $b$  is known. Table 4.1 gives values of  $b$  at three prestrains. It may be assumed that  $b$  is independent of temperature. The values of  $G_L$  evaluated in this manner are given in the Table 4.3. The first three values of  $G_L$  in Table 4.3 can be used to evaluate the activation energy for the growth process (this is because the prestrain is not very different for these data). A plot of  $\ln G_L$  vs.  $1/T$  is shown in Figure 4.4. The plot is linear, indicating an Arrhenius nature of the temperature dependence of  $G_L$ . The activation energy may be evaluated from the slope of this plot and the calculated value is



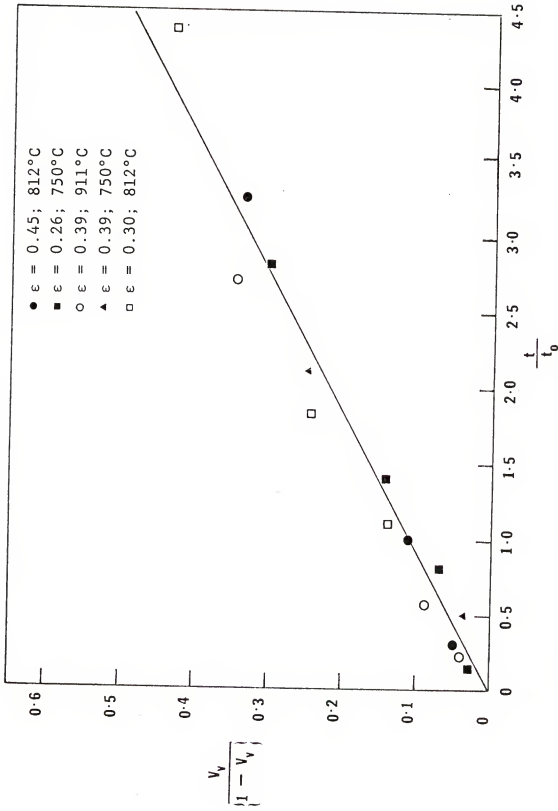


Figure 4.3 A graph of  $V_v/(1-V_v)$  vs.  $t/t_0$  at different annealing temperatures and prestrains.

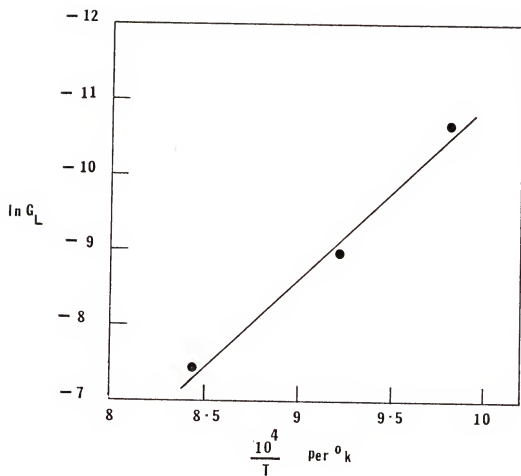


Figure 4.4. An Arrhenius plot of  $\ln G_L$  vs.  $1/T$ .

Table 4.3

Prestrain	Annealing Temperature °C	$G_L$ cm/sec
0.39*	750	$0.230 \times 10^{-4}$
0.45	812	$1.32 \times 10^{-4}$
0.39*	911	$5.87 \times 10^{-4}$
0.26**	750	$0.086 \times 10^{-4}$
0.30	812	$0.56 \times 10^{-4}$

\*b value assumed to be same as that for the pre-strain of 0.45

\*\*b value assumed to be same as that for the pre-strain of 0.30

as follows:

$$\left\{ \begin{array}{l} \text{Activation energy} \\ \text{for growth} \end{array} \right\} = Q_G = 47 \text{ K cal/mole}$$

This simple model explains all the experimental behavior quantitatively. The analysis clearly demonstrates the applicability of the present approach. A similar experimental behavior has been observed in some other recrystallization studies [93,94] and can be explained by using the present approach. The next two chapters deal with the experimental studies done during the present work, and it will again be shown that this approach is very successful in analyzing the experimental data.

## CHAPTER V NUCLEATION AND GROWTH OF AUSTENITE FROM PEARLITE

### 5.1 Introduction:

The formation of austenite has been studied in much less detail than its decomposition. The previous investigations are not entirely satisfying. In some of the studies, quantitative data is not available, while in other cases there are some contradictions.

This chapter deals with an experimental investigation of the formation of austenite from pearlite in a eutectoid Fe-C alloy. A brief survey of the previous work is presented in the first section and the subsequent sections deal with the experimental work and data analysis.

### 5.2 Literature Survey:

A study of the austenitization of pearlite was carried out by Roberts and Mehl [105] in eutectoid steels. They concluded that the overall transformation could be described satisfactorily by a constant nucleation and growth rate model. Speich and Szirmai [106] studied formation of austenite from pearlite in hypereutectoid Fe-C alloys. They claim that the nucleation of austenite

occurs preferentially at the intersections of the pearlite colonies. The following observations were made by Speich and Szirmai [106].

(1) The relationship between the volume fraction of austenite,  $V_V^Y$ , and its surface area,  $S_V^Y$ , could be described by an empirical equation:

$$S_V^Y = A_1 V_V^Y [1 - V_V^Y] - A_2 \{V_V^Y (1 - V_V^Y)\}^2 \quad (5.1)$$

where  $A_1$  and  $A_2$  depend on temperature but not on the volume fraction.

(2) The surface area averaged interface velocity was found to be constant at a given austenitizing temperature.

(3) The time dependence of the volume fraction could be described by the following equation:

$$V_V^Y = 1 - \text{Exp}\{-B_1 t^3\} \quad (5.2)$$

where  $B_1$  is a kinetic constant. From these three observations Speich and Szirmai concluded that the transformation takes place by the site saturation of the austenite nuclei along intersections of the pearlite colonies and the subsequent three dimensional growth of the nuclei at a constant rate.

Note that equation (5.2) assumes a random impingement. For such a case of site saturated three dimensional growth, the model developed in section 3.2 gives

$$\frac{S_V^\gamma}{(1-v_V^\gamma)} = S_{V_{ex}}^\gamma = B_2 t^2 \quad (5.3)$$

where  $B_2$  is a kinetic constant. Thus a plot of  $\ln\left\{\frac{S_V^\gamma}{(1-v_V^\gamma)}\right\}$  vs.  $\ln t$  should be linear with a slope of 2.0. Such a plot for Speich and Szirmai's data [106] was found to be linear but the slope was observed to be 0.90 instead of 2.0. Furthermore, the surface area averaged interface velocity,  $\bar{v}_S$ , calculated from equations (5.1) and (5.2) was found to increase systematically with time, increasing almost by one order of magnitude. Thus the conclusions reached by Speich and Szirmai [106] need to be re-examined.

Karlson [107] has studied the transformation kinetics of the austenitization process in Fe-0.18%C alloy at 855°C. It was observed that pearlite transforms to austenite in less than one second and the further growth of austenite occurs by consumption of ferrite by the existing austenite grains. Karlson [107] concluded that diffusion of carbon through austenite is the rate controlling step.

The formation of austenite has been studied by several other workers [108-112] but most of these papers deal with either the effect of rapid heating on the forma-

tion of austenite or the experiments are done on steels with significant amounts of alloying elements. A review article on the austenitization process is given by Paxton [113].

### 5.3 Experimental Work:

The experiments were done on Fe-0.83%C alloy supplied by Bethlehem Steel Corporation. The alloy composition is given in Table 5.1.

Table 5.1  
Alloy Composition

<u>Element</u>	<u>Wt. Percent</u>	<u>Element</u>	<u>Wt. Percent</u>
C	0.83	Mo	0.04
Mn	<0.01	Cu	0.001
Si	<0.002	Sn	<0.002
S	<0.01	Al	<0.015
Cr	0.01	Ti	<0.001
Ni	<0.01	N	0.001

The alloy was homogenized at 1000°C for three days. Zirconium chips were used to minimize the oxidation and decarburization during the homogenizing treatment. Three samples were cut from the different portions of the homogenized bars and were polished for the microscopic exam-

ination. All the samples were found to be completely pearlitic and there were no concentration gradients.

The homogenized bar was machined from  $\frac{1}{2}$ " to  $\frac{1}{4}$ " diameter and the samples of 1/16" thickness were cut from the  $\frac{1}{4}$ " diameter rod. These samples were used for the experimental work.

#### 5.3.1 Starting Structure for the Austenitization Studies

A uniform interlamellar spacing was produced in the samples by the following heat treatment.

The specimens were austenitized at 850°C for fifteen minutes in a salt bath furnace and then quickly transferred to another salt bath at 680°C. The samples were kept at this temperature for twenty minutes and then quenched in iced brine. The salt baths were sprinkled with graphite powder to avoid decarburization.

Three samples were polished and nital etched. The structure of these samples was found to be completely pearlitic. The pearlite spacing was observed to be uniform and the same in all three samples.

#### 5.3.2 Austenitization Experiments

The specimens were austenitized at 750°C for various times in a salt bath furnace and then quenched in iced brine. The temperature control of the furnace was



approximately  $\pm 2^{\circ}\text{C}$ . The procedure was repeated at  $730^{\circ}\text{C}$  and  $740^{\circ}\text{C}$ . The experiments had to be repeated several times to get well-spaced austenitization times and uniform microstructures.

#### 5.4 Metallography:

Each sample was cut in the middle and mounted "edge on." This "edge on" mounting was done to avoid any surface effects. The polishing was done by the standard polishing and grinding techniques. The final wheel polishing was done by using 6 micron diamond paste. Before etching, each sample was examined under the microscope. The relief between pearlite and martensite was small. The samples were etched with a 2% nital solution. The representative microstructures are shown in Figures 5.1 to 5.3.

It was observed that the austenite grains form uniformly in the pearlite matrix and at low volume fractions the microstructure on the section is typically one of the polydispersed spheres distributed in the matrix. Some cementite was left even after the completion of the austenitization process. In most of the cases, this residual cementite was in the form of spherodite rather than lamellar shape. Thus one may conclude that the com-

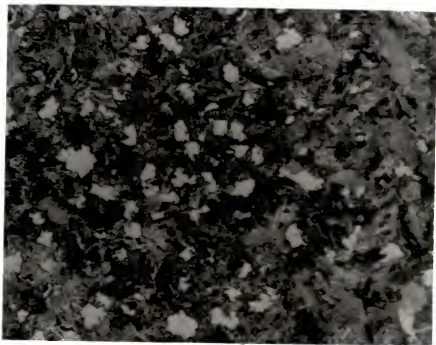


Figure 5.1. A photomicrograph of a sample partially austenitized at 750°C for 23 sec.

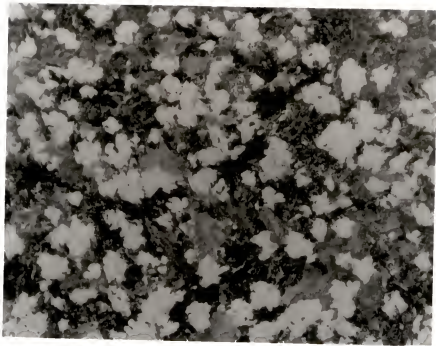


Figure 5.2. A photomicrograph of a sample partially austenitized at 750°C for 32 sec.

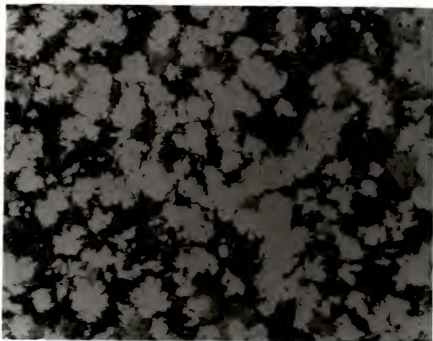


Figure 5.3. A photomicrograph of a sample partially austenitized at 750°C for 45 sec.

position of austenite at the end of the austenitization process is not uniform.

The volume fraction and surface area of martensite (which was austenite at the reaction temperature) was measured in each sample by using the standard stereological techniques. The measurements were carried out manually. The image was projected on the T.V. screen of the Quantimet 720 and the measurements were performed by superimposing a grid. At least fifty grid placements were used in each sample. The volume fraction was measured by point counting while the surface area was measured by the line intercept count. The measured values of the volume fraction and surface area of austenite are given in Tables 5.2 to 5.4.

### 5.5 Data Processing:

In this case, one may assume that the impingement is random. Thus, it is possible to evaluate the extended properties by using equations (2.15) and (2.16). The extended properties evaluated in this manner are given in Tables 5.2 to 5.4.

A plot of  $S_V^Y$  vs.  $V_V^Y$  is shown in Figure 5.4. The plot is nonlinear. Such a plot is expected to be linear for a two or one dimensional growth [see equations (3.77)]

Table 5.2  
Global Properties of Austenite  
Austenitizing Temperature: 750°C

No.	Austenitizing time (sec.)	$V_V^\gamma$	$S_V^\gamma \text{ cm}^2/\text{cm}^3$	$V_V^\gamma$	$S_V^\gamma \text{ cm}^2/\text{cm}^3$
1	23	0.10	299	0.11	332
2	26	0.15	392	0.16	461
3	29	0.22	533	0.25	683
4	32	0.32	606	0.39	891
5	35	0.41	677	0.53	1148
6	38	0.53	711	0.76	1513
7	41	0.67	628	1.11	1905
8	45	0.78	509	1.51	2317

Table 5.3  
Global Properties of Austenite  
Austenitizing Temperature: 740°C

No.	Austenitizing time (sec.)	$V_V^Y$	$S_V^Y \text{ cm}^2/\text{cm}^3$	$V_{ex}^Y$	$S_{Vex}^Y \text{ cm}^2/\text{cm}^3$
1	40	0.10	236	0.110	262
2	50	0.16	412	0.170	490
3	60	0.35	581	0.430	893
4	70	0.53	648	0.76	1378
5	80	0.70	576	1.2	1920
6	90	0.87	381	2.04	2930

Table 5.4  
Global Properties of Austenite  
Austenitizing Temperature: 730°C

No.	Austenitizing time (sec.)	$V_V^Y$	$S_V^Y$ cm <sup>2</sup> /cm <sup>3</sup>	$V_{Vex}^Y$	$S_{Vex}^Y$ cm <sup>2</sup> /cm <sup>3</sup>
1	165	0.12	200	0.13	226
2	180	0.08	190	0.08	206
3	210	0.14	246	0.15	292
4	240	0.20	360	0.22	450
5	300	0.43	480	0.56	843
6	420	0.86	404	2.0	2890



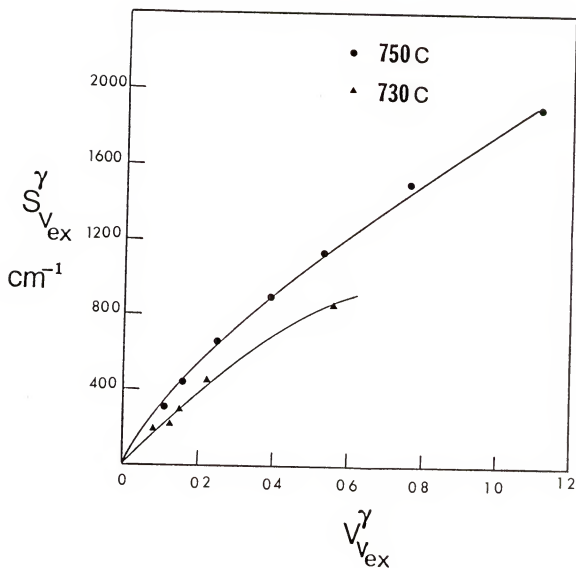


Figure 5.4. A graph of  $S_{Vex}^{\gamma}$  vs.  $V_{Vex}^{\gamma}$  during austenitization of pearlite.

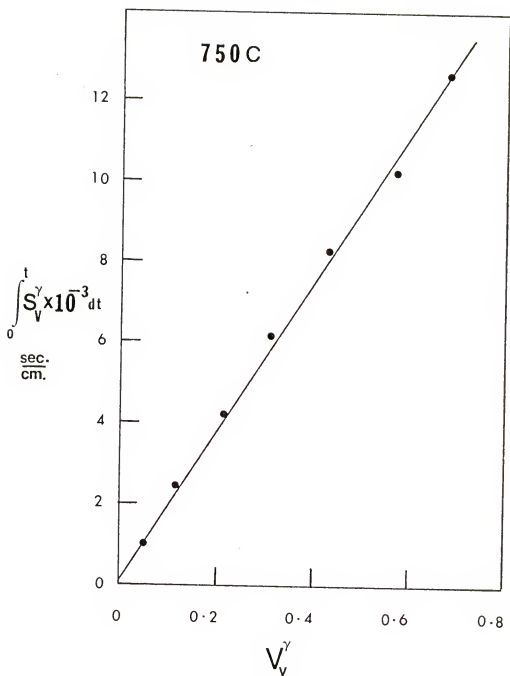


Figure 5.5. A graph of  $\int_0^t S_V^\gamma dt$  vs.  $V_V^\gamma$  at 750°C.

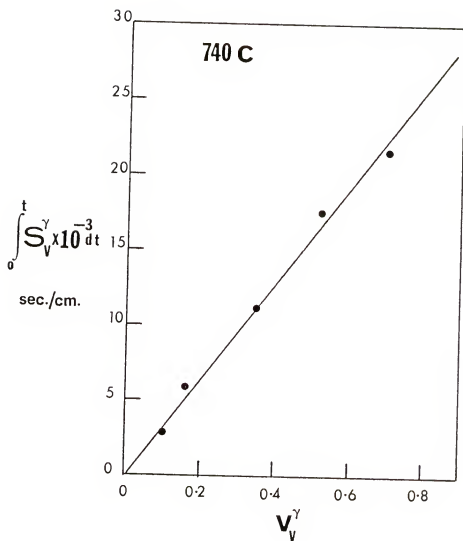


Figure 5.6. A graph of  $\int_0^t S_V^\gamma dt$  vs.  $V_V^\gamma$  at 740°C.

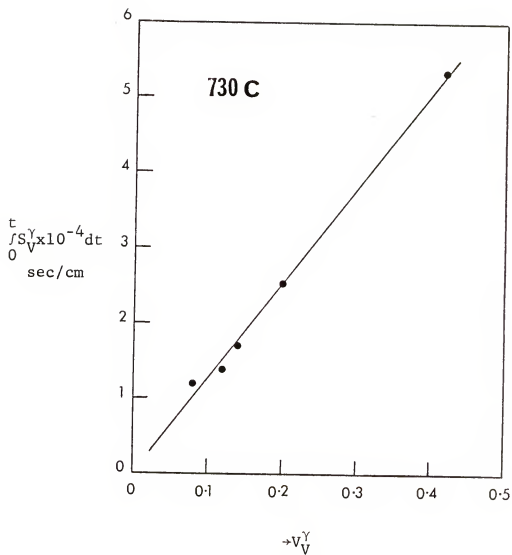


Figure 5.7. A graph of  $\int_0^t S_V^\gamma dt$  vs.  $V_V$  at 730°C.

and (3.90)]. Thus, it may be concluded that the austenite growth occurs in a three dimensional manner.

A plot of  $\int_0^t S_V^Y dt$  vs.  $V_V^Y$  was found to be linear at all three austenitizing temperatures. These plots are shown in Figures 5.5 to 5.7. The slope of the straight line changes with the austenitizing temperature. Thus, we have the following empirical equation:

$$\int_0^t S_V^Y dt = \alpha(T) \cdot V_V^Y \quad (5.4)$$

where  $\alpha(T)$  does not depend on the time but it decreases as the austenitizing temperature increases.

A plot of  $\{S_{V_{ex}}^Y / t^2\}$  vs.  $t$  is shown in Figures 5.8 to 5.10. This plot is also linear at all the austenitizing temperatures. Thus, the following empirical equation describes the time dependence of the extended surface area.

$$S_{V_{ex}}^Y = t^2 [B_1^Y + B_2^Y t] \quad (5.5)$$

where  $B_1^Y$  and  $B_2^Y$  depend on the temperature. Table 5.5 gives the values of  $\alpha(T)$ ,  $B_1^Y$  and  $B_2^Y$  at different austenitizing temperatures.

#### 5.6 Data Analysis:

The nonlinear plot of  $V_{V_{ex}}^Y$  vs.  $S_{V_{ex}}^Y$  (see Figure 5.4)

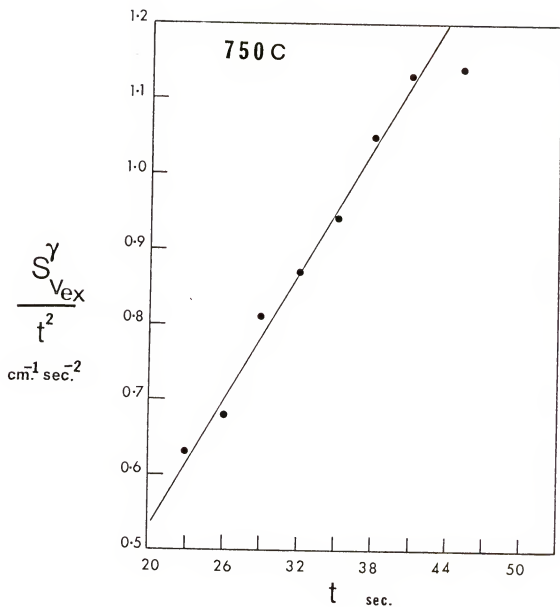


Figure 5.8. A graph of  $S_{Vex}^{\gamma} / t^2$  vs.  $t$  at 750°C.

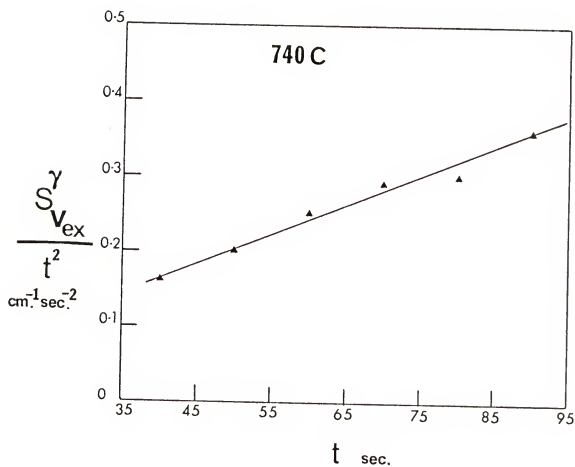


Figure 5.9. A graph of  $S_{V_{ex}}^{\gamma} / t^2$  vs.  $t$  at 740°C.

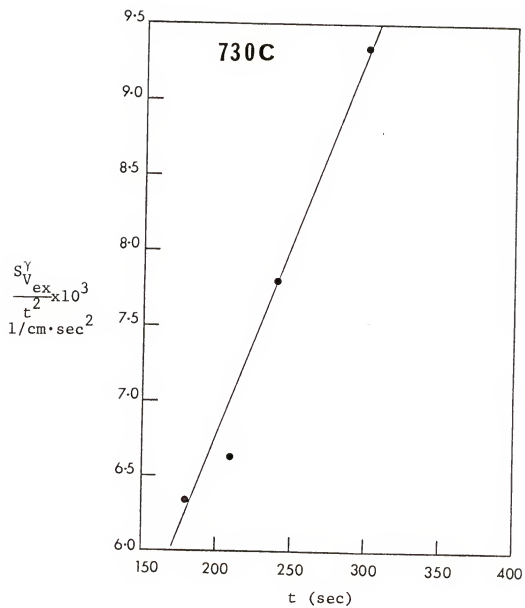


Figure 5.10. A graph of  $S_V^Y / t^2$  vs. t at 730°C.



Table 5.5

Austenitizing Temperature °C	$\alpha(T)$ sec/cm	$B_1^Y$ 1/cm-sec <sup>2</sup>	$B_2^Y$ 1/cm-sec <sup>3</sup>
730	$1.248 \times 10^5$	$0.102 \times 10^{-3}$	$0.036 \times 10^{-3}$
740	$3.2 \times 10^4$	$1.35 \times 10^{-3}$	$4.023 \times 10^{-3}$
750	$1.83 \times 10^4$	0.0528	0.026

indicates that the austenite growth is three dimensional. Since the matrix (pearlite) composition is not expected to change during the process, it can be said that the austenite growth rate is only size dependent. Thus, equation (3.47) can be used to deduce the mathematical form of the austenite growth rate. This can be done as follows.

Equation (5.4) can be rewritten in the following form:

$$\int_0^t S_V^Y dt = \alpha(T) \int_0^t \frac{dV_V^Y}{dt} dt \quad (5.6)$$

Substituting equations (2.15) and (2.16) into this equation yields

$$\int_0^t e^{-V_V^Y} \{S_{V_{ex}}^Y - \alpha(T) \frac{dV_{V_{ex}}^Y}{dt}\} dt = 0 \quad (5.7)$$

Equation (5.7) can be satisfied for any arbitrary value of  $t$  only if the integrand is identically equal to zero.

Thus,

$$S_{V_{ex}}^{\gamma} - \alpha(T) \frac{dV_{V_{ex}}^{\gamma}}{dt} = 0$$

$$\text{or} \quad \int_0^t S_{V_{ex}}^{\gamma} dt = \alpha(T) V_{V_{ex}}^{\gamma} \quad (5.8)$$

Now, equation (3.47) gives

$$\int_0^t V(t-\tau) S_{V_{ex}}^{\gamma}(\tau) d\tau = \int_0^t S(t-\tau) V_{V_{ex}}^{\gamma}(\tau) d\tau \quad (3.74)$$

Integrating the left-hand side of this equation by parts yields

$$\int_0^t \left( \frac{\partial V(t-\tau)}{\partial t} \right)_{\tau} \cdot \int_0^{\tau} S_{V_{ex}}^{\gamma}(\tau) d\tau d\tau = \int_0^t S(t-\tau) V_{V_{ex}}^{\gamma}(\tau) d\tau \quad (5.9)$$

Substituting equation (5.8) into (5.9) gives

$$\int_0^t V_{V_{ex}}^{\gamma}(\tau) [S(t-\tau) - \alpha(T) \left( \frac{\partial V(t-\tau)}{\partial t} \right)_{\tau}] d\tau = 0 \quad (5.10)$$

Since the expression in the square bracket is a function of  $(t-\tau)$  only, the integrand has to be identically equal to zero if equation (5.10) is to be satisfied at any value of time,  $t$ . Thus

$$S(t-\tau) - \alpha(T) \left( \frac{\partial V(t-\tau)}{\partial t} \right)_{\tau} = 0$$

or

$$\frac{1}{S(t-\tau)} \left[ \frac{\partial V(t-\tau)}{\partial t} \right]_{\tau} = \frac{1}{\alpha(T)} \quad (5.11)$$

The expression on the left-hand side of equation (5.11) is the surface area averaged interface velocity of one particle (nucleated at time  $\tau$ ). The expression is valid for any value of  $\tau$ ; thus it is valid for all the particles.

It has already been deduced that the growth is three dimensional. It can be qualitatively deduced from the microstructures that the austenite particles have a spherical shape. Let  $R$  be the radius of the austenite particle at time  $t$  whose nucleation time is  $\tau$ . One can write

$$V(t-\tau) = \frac{4\pi}{3} R^3 \quad (5.12)$$

and

$$S(t-\tau) = 4\pi R^2 \quad (5.13)$$

Equations (5.12) and (5.13) give

$$\frac{1}{S(t-\tau)} \left[ \frac{\partial V(t-\tau)}{\partial t} \right]_{\tau} = \left[ \frac{dR}{dt} \right]_{\tau} \quad (5.14)$$

Combining equations (5.11) and (5.14) yields

$$\left[ \frac{dR}{dt} \right]_{\tau} = \frac{1}{\alpha(T)} \quad (5.15)$$

Thus the austenite growth occurs at a constant growth rate and its value at a particular temperature is given by  $(1/\alpha(T))$ . Thus, we have deduced the growth rate of austenite from only the time variation of the volume frac-

tion and surface area without any knowledge or assumption regarding the nucleation rate. To the best knowledge of the author, this has never been done before. The result clearly demonstrates the potential and applicability of equations (3.47) to (3.49) developed in the third chapter.

The nucleation rate,  $\dot{N}(t)$ , will now be evaluated. For a particle nucleated at  $t = 0$ , equations (5.13) and (5.15) give the following result:

$$S(t) = \frac{4\pi}{[\alpha(T)]^2} \cdot t^2 \quad (5.16)$$

Taking the Laplace transform of both the sides of this equation yields

$$L\{S(t)\} = \frac{8\pi}{[\alpha(T)]^2} \cdot \frac{1}{s^3} \quad (5.17)$$

Note that  $S$  on the right-hand side of this equation is the parameter of the Laplace transform and it should not be confused with the surface area.

Similarly, equation (5.5) gives

$$L\{S_{\text{ex}}^Y(t)\} = \frac{2B_1^Y}{s^3} + \frac{6B_2^Y}{s^4} \quad (5.18)$$

Combining equations (3.48), (5.17) and (5.18) yields

$$\dot{N}(t) = \frac{\alpha [ \langle T \rangle ]^2}{8\pi} L^{-1} \left\{ 2B_1^Y + \frac{6B_2^Y}{s} \right\} \quad (5.19)$$

or

$$\dot{N}(t) = \frac{[\alpha(T)]^2}{4\pi} \{B_1^\gamma \delta(t) + 3B_2^\gamma\} \quad (5.20)$$

where  $\delta(t)$  is the delta function and it is identically equal to zero for  $t < 0$ . Thus for  $t \geq 0$ , one can write

$$\dot{N}(t) = \frac{3[\alpha(T)]^2}{4\pi} B_2^\gamma \quad (5.21)$$

Thus, the nucleation rate is constant and its value is given by equation (5.21). The values of the nucleation rate and growth rate, evaluated by using equations (5.21) and (5.15), are given in Table 5.6

Table 5.6

Temperature °C	Growth rate cm/sec	Nucleation rate 1/cm <sup>3</sup> -sec
730	$0.80 \times 10^{-5}$	$1.34 \times 10^5$
740	$0.31 \times 10^{-4}$	$9.8 \times 10^5$
750	$0.55 \times 10^{-4}$	$20 \times 10^5$

Brandt [114] has solved the diffusion equations for the growth of pearlite, assuming that the volume diffusion of carbon is the rate controlling process. For the alloy of eutectoid composition, similar technique can be used to evaluate the growth rate of austenite from pearlite. This method was used by Speich and Richards [116] to

evaluate the growth rate of austenite between 820°C and 900°C. Evaluation of the growth rate by using this technique requires a solution to four nonlinear simultaneous equations and it gives a complicated expression for the temperature dependence of the austenite growth rate. However, at a given temperature a constant growth rate is predicted, which is in agreement with the present experimental observations.

#### 5.7 Conclusions:

(1) The growth rate of austenite was deduced from the time variation of its volume fraction and surface area, without any knowledge or assumptions regarding the nucleation rate. The result clearly demonstrates the potential and the practical feasibility of the present approach.

(2) The austenite growth rate was found to be constant at a given temperature.

(3) The nucleation rate of austenite was evaluated from the time dependence of its extended surface area. The nucleation rate was found to be constant at a given temperature.

CHAPTER VI  
FORMATION OF AUSTENITE FROM "SPHERODIZED" CEMENTITE  
AND FERRITE AGGREGATES

6.1 Introduction:

There are very few experimental studies on the formation of austenite from spherodized cementite structures. These previous investigations are incomplete and inconclusive. This chapter deals with the experimental study of the formation of austenite from spherodized cementite structures, in a eutectoid Fe-C alloy. The investigation clearly demonstrates the effect of "geometry" on the kinetic and kinematics of the phase transformation. The experiments were carried out on three different initial distributions of spherodized cementite and at three different austenitizing temperatures. The data are analyzed in a systematic manner (which is the most serious weakness of the previous studies) by using the approach developed in the previous chapters. A brief literature survey is presented in the first section. The second section deals with the experimental work; the subsequent sections are concerned with the data processing and analysis.

## 6.2 Literature Survey:

Roberts and Mehl [105] studied nucleation and growth of austenite from spherodized cementite structures. They observed that the nucleation of austenite does not occur at every carbide particle because a single austenite grain may envelope several carbide particles. Roberts and Mehl [105] observed that the ferrite grain boundaries play a very important role in the austenitization of the spherodized cementite structures. A qualitative description of the austenitization process is given by Bain [117]. Molinder [118] studied austenitization of a spherodized cementite structure in 1.27 wt.% carbon steel. Molinder [118] concluded that the process is interface controlled. The kinetics of austenitization process was studied by Neizweidz, Partom, Taub and Weiss [119] in a graphitic steel. The transformation was studied by measuring the volume fraction of austenite and cementite at various times during the process. The data, on volume fraction of austenite, were analyzed by using an equation of the type

$$V_V = 1 - \text{Exp}\{-Bt^n\} \quad (6.1)$$

The values of  $n$  varied from 0.8 to 1.74 during different stages of the transformation at a given temperature.



Their volume fraction data were reanalyzed during the present work and it was found that following simple equation describes the time variation of the volume fraction of austenite:

$$\frac{V_V}{(1-V_V)} = B_1 t \quad (6.2)$$

where  $B_1$  is a function of temperature only. It was shown in the previous chapters that if the impingement function is described by  $(1-V_V)^2$ , then

$$V_{V_{ex}} = \frac{V_V}{1-V_V} \quad (6.3)$$

Combining equations (6.2) and (6.3) gives

$$V_{V_{ex}} = B_1 t \quad (6.4)$$

Thus, under the assumption of equation (6.3), equation (6.4) describes a linear relationship between the extended volume fraction of austenite and time. Equation (6.4) may be interpreted as the site saturated two dimensional parabolic growth of austenite. Thus, the complicated numerical solution to the diffusion problem, presented by Neidzweidz et al. [119], may not be necessary.

Judd and Paxton [120] have studied austenitization of spheroidized cementite and ferrite aggregates in some

low carbon steels. They have developed a mathematical model for the kinetics of dissolution of spherodized cementite. The model does not take into account the geometrical impingement between the growing austenite grains; thus, it is applicable only if the volume fraction of spherodized cementite is small and the interparticle distance is large. Furthermore, the model assumes that the spherodized cementite is in the form of discrete particles. It will be demonstrated that this may not be necessarily true if the cementite is situated at the ferrite grain edges. Judd and Paxton [120] concluded that the volume diffusion of carbon in austenite is the rate controlling step for the process.

Speich and Szirmai [106] studied the formation of austenite from spherodized cementite structure in some Fe-C alloys. They observed that growth of austenite grains is inhibited across the ferrite grain boundaries. This may suggest an orientation-relationship between the austenite and ferrite grains. A review article on the austenitization process is given by Paxton [113].

Mathematical models for dissolution of spherodized cementite, during the austenitization process, have been developed by Neidzweidz, Weiss, Partom and Taub [119] and Judd and Paxton [120]. Molinder [118] has developed a model

for the time variation of the average austenite composition during the process.

### 6.3 Experimental Work:

The experiments were done on the Fe-0.83 wt.% C alloy supplied by Bethlehem Steel Corporation. The composition of the alloy is given in Table 5.1. The homogenization treatment is described in section 5.2. The samples of  $\frac{1}{4}$ " diameter and 1/16" thickness were used for the experiments.

#### 6.3.1 Starting Structure

The samples were austenitized at 850°C for thirty minutes in a salt bath furnace and then quenched in the iced brine. The microstructure of three samples was examined and was found to be completely martensitic. The hardness of each quenched sample was measured on the Rockwell "c" scale and the samples with the average hardness less than Rc. 63 were discarded (the hardness of eutectoid martensite is Rc. 65). The martensitic samples were vacuum sealed in vycor tubes and annealed in a muffle furnace at 690°C to produce the spherodized cementite structures. Three different initial distributions of spherodized cementite were produced by annealing the

samples for different annealing times. The details of annealing times and the letter designations for these starting structures are given in Table 6.1.

Table 6.1  
Annealing Temperature: 690°C

<u>Annealing Time</u>	<u>Letter Designation</u>
1 day	D <sub>1</sub>
1 week	D <sub>2</sub>
1 month	D <sub>3</sub>

### 6.3.2 Austenitizing Experiments

The samples of all the three batches, D<sub>1</sub>, D<sub>2</sub> and D<sub>3</sub>, were partially austenitized at 750°C for various times in a salt bath furnace and then quenched in iced brine. The temperature control of the surface was  $\pm 2^\circ\text{C}$ . The remaining samples of batch D<sub>2</sub> were partially austenitized at 740°C and 760°C for various times and then quenched in iced brine.

### 6.3.3 Metallography

The polishing was done by standard grinding and polishing techniques. The samples were ground through a series of SiC papers to 600 grit and then polished on a polishing wheel with six micron diamond paste. In order

to measure the global properties of cementite phase by using the Quantimet 720, the samples were etched by using the etching procedure [121] described in Table 6.2.

Table 6.2  
Etching Procedure for Etching Spherodized Cementite

Composition of etching solution:

picric acid: 2 gm

Sodium hydroxide: 24.5 gm

Water: 73.5 cc

Etch the sample for ten to fifteen minutes in the boiling etching solution

In the etched structures spherodized cementite was colored dark brown, while ferrite and martensite were unaffected. This etching solution does not etch the ferrite grain boundaries. A typical microstructure revealed in this manner is shown in Figure 6.1. The volume fraction,  $V_V^C$ , surface area,  $S_V^C$ , and total curvature,  $M_V^C$ , of the spherodized cementite was measured in all the samples by using the image analyzing computer, Quantimet 720. Details of the procedure is given elsewhere [56]. The values of the global properties of cementite are given in Tables 6.3 to 6.8. In addition to these global properties, the inverse cumulative intercept distribution of the linear intercepts of cementite phase was measured in each sample. This is explained as follows.

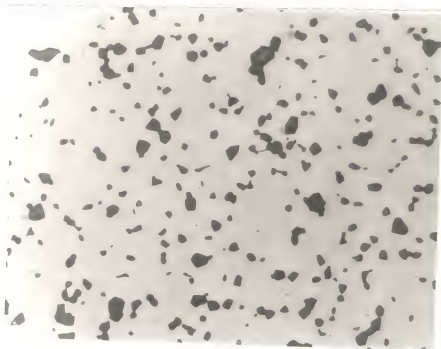


Figure 6.1. A photomicrograph of the starting structure D<sub>3</sub> etched with the boiling sodium picrate solution.

Table 6.3  
Global Properties of Spherodized Cementite in the Starting Structures  
Annealing Temperature: 690°C

Designation	Annealing time	Volume fraction $V_V^C$	Surface area $S_V^C \text{ cm}^2/\text{cm}^3$	Total Curvature $M_V^C \text{ cm}/\text{cm}^3$
D <sub>1</sub>	1 day	0.13	2254	$12 \times 10^6$
D <sub>2</sub>	1 week	0.13	1500	$4.6 \times 10^6$
D <sub>3</sub>	1 month	0.14	1384	$3.94 \times 10^6$

Table 6.4  
Global Properties of Cementite During Austenitization at 750°C  
Starting Structure: D<sub>1</sub>

No.	Austenitizing time (sec)	Volume fraction $V_V^C$	Surface area $S_V^C$ cm <sup>2</sup> /cm <sup>3</sup>	Total curvature $M_V^C$ cm/cm <sup>3</sup>	Mean intercept $\bar{\lambda}_C$ cm	Mean curvature $\bar{H}_C$ Per cm	$\bar{\lambda}^C \bar{H}^C$
1	0	0.130	2254	$12 \times 10^6$	$2.3 \times 10^{-4}$	$5.323 \times 10^3$	1.23
2	20	0.0983	1759	$8.54 \times 10^6$	$2.23 \times 10^{-4}$	$4.85 \times 10^3$	1.08
3	30	0.0763	1427	$7.66 \times 10^6$	$2.14 \times 10^{-4}$	$5.36 \times 10^3$	1.15
4	40	0.0394	743	$4.63 \times 10^6$	$2.12 \times 10^{-4}$	$6.23 \times 10^3$	1.32
5	50	0.0285	555	$3.46 \times 10^6$	$2.06 \times 10^{-4}$	$6.23 \times 10^3$	1.28
6	60	0.0307	585	$3.15 \times 10^6$	$2.1 \times 10^{-4}$	$5.38 \times 10^3$	1.13
7	90	0.0261	581	$3.258 \times 10^6$	$1.8 \times 10^{-4}$	$5.60 \times 10^3$	1.01
8	130	0.0120	220	$1.439 \times 10^6$	$2.18 \times 10^{-4}$	$6.5 \times 10^3$	1.42
9	180	0.010	200	$1.36 \times 10^6$	$2.0 \times 10^{-4}$	$6.8 \times 10^3$	1.36



Table 6.5  
Global Properties of Cementite During Austenitization at 750°C  
Starting Structure: D<sub>3</sub>

No.	Austenitizing time (sec)	Volume fraction $V_V^C$	Surface area $S_V^C$ cm <sup>2</sup> /cm <sup>3</sup>	Total curvature $M_V^C$ cm/cm <sup>3</sup>	Mean intercept $\bar{\chi}_C$ cm	Mean curvature $\bar{H}_C$ Per cm	$\bar{\chi}^C \bar{H}^C$
1	0	0.14	1384	$3.94 \times 10^6$	$4.04 \times 10^{-4}$	$2.84 \times 10^3$	1.15
2	30	0.11	1162	$3.2 \times 10^6$	$3.78 \times 10^{-4}$	$2.75 \times 10^3$	1.04
3	35	0.12	1016	$2.65 \times 10^6$	$4.72 \times 10^{-4}$	$2.60 \times 10^3$	1.23
4	40	0.113	1140	$3.23 \times 10^6$	$4.54 \times 10^{-4}$	$2.37 \times 10^3$	1.07
5	45	0.10	980	$2.615 \times 10^6$	$4.08 \times 10^{-4}$	$2.66 \times 10^3$	1.08
6	50	0.0847	850	$2.3 \times 10^6$	$3.98 \times 10^{-4}$	$2.70 \times 10^3$	1.07
7	65	0.0612	681	$2.15 \times 10^6$	$3.6 \times 10^{-4}$	$3.15 \times 10^3$	1.13
8	90	0.0548	630	$2.05 \times 10^6$	$3.48 \times 10^{-4}$	$3.25 \times 10^3$	1.131
9	150	0.0370	400	$1.22 \times 10^6$	$3.7 \times 10^{-4}$	$3.05 \times 10^3$	1.13

Table 6.6  
Global Properties of Cementite During Austenitization at 750°C  
Starting Structure: D<sub>2</sub>

No.	Austenitizing time (sec)	Volume fraction $V_C$	Surface area $S_V^C$ cm <sup>2</sup> /cm <sup>3</sup>	Total curvature $M_V^C$ cm/cm <sup>3</sup>	Mean intercept $\bar{\lambda}^C$ cm	Mean curvature $H^C$ Per cm	$\bar{\lambda}^C H^C$
1	0	0.13	1500	$4.6 \times 10^6$	$3.46 \times 10^{-4}$	$3.06 \times 10^3$	1.06
2	30	0.104	1143	$3.36 \times 10^6$	$3.64 \times 10^{-4}$	$2.93 \times 10^3$	1.07
3	45	0.0753	915	$2.92 \times 10^6$	$3.3 \times 10^{-4}$	$3.19 \times 10^3$	1.05
4	60	0.046	656	$2.304 \times 10^6$	$2.8 \times 10^{-4}$	$3.51 \times 10^3$	0.983
5	90	0.042	564	$1.81 \times 10^6$	$2.98 \times 10^{-4}$	$3.21 \times 10^3$	0.957
6	120	0.033	406	$1.25 \times 10^6$	$3.25 \times 10^{-4}$	$3.07 \times 10^3$	1.0
7	240	0.017	218	$0.69 \times 10^6$	$3.2 \times 10^{-4}$	$3.16 \times 10^3$	1.01

Table 6.7  
Global Properties of Cementite During Austenitization at 760°C  
Starting Structure: D<sub>2</sub>

No.	Austenitizing time (sec)	Volume fraction $V_V^C$	Surface area $S_V^C$ cm <sup>2</sup> /cm <sup>3</sup>	Total curvature $M_V^C$ cm/cm <sup>3</sup>	Mean intercept $\bar{\lambda}^C$ cm	Mean curvature $H_C$ Per cm	$\bar{\lambda}^C H^C$
1	0	0.13	1500	$4.6 \times 10^6$	$3.46 \times 10^{-4}$	$3.06 \times 10^3$	1.06
2	30	0.0716	826	$2.86 \times 10^6$	$3.46 \times 10^{-4}$	$3.462 \times 10^3$	1.19
3	45	0.058	673	$1.97 \times 10^6$	$3.45 \times 10^{-4}$	$2.927 \times 10^3$	1.01
4	60	0.036	447	$1.51 \times 10^6$	$3.22 \times 10^{-4}$	$3.378 \times 10^3$	1.08
5	90	0.026	330	$1.35 \times 10^6$	$3.15 \times 10^{-4}$	$4.09 \times 10^3$	1.28
6	150	0.015	193	$0.660 \times 10^6$	$3.11 \times 10^{-4}$	$3.42 \times 10^3$	1.06

Table 6.8  
Global Properties of Cementite During Austenitization at 740°C  
Starting Structure: D<sub>2</sub>

No.	Austenitizing time (sec)	Volume fraction $V_V^C$	Surface area $S_V^C$ cm <sup>2</sup> /cm <sup>3</sup>	Total curvature $M_V^C$ cm/cm <sup>3</sup>	Mean intercept $\bar{\lambda}^C$ cm	Mean curvature $\bar{H}^C$ 1/cm	$\bar{\lambda}^C \bar{H}^C$
1	0	0.13	1500	$4.6 \times 10^6$	$3.46 \times 10^{-4}$	$3.06 \times 10^3$	1.06
2	30	0.108	1368	$4.23 \times 10^6$	$3.158 \times 10^{-4}$	$3.09 \times 10^3$	0.98
3	45	0.078	978	$2.94 \times 10^6$	$3.19 \times 10^{-4}$	$3.0 \times 10^3$	0.96
4	50	0.046	654	$2.12 \times 10^6$	$2.81 \times 10^{-4}$	$3.24 \times 10^3$	0.91
5	120	0.0345	463	$1.24 \times 10^6$	$2.98 \times 10^{-4}$	$2.7 \times 10^3$	0.81
6	240	0.021	332	$0.92 \times 10^6$	$2.53 \times 10^{-4}$	$2.8 \times 10^3$	0.81
7	300	0.0168	238	$0.60 \times 10^6$	$2.82 \times 10^{-4}$	$2.52 \times 10^3$	0.70
8	360	0.0138	151	$0.18 \times 10^6$	$3.65 \times 10^{-4}$	$1.2 \times 10^3$	0.44
9	600	0.01	150	$0.23 \times 10^6$	$2.66 \times 10^{-4}$	$1.53 \times 10^3$	0.41

Let  $n_L(\ell)$  be the distribution function of the linear intercepts such that  $n_L(\ell)d\ell$  gives the number of intercepts per unit length of the test line, whose length is between  $\ell$  and  $(\ell + d\ell)$ . The inverse cumulative distribution function of the linear intercepts,  $N_{L>}(\ell)$ , is defined by the following equation:

$$N_{L>}(\ell) = \int_{\ell}^{\ell_m} n_L(\ell)d\ell \quad (6.5)$$

where  $\ell_m$  is the maximum intercept length observed. Thus,  $N_{L>}(\ell)$  is the number of intercepts of length greater than  $\ell$ , per unit length of the test line. It is possible to measure  $N_{L>}(\ell)$  for different values of  $\ell$  by using the Quantimet 720. The  $N_{L>}(\ell)$  function for spherodized cementite was measured in each sample. The values of  $N_{L>}(\ell)$  for different values of  $\ell$  are given in Tables 6.9 to 6.14. If the particles are discrete and have a simple convex shape, then it is possible to evaluate the three dimensional size distribution from the measured  $N_{L>}(\ell)$  [51].

One starting structure (batch  $D_2$ ) was polished and etched with 2% nital and the volume fraction and surface area of the spherodized cementite was measured manually. The sample was repolished and the structure was revealed by the etching procedure described in Table 6.2. The

Table 6.9  
Inverse Cumulative Distribution,  $N_{L>}(\lambda)$ , of Cementite  
in the Starting Structures

$\lambda$ (microns)	$D_1$		$D_2$		$D_3$	
	$N_{L>}(\lambda)$	per cm	$\lambda$ (microns)	$N_{L>}(\lambda)$	$\lambda$ (microns)	$N_{L>}(\lambda)$
0	1127		0	750	0	692
0.9	867		1.23	705	0.70	678
1.87	563		2.46	543	1.23	638
2.79	315		3.69	355	1.75	590
3.71	169		4.92	214	2.63	483
4.66	90		6.15	125	3.50	368
5.42	56.4		7.383	67	4.38	273
6.33	33.8		8.613	39.5	5.25	200
7.22	22.5		9.84	24.3	6.13	141
8.12	9.0		11.07	13.2	7.0	102
					7.88	78
					8.75	56
					11.38	23
					14.88	6.5

Table 6.10  
Measured Values of  $N_{L>}(\lambda)$  Function at  
Different Values of the Intercept Length,  $\lambda$   
Austenitizing temperature: 750°C  
Starting structure:  $D_1$

$t=20$ sec		$t=30$ sec		$t=40$ sec	
$\lambda$ ( $\mu$ )	$N_{L>}(\lambda)$ per cm	$\lambda$ ( $\mu$ )	$N_{L>}(\lambda)$ per cm	$\lambda$ ( $\mu$ )	$N_{L>}(\lambda)$ per cm
0	878.57	0	713.5	0	371.5
0.54	813	0.90	567.2	0.54	336.15
1.08	663	1.80	339	1.08	269
1.62	493	2.70	178	1.62	192.7
2.16	344	3.60	86.6	2.12	132.4
2.70	238	4.50	41	2.70	88.7
3.60	125	5.40	21.9	3.60	45
4.50	66.6	6.30	11.1	4.50	23
5.40	34.7	7.20	6.0	5.40	10.7
6.30	29.6	8.10	3.66	6.30	4.5
7.20	16.5	9.0	2.34	7.20	2.01
8.10	8.5	9.90	1.27	8.10	0.74
9.00	5.0	10.80	0.73	9.0	0.32

Table 6.10 - continued.

t=20 sec			t=30 sec			t=40 sec		
$\bar{\lambda}$ ( $\mu$ )	$N_{L>}(\bar{\lambda})$	per cm	$\bar{\lambda}$ ( $\mu$ )	$N_{L>}(\bar{\lambda})$	per cm	$\bar{\lambda}$ ( $\mu$ )	$N_{L>}(\bar{\lambda})$	per cm
9.90		2.85	11.70		0.37	9.90		0.16
10.80		1.22	12.60		0.23	10.80		0.12
11.70		0.77	13.50		0.19	11.70		0.10
t=50 sec			t=60 sec			t=90 sec		
$\bar{\lambda}$ ( $\mu$ )	$N_{L>}(\bar{\lambda})$	per cm	$\bar{\lambda}$ ( $\mu$ )	$N_{L>}(\bar{\lambda})$	per cm	$\bar{\lambda}$ ( $\mu$ )	$N_{L>}(\bar{\lambda})$	per cm
0		277.5	0		292.2	0		290.5
0.36		266.4	0.36		277.9	0.19		277.5
0.72		239.76	0.72		242.4	0.38		258.75
1.08		199.8	1.08		201.5	0.58		233.75
1.44		162.34	1.44		163.5	0.78		208.75
1.80		123.5	1.80		131.4	0.97		186.25
2.16		94.9	2.16		105.1	1.46		132.50
2.70		61	2.52		84.74	1.94		89.09
3.60		33.9	2.88		64.30	2.43		61.04



Table 6.10 - continued.

t=50 sec		t=60 sec		t=90 sec	
$\lambda$ ( $\mu$ )	$N_{L>}(\lambda)$ per cm	$\lambda$ ( $\mu$ )	$N_{L>}(\lambda)$ per cm	$\lambda$ ( $\mu$ )	$N_{L>}(\lambda)$ per cm
4.50	12.8	3.24	46.80	2.91	43.0
5.40	6.7	3.60	35.04	3.40	28.6
6.30	5.0	4.50	17.53	3.88	20.91
7.20	2.15	5.40	8.80	4.37	14.91
8.10	1.42	6.30	5.84	4.85	11.38
9.00	0.61	7.20	2.0	5.34	7.34

t=180 sec		
$\lambda$ ( $\mu$ )	$N_{L>}(\lambda)$	per cm
0	0	100
0.19	0.19	96.8
0.39	0.39	91.5
0.58	0.58	84.75
0.78	0.78	77.0
0.97	0.97	68.9

Table 6.10 - continued.

$\lambda$ ( $\mu$ )	$N_{L>}(\lambda)$	$t=180$ sec per cm
1.16	61.7	
1.46	53.1	
1.94	37.4	
2.43	25.1	
2.91	16.53	
3.40	8.85	
3.88	5.02	
4.37	3.27	
4.85	1.63	
5.34	1.0	
5.82	0.90	

Table 6.11  
 Measured Values of  $N_{L>}(\lambda)$  Function for  
 Different Values of the Intercept Length,  $\lambda$   
 Austenitizing temperature: 750°C  
 Starting structure:  $D_2$

$\lambda$ ( $\mu$ )	$N_{L>}(\lambda)$ per cm						
	t=30 sec	t=45 sec	t=60 sec	t=90 sec	t=120 sec	t=240 sec	t=240 sec
0	571	457.5	328	282	203	108	
1.25	501.4	361	255	215	167	87.8	
2.5	354.6	239.5	156	133.6	111.2	58.14	
3.75	217.46	147	84.75	78.8	69	35.8	
5.0	129.5	86.78	47.05	46.21	37.52	21.55	
6.25	72.22	50.2	24.35	25.3	22	11.3	
7.5	41.82	27.67	12.16	14.74	9.56	6.35	
8.75	25.35	15.56	6.22	9.23	5.13	2.55	
10	13.74	5.89	4.31	*	*	*	
11.25	*	*	1.40	*	*	*	
12.5	*	*	1.07	*	*	*	
13.75	*	*	0.5	*	*	*	

Table 6.12  
 Measured values of  $N_{L>}(\ell)$  Function for  
 Different Values of the Intercept Length,  $\ell$   
 Austenitizing temperature: 750°C  
 Starting structure: D<sub>3</sub>

$\ell$ ( $\mu$ )	$N_{L>}(\ell)$ per cm					
	t=30 sec	t=50 sec	t=65 sec	t=90 sec	t=150 sec	t=200 sec
0	581	425	340.5	315	200	
0.5	550	404.6	320.07	293	190	
1.0	520.6	381	296.24	268.7	179	
1.5	480.5	352	269.0	236.2	165.4	
2.0	426.5	308.5	238.35	197.5	146.8	
2.5	374.2	263.5	204.30	163.8	128.8	
3.0	348	221	170.25	136	119.8	
3.5	265	178.5	139.61	115	91.2	
4.0	219	143.23	115.77	96.7	75.4	
4.5	178	113	91.94	77.2	61.4	
5.0	146.5	93.5	74.91	66.15	50.4	
5.5	123.8	90	71.0	56.7	42.6	
6.0	102.25	67	44.27	45.7	35.2	

Table 6.12 - continued.

$\ell$ ( $\mu$ )	$N_{L>}(\ell)$ per cm					
	t=30 sec	t=50 sec	t=65 sec	t=90 sec	t=150 sec	t=150 sec
7.0	69.72	49.7	27.24	25.2	24.0	
8.0	40.7	34	10.22	13.8	14.0	
9.0	22.7	21.25	10.22	6.62	8.0	
10.0	17.5	12.75	6.81	3.78	6.0	
12.0	5.81	3.0	1.70	4.0	2.0	
14.0	2.91	*	1.4	1.92	0.50	
16.0	0.58	*	0.5	*	0.10	

\* No measurements performed

Table 6.13  
Measured Values of  $N_{L>}(\lambda)$  Function for  
Different Values of the Intercept Length,  $\lambda$   
Austenitizing temperature: 740°C  
Starting structure:  $D_2$

$\lambda$ ( $\mu$ )	$N_{L>}(\lambda)$ per cm							
	t=30 sec	t=45 sec	t=60 sec	t=120 sec	t=240 sec	t=300 sec	t=600 sec	
0	684	489	327	232	169	120	75	
0.84	612.5	409	270	197	140	102	63	
1.68	514	323	217	153	111	75	46	
2.52	388	247	156	113	85	54	33	
3.36	277	180	113	85	62	39	22.3	
4.20	195	134	75	61	38	26	15.0	
5.04	131	98	50	45	25	17.5	8.1	
5.88	88	72	31	33	17.5	10.75	4.7	
6.72	60	51	20	20.5	10.5	6.1	2.9	
7.56	42	34	13	12	7.4	2.4	1.5	
8.4	31	22.6	9	7	4.6	1.57	1.0	
9.24	22.5	14	5.44	5.5	2.3	1.0	0.65	
10.08	15.5	10.85	3.50	3.73	1.7	0.8	*	

Table 6.13 - continued.

$\lambda$ ( $\mu$ )	$N_{L>}(\lambda)$ per cm							
	t=30 sec	t=45 sec	t=60 sec	t=120 sec	t=240 sec	t=300 sec	t=600 sec	
10.92	10.10	7.8	2.0	1.4	0.80	0.6	*	
11.76	6.2	6.0	1.77	0.18	0.16	*	*	
12.6	4.7	3.9	1.62	0.15	*	*	*	
13.44	3.55	2.92	1.38	0.15	*	*	*	
14.28	2.3	1.55	0.98	0.11	*	*	*	
15.12	1.25	1.36	0.65	0	*	*	*	
15.96	0.62	1.25	0.47	0	*	*	*	
16.80	0	0.15	0	0	*	*	*	

\*No measurements performed

\* No measurements performed

Table 6.14  
 Measured Values of  $N_{L>}(\lambda)$  Function for  
 Different Values of the Intercept Length,  $\lambda$   
 Austenitizing temperature: 760°C  
 Starting Structure: D<sub>2</sub>

$\lambda$ ( $\mu$ )	$N_{L>}(\lambda)$ per cm					
	t=30 sec	t=45 sec	t=60 sec	t=90 sec	t=150 sec	
0	413	336.5	223.5	165	96.5	
1.23	351.7	269.85	187.76	141.31	78.75	
2.46	242	195.91	124.54	95.12	56.24	
3.69	150	125.2	75	55.4	35.15	
4.92	89.8	75.8	41	32.2	21.28	
6.15	49.7	44.30	20.3	21.8	10.47	
7.38	29.5	22.4	9.96	15	5.37	
8.61	16.2	13.06	5.95	8.57	2.79	
9.84	9.32	6.32	3.10	4.4	1.49	
11.07	5.27	3.53	0.44	2.2	0.58	



volume fraction and surface area of the spherodized cementite were measured by using the Quantimet. The values of the volume fraction and surface area of the spherodized cementite measured by these two procedures are given in Table 6.15.

Table 6.15  
Starting Structure: D<sub>2</sub>

2% nital etch and manual measurements		Boiling sodium picrate etch and Quantimet measurements	
$V_V^c$	$S_V^c \text{ cm}^2/\text{cm}^3$	$V_V^c$	$S_V^c \text{ cm}^2/\text{cm}^3$
0.128	1456	0.13	1500

No significant difference is observed in the values of the volume fraction and surface area measured on the same sample, etched by two different etching procedures. Thus, one may conclude that the etching technique (Table 6.2) did not give rise to any artifacts.

It is not possible to reveal the ferrite grain boundaries by using the etching procedure described in Table 6.2. In order to etch both the spherodized cementite and the ferrite grain boundaries, the following etching procedure was used. The samples were first etched by using the procedure described in Table 6.2 and then re-etched by using the etching procedure described in Table 6.16.

Table 6.16  
Etching Procedure for Etching the Ferrite  
Grain Boundaries and Martensite

Solution A: 2 gm picric acid in 100 cc of  
methyl alcohol

Solution B: 2% nital

Immerse the sample in Solution A for 5 seconds and then immerse it in Solution B for 5 to 10 seconds.

A typical microstructure of the starting as-coarsened samples revealed in this manner is shown in Figure 6.2. In all three starting structures it was observed that most of the spherodized cementite was situated at the ferrite grain edges (see Figure 6.2). The volume fraction of the cementite particles was determined for the particles situated at the ferrite grain edges,  $V_V^e$ , grain boundaries,  $V_V^b$ , and inside the ferrite matrix,  $V_V^m$ , in the as-coarsened sample of batch  $D_3$ . The results are as follows:

$$V_V^e = 0.108$$

$$V_V^b = 0.03$$

$$V_V^m = 0.002$$

Thus, 80% of the spherodized cementite volume was situated at the ferrite grain edges. It may be concluded that the spherodized cementite is situated at the ferrite grain edges in these samples.

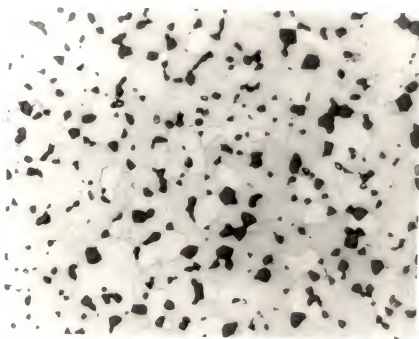


Figure 6.2. A photomicrograph of the starting structure  $D_3$  etched with the double etching procedure.

A detailed quantitative microstructural analysis was carried out on the as-coarsened structure of the batch D<sub>3</sub>. The results are given in Table 6.17.

Table 6.17  
Detailed Microstructural Analysis of  
Starting Structure D<sub>3</sub>

- 1) Volume fraction of cementite = 0.14
- 2) Surface area of cementite =  $1384 \text{ cm}^2/\text{cm}^3$
- 3) Total curvature of cementite =  $3.94 \times 10^6 \text{ cm}/\text{cm}^3$
- 4) Surface area of the ferrite grain boundaries =  $1744 \text{ cm}^2/\text{cm}^3$
- 5) Length of the ferrite grain edges =  $2.024 \times 10^6 \text{ cm}^2/\text{cm}^3$
- 6) Length of the ferrite grain edges occupied by cementite =  $2.26 \times 10^6 \text{ cm}/\text{cm}^3$
- 7) Fraction of the ferrite grain edge length occupied by cementite: 0.53
- 8) Length of ferrite-ferrite-cementite triple lines =  $4.171 \times 10^6 \text{ cm}/\text{cm}^3$

It is observed that although most of the cementite particles are on the ferrite grain edges, only 53% of the ferrite grain edge length is occupied by the spheroidized cementite. Some serial sectioning was done on the as-coarsened structure of the batch D<sub>3</sub>. It was observed that the cementite particles, which looked discrete and separate on the section, were interconnected in the third

dimension. No quantitative measurements were made to evaluate the connectivity of the structure.

A detailed quantitative microstructural analysis was performed on each sample of one series (starting structure  $D_3$ ) partially austenitized at  $750^\circ\text{C}$ . There are three phases present in the partially austenitized samples: ferrite, cementite and austenite (which is martensite in the quenched samples). Let superscript  $\alpha$  denote the ferrite phase,  $\gamma$  denote the austenite and  $C$  denote the cementite. The following geometrical properties were measured in each  $D_3$  sample reacted at  $750^\circ\text{C}$ .

- 1) Volume fraction of austenite  $V_V^\gamma$
- 2) Volume fraction of cementite  $V_V^C$
- 3) Total surface area of austenite  $S_V^\gamma$
- 4) Total surface area of cementite  $S_V^C$
- 5) Total curvature of cementite  $M_V^C$
- 6) Surface area of austenite-cementite interface  $S_V^{\gamma-C}$
- 7) Surface area of ferrite-cementite interface  $S_V^{\gamma-\alpha}$
- 8) Surface area of ferrite grain boundaries  $S_V^{\alpha\alpha}$
- 9) Length of the ferrite grain edges  $L_V^{\alpha\alpha\alpha}$
- 10) Length of ferrite-ferrite-austenite triple lines  $L_V^{\alpha\alpha\gamma}$
- 11) Length of ferrite-ferrite-carbide triple lines  $L_V^{\alpha\alpha C}$
- 12) Length of ferrite-austenite-carbide triple lines  $L_V^{\alpha\gamma C}$

To the best knowledge of the author such an exhaustive quantitative microscopic study of a phase transformation has never been done before. It will be shown in the subsequent sections that these measurements are essential for the rigorous understanding of this apparently simple process.

In order to etch all the three phases and the ferrite grain boundaries present in the partially austenitized samples, the samples were first etched by using the etching procedure described in Table 6.2 and then re-etched by using the procedure described in Table 6.16. The typical microstructures of the partially austenitized samples are shown in Figures 6.3 to 6.5. The detailed quantitative microstructural analysis of the  $D_3$  samples reacted at  $750^{\circ}\text{C}$  was performed manually. The measurements were carried out by projecting the image on the T.V. screen of the Quantimet. A grid was superimposed on the image to perform the measurements. The results are given in Tables 6.18 to 6.20. The following qualitative observations were made on the partially austenitized samples.

(1) The spherodized cementite was not completely covered with austenite til the austenite volume fraction was approximately 0.5.

(2) The growth of austenite was inhibited across the ferrite grain boundaries.

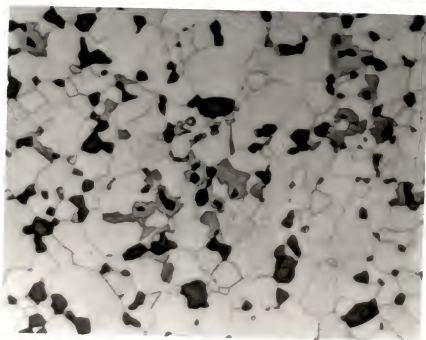


Figure 6.3. Microstructure of a sample partially austenitized at 750°C for 35 sec (starting structure D<sub>3</sub>).

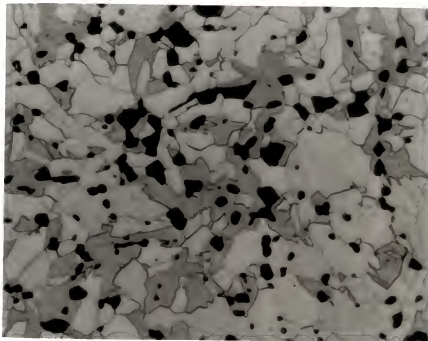


Figure 6.4. Microstructure of a sample partially austenitized at 750°C for 50 sec (starting structure D<sub>3</sub>).



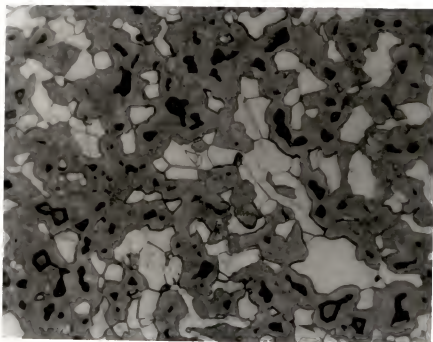


Figure 6.5. Microstructure of a sample partially austenitized at 750°C for 90 sec (starting structure D3).

Table 6.18  
 A Detailed Stereological Analysis of the  
 Interfacial Areas  
 Austenitizing temperature: 750°C  
 Starting structure: D<sub>3</sub>  
 Units for surface areas: cm<sup>2</sup>/cm<sup>3</sup>

Austenitizing time (sec)	S <sub>V</sub> <sup>γ</sup> total	S <sub>V</sub> <sup>C</sup> total	S <sub>V</sub> <sup>γ-C</sup>	S <sub>V</sub> <sup>γ-α</sup>	S <sub>V</sub> <sup>α-C</sup>	S <sub>V</sub> <sup>αα</sup>
0	0	1384	0	0	1384	1744
30	968	1162	344	624	816	1105
35	1042	1016	300	742	716	911
40	1317	995	400	917	596	744
45	920	980	*	*	*	779
50	1789	850	491	1298	359	668
65	1950	681	550	1400	131	320
90	1763	630	606	1157	0	258
150	1051	400	400	651	0	108

\* No measurements performed

Table 6.19  
 A Detailed Stereological Analysis of the  
 Lineal Features  
 Austenitizing temperature: 750°C  
 Starting Structure: D<sub>3</sub>

Units: cm/cm<sup>3</sup>

Austenitizing time (sec)	$L_V^{\alpha\alpha\alpha}$	$L_V^{\alpha\alpha\gamma}$	$L_V^{\alpha\alpha C}$	$L_V^{\alpha\gamma C}$
0	$2.024 \times 10^6$	0	$4.171 \times 10^6$	0
30	$1.05 \times 10^6$	$9.58 \times 10^5$	$1.851 \times 10^6$	$7.42 \times 10^5$
35	$0.91 \times 10^6$	$8.7 \times 10^5$	$1.085 \times 10^6$	$4.81 \times 10^5$
40	$0.694 \times 10^6$	$9.0 \times 10^5$	$0.85 \times 10^6$	$6.05 \times 10^5$
45	$0.72 \times 10^6$	*	*	$4.67 \times 10^5$
50	$0.688 \times 10^6$	$1.14 \times 10^6$	$0.8 \times 10^6$	$9.05 \times 10^5$
65	$0.237 \times 10^6$	$1.0 \times 10^6$	*	*
90	$0.188 \times 10^6$	$9.32 \times 10^5$	0	0
150	$0.086 \times 10^6$	$4.15 \times 10^5$	0	0

\* No measurements made

Table 6.20  
 Measured Volume Fractions of Different Phases  
 Austenitizing temperature: 750°C  
 Starting Structure: D<sub>3</sub>

Austenitizing time (sec)	$V_V^C$	$V_V^Y$	$V_V^\alpha$
0	0.14	0	0.86
30	0.11	0.116	0.77
35	0.12	0.130	0.75
40	0.113	0.184	0.70
45	0.10	0.160	0.74
50	0.0847	0.285	0.63
65	0.0612	0.45	0.49
90	0.0548	0.58	0.37
150	0.037	0.83	0.13

(3) Austenite nucleated preferentially along the ferrite grain edges.

(4) The austenite growth along the ferrite grain boundaries was much more than that inside the ferrite grains.

(5) There is some incubation time involved in the formation of austenite; the magnitude of this incubation time depends on the austenitizing temperature. Furthermore, the magnitude of the incubation time is higher for the coarser starting structures. Some  $D_2$  samples were reacted at  $730^\circ\text{C}$ . It was observed that the austenite was not formed in these samples for reaction times less than 75 seconds. Thus, it can be concluded that the observation of incubation time is not an artifact arising from the experimental procedures.

#### 6.4 Data Processing:

(1) It was observed that the volume fraction,  $V_V^C$ , of cementite varied linearly with the surface area,  $S_V^C$ , of cementite. This behavior is shown in Figures 6.6 to 6.10 for different austenitizing temperatures and starting structures. Table 6.21 gives the values of slope and intercept of the plot of  $S_V^C$  vs.  $V_V^C$  for different austenitizing temperatures and starting structures. It is

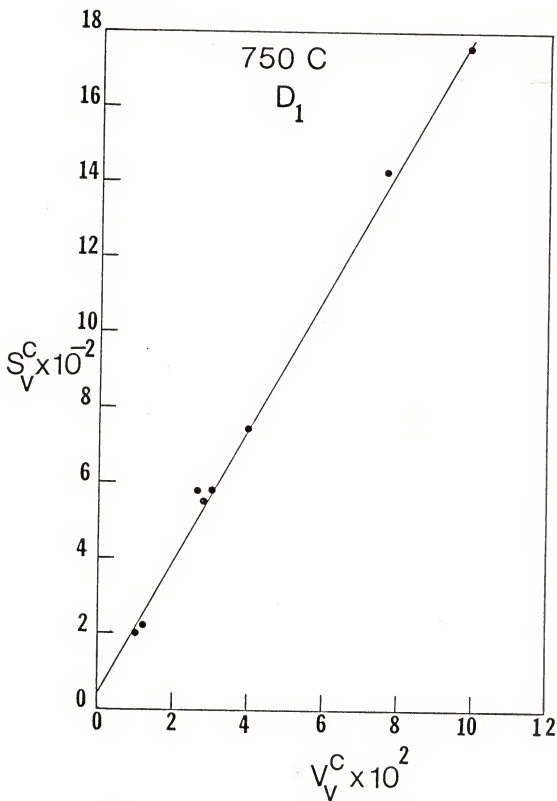


Figure 6.6. A plot of the surface area,  $S_V^C$ , of cementite vs. its volume fraction,  $V_V^C$ , during the austenitization of the starting structure,  $D_1$ , at 750°C.

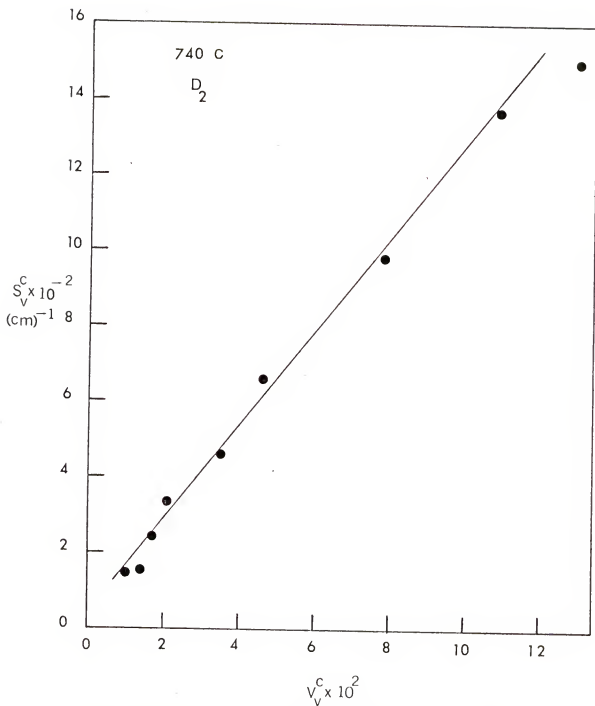


Figure 6.7. A plot of the surface area,  $S_V^C$ , of cementite vs. its volume fraction,  $V_V^C$ , during the austenitization of the starting structure, D<sub>2</sub>, at 740°C.

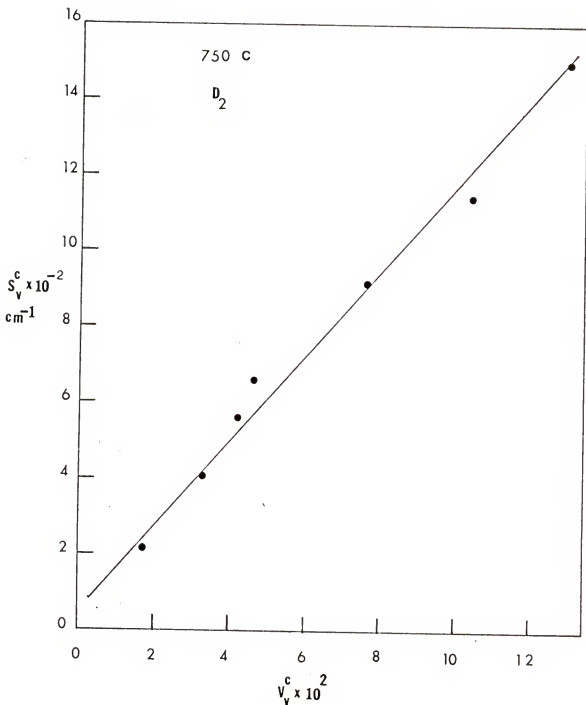


Figure 6.8. A plot of the surface area,  $S_V^C$ , of cementite vs. its volume fraction,  $V_V^C$ , during the austenitization of the starting structure, D<sub>2</sub>, at 750°C.



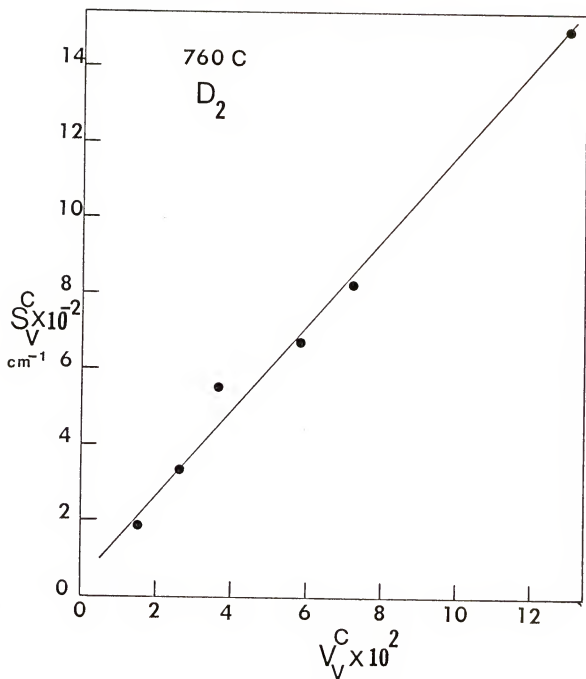


Figure 6.9. A plot of the surface area,  $S_V^C$ , of cementite vs. its volume fraction,  $V_V^C$ , during the austenitization of the starting structure, D<sub>2</sub>, at 760°C.

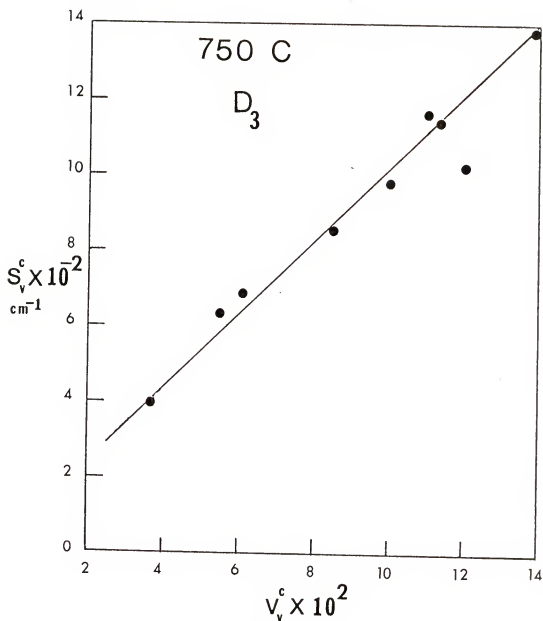


Figure 6.10. A plot of the surface area,  $S_v^c$ , of cementite vs. its volume fraction,  $V_v^c$ , during the austenitization of the starting structure, D<sub>3</sub>, at 750°C.

Table 6.21  
 $S_V^C = A_1 V_V^C + A_2$

Austenitizing temperature	Starting structure	Slope $A_1$ $\text{cm}^2/\text{cm}^3$	Intercept $A_2$ $\text{cm}^2/\text{cm}^3$
750°C	$D_1$	$1.7 \times 10^4$	70
750°C	$D_2$	$1.12 \times 10^4$	40
750°C	$D_3$	$0.95 \times 10^4$	60
740°C	$D_2$	$1.21 \times 10^4$	40
760°C	$D_2$	$1.12 \times 10^4$	40

interesting to note that the slope and the intercept do not vary significantly with the austenitizing temperature but depend on the starting structure. This may indicate that the linear relationship between  $S_V^C$  and  $V_V^C$  results from the geometry of the starting microstructure rather than the kinetics of the process. Figure 6.11 shows a plot of  $(S_V^C/S_{V_0}^C)$  vs.  $(V_V^C/V_{V_0}^C)$  for all the austenitizing times, temperatures and the starting structures of spherodized cementite ( $V_{V_0}^V$  and  $S_{V_0}^C$ ) are the volume fraction and surface area of spherodized cementite in the unreacted samples. All the data points fall on one straight line. Thus we have the following empirical relationship between the volume fraction and surface area of cementite during the austenitization of these spherodized structures:

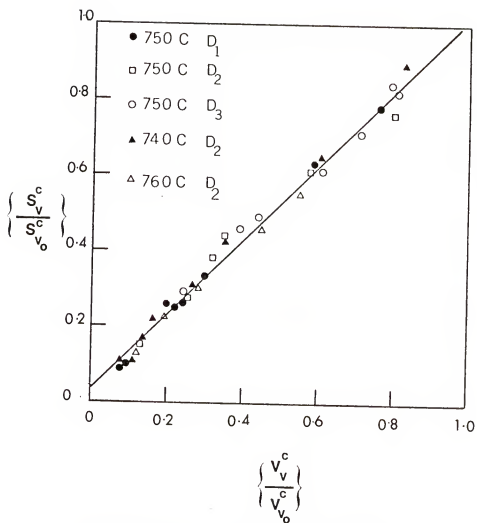


Figure 6.11. A plot of  $\left( \frac{S_v^c}{S_{v_0}^c} \right)$  vs.  $\left( \frac{V_v^c}{V_{v_0}^c} \right)$  during the austenitization of the spheroidized cementite structures.

$$\frac{s_V^C}{s_{V_0}^C} = 1.01 \left( \frac{v_V^C}{v_{V_0}^C} \right) + 0.03 \quad (6.6)$$

Equation (6.6) is valid for all the austenitizing temperatures and starting structures of spherodized cementite. The mean linear intercept,  $\bar{\lambda}^C$ , of the cementite phase is given by the following equation:

$$\bar{\lambda}^C = \frac{4v_V^C}{s_V^C} \quad (6.7)$$

Combining equations (6.6) and (6.7) gives

$$\bar{\lambda}^C = \frac{\bar{\lambda}_0^C}{\frac{v_V^C}{v_{V_0}^C} [1.01 + 0.03 \frac{v_{V_0}^C}{v_V^C}]} \quad (6.8)$$

where  $\bar{\lambda}_0^C$  is the mean intercept of spherodized cementite in the starting structure. It is interesting to note that, for  $v_V^C > 0.03$ ,

$$\bar{\lambda}^C \approx \bar{\lambda}_0^C \quad (6.9)$$

Thus mean intercept of the spherodized cementite does not vary significantly with the austenitization time til the process is almost complete. This is a rather peculiar result, because one would expect the mean intercept,  $\bar{\lambda}^C$ , to decrease systematically with time as the spherodized cementite dissolves.

It was observed that the total curvature,  $M_V^C$ , of the spherodized cementite varied linearly with its surface area,  $S_V^C$ , during the austenitization process. This behavior is shown in Figures 6.12 to 6.16, for different austenitizing temperatures and starting structures of spherodized cementite. Table 6.22 gives the values of the slope and intercept of the plot of  $M_V^C$  vs.  $S_V^C$  for different austenitizing temperatures and starting structures.

Table 6.22  
 $M_V^C = A_3 S_V^C + A_4$

Austenitizing temperature	Starting structure	Slope $A_3$ 1/cm	Intercept $A_4$ cm/cm <sup>3</sup>
750 C	D <sub>1</sub>	4900	$4.0 \times 10^5$
750 C	D <sub>2</sub>	3000	$0.50 \times 10^5$
750 C	D <sub>3</sub>	2790	$0.50 \times 10^5$
740 C	D <sub>2</sub>	3180	$-2.0 \times 10^5$
760 C	D <sub>2</sub>	3000	$0.5 \times 10^5$

Figure 6.17 shows a plot of  $(M_V^C/M_{V0}^C)$  vs.  $(S_V^C/S_{V0}^C)$  for all the austenitizing times, temperatures and the starting structures of the spherodized cementite ( $M_{V0}^C$  and  $S_{V0}^C$  are the total curvature and surface area of the cementite

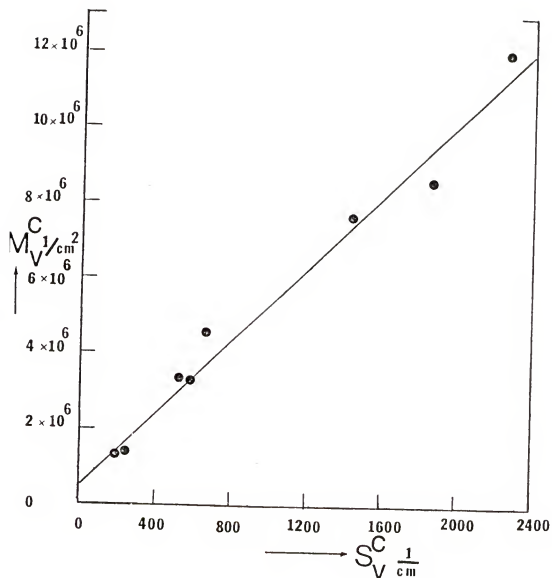


Figure 6.12. A graph of  $M_V^C$  vs.  $S_V^C$  during the austenitization of the starting structure, D<sub>1</sub>, at 750°C.

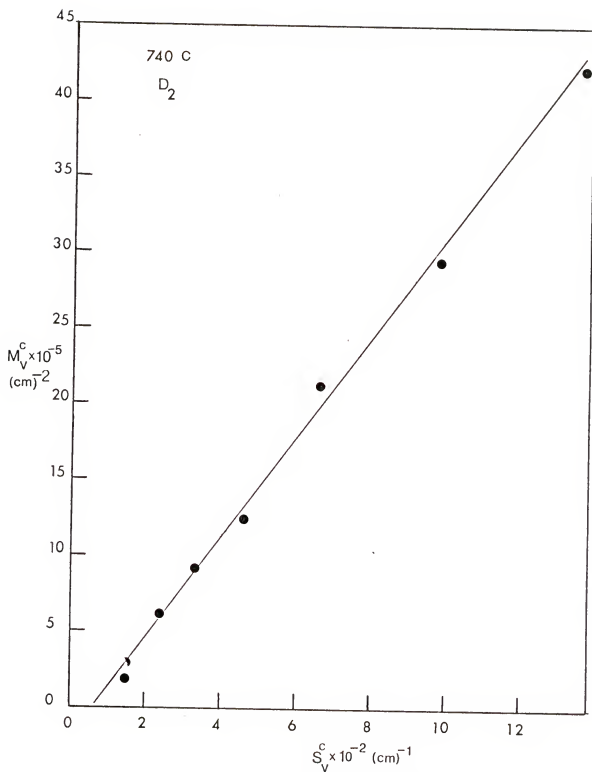


Figure 6.13. A graph of  $M_V^C$  vs.  $S_V^C$  during the austenitization of the starting structure D<sub>2</sub> at 740°C.



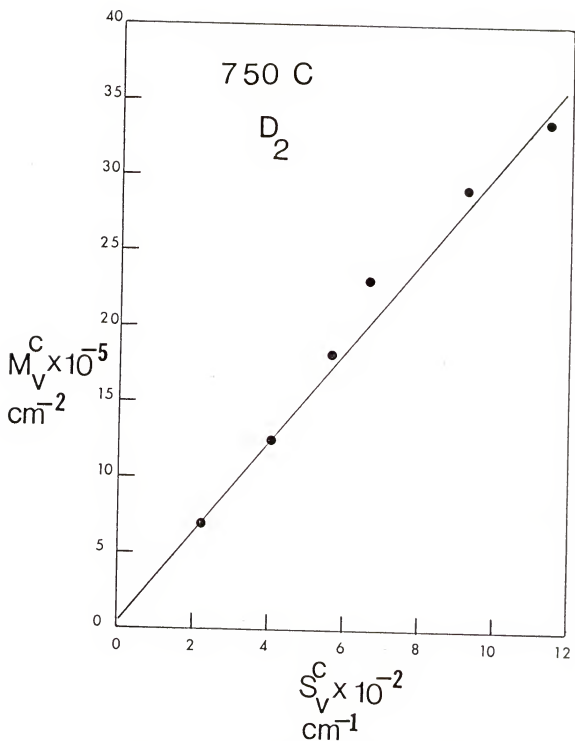


Figure 6.14. A graph of  $M_V^C$  vs.  $S_V^C$  during the austenitization of the starting structure D<sub>2</sub> at 750°C.

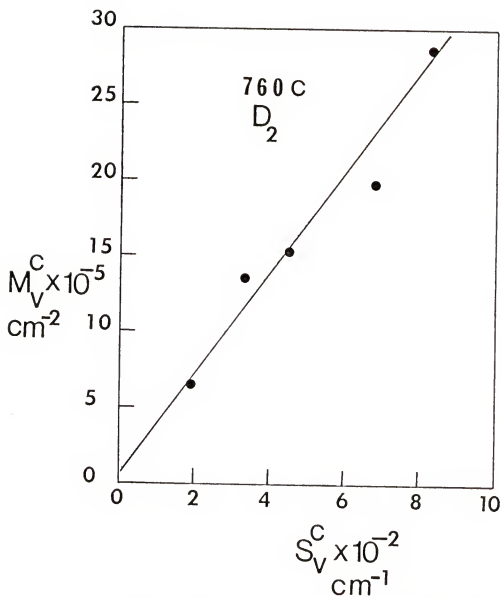


Figure 6.15. A graph of  $M_V^C$  vs.  $S_V^C$  during the austenitization of the starting structure D<sub>2</sub> at 760°C.

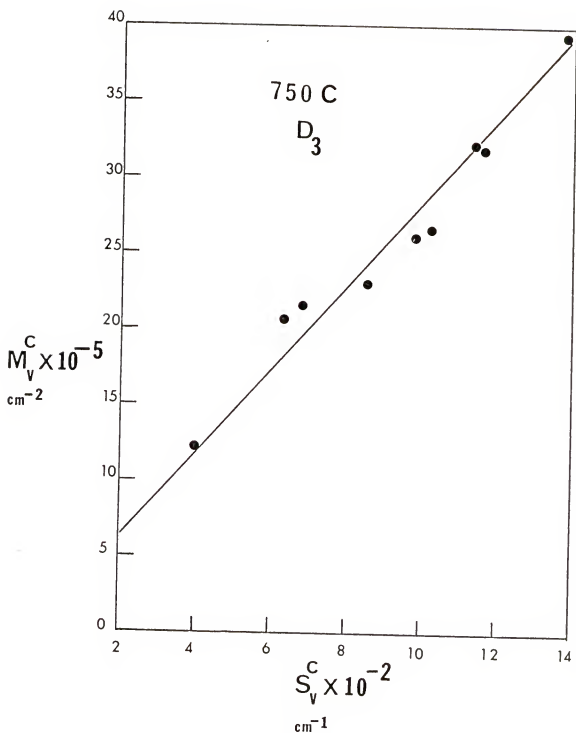


Figure 6.16. A graph of  $M_v^C$  vs.  $S_v^C$  during the austenitization of the starting structure D<sub>3</sub> at 750°C.

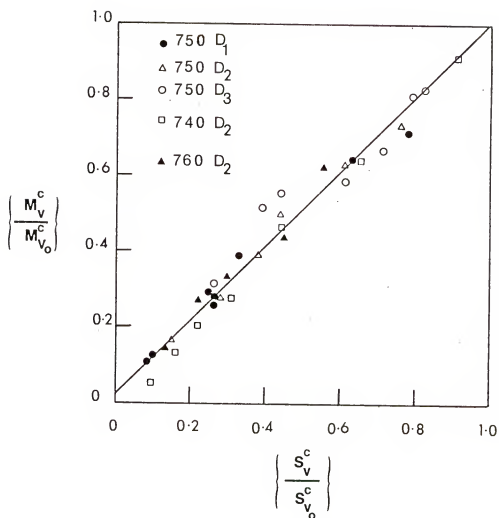


Figure 6.17. A graph of  $(M_v^c/M_{v_0}^c)$  vs.  $(S_v^c/S_{v_0}^c)$  during the austenitization of the spheroidized cementite structures.

phase in the starting structures). The plot is linear and all the data points fall on one straight line. Thus we have the following empirical relationship between the total curvature and surface area of the spherodized cementite during the process:

$$\frac{M_V^C}{M_{V0}^C} = 0.98 \left[ \frac{S_V^C}{S_{V0}^C} \right] + 0.02 \quad (6.10)$$

The mean curvature,  $\bar{H}^C$ , of the spherodized cementite is given by the following equation [34,35]:

$$\bar{H}^C = \frac{M_V^C}{S_V^C} \quad (6.11)$$

Combining equations (6.10) and (6.11) yields

$$\bar{H}^C = \bar{H}_0^C \left[ 0.98 + 0.02 \frac{S_{V0}^C}{S_V^C} \right] \quad (6.12)$$

where  $\bar{H}_0^C$  is the mean curvature of the spherodized cementite in the starting structure. Thus the mean curvature of the spherodized cementite does not vary significantly with the austenitizing time til the process is almost complete. Again, this is a very peculiar result because one would expect  $\bar{H}^C$  to increase systematically with the austenitizing time.

Define an inverse cumulative frequency function,

$F_{>}(\ell, t)$  for the linear intercepts of spheroidized cementite at time  $t$  as

$$F_{>}(\ell, t) = \frac{N_{L>}(\ell, t)}{N_L(t)} \quad (6.13)$$

where  $N_L(t)$  is the total number of intercepts. Note that

$$N_L(t) = \frac{S_V^C(t)}{2} \quad (6.14)$$

Figures 6.18 to 6.22 show the plots of  $F_{>}(\ell, t)$  vs.  $(\ell/\bar{\lambda}^C)$  at different austenitizing times for given austenitizing temperatures and starting structures. It is observed that for a given austenitizing temperature and starting structure, the plot of  $F_{>}(\ell, t)$  vs.  $(\ell/\bar{\lambda}^C)$  is independent of the austenitizing time. In each of the figures (6.18 to 6.22), it is observed that the data points, at different austenitizing times, fall on the same curve. Thus,

$$F_{>}(\ell, t) = \left\{ \begin{array}{l} \text{a function of} \\ (\ell/\bar{\lambda}^C) \text{ only} \end{array} \right\} = \phi(\ell/\bar{\lambda}^C) \quad (6.15)$$

This is a very peculiar observation, because if it is due to the kinetics of the process, then it suggests an asymptotic distribution of the cementite particles during the austenitizing process, which is not at all expected. On the other hand this observation can be explained in a

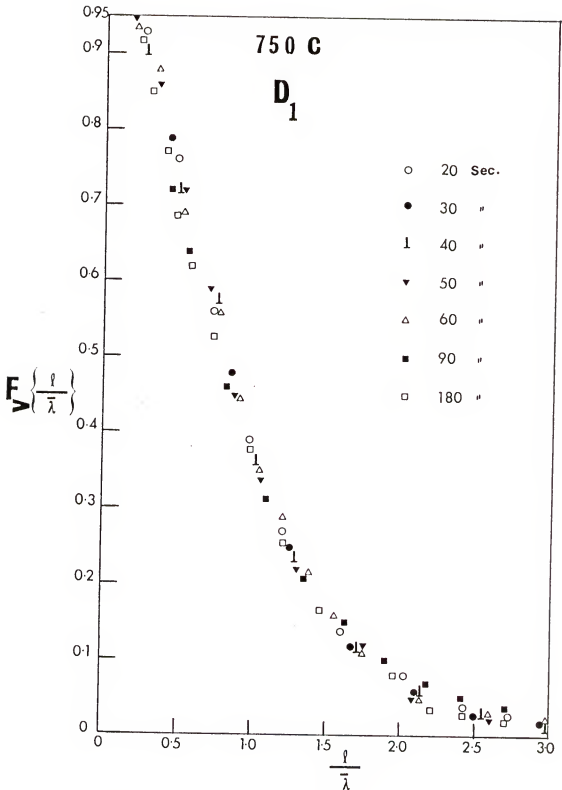


Figure 6.18. A graph of inverse cumulative frequency function,  $F_{\geq}(l)$ , vs.  $l/\bar{\lambda}$ , at various times during the austenitization of the starting structure D<sub>1</sub> at 750°C.

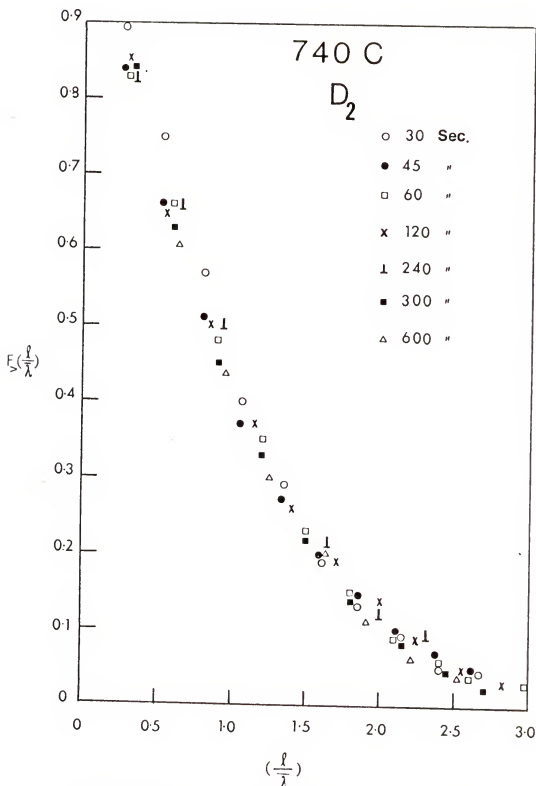


Figure 6.19. A graph of inverse cumulative frequency function,  $F_{>}(\ell)$ , vs.  $\ell/\lambda$ , at various times during the austenitization of the starting structure  $D_2$  at 740°C.



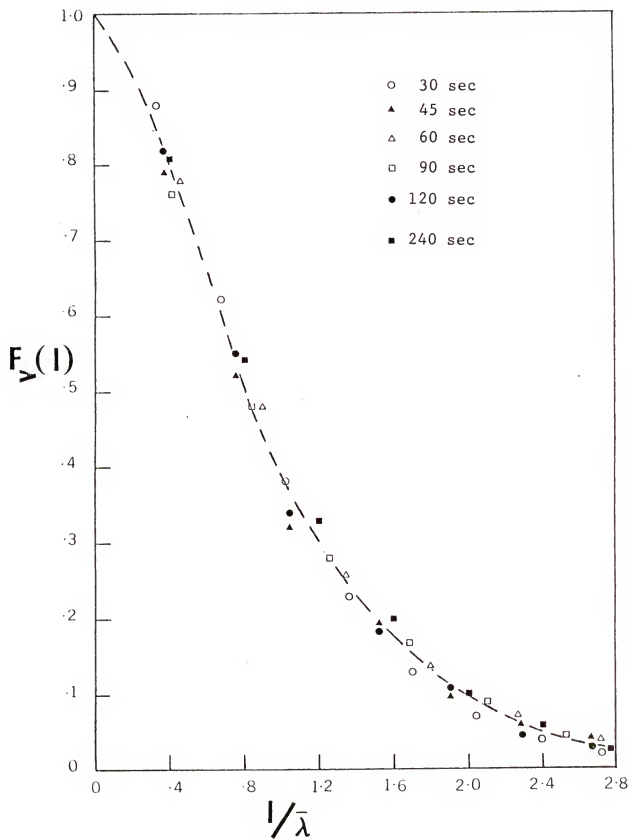


Figure 6.20. A graph of inverse cumulative frequency function,  $F_{\geq}(\ell)$ , vs.  $\ell/\bar{\lambda}$ , at various times during the austenitization of the starting structure D<sub>2</sub> at 750°C.

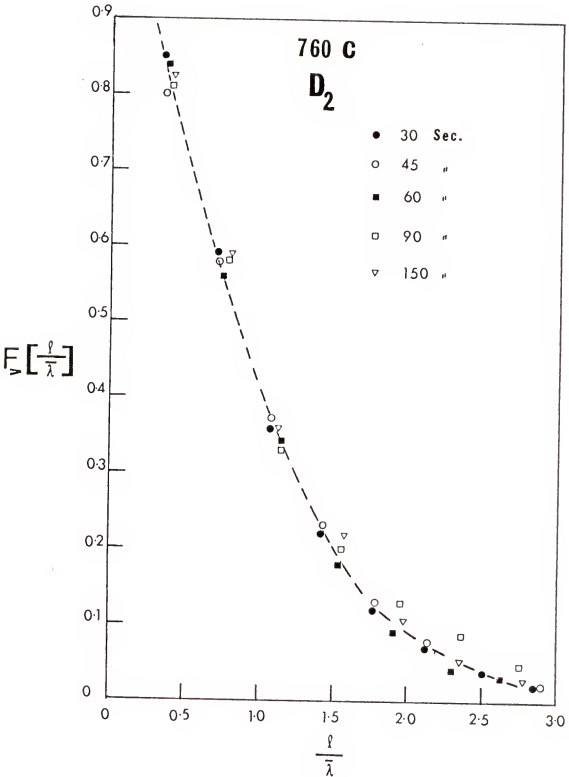


Figure 6.21. A graph of inverse cumulative frequency function,  $F_{>}(\ell)$ , vs.  $\ell/\bar{\lambda}$ , at various times during the austenitization of the starting structure D<sub>2</sub> at 760°C.

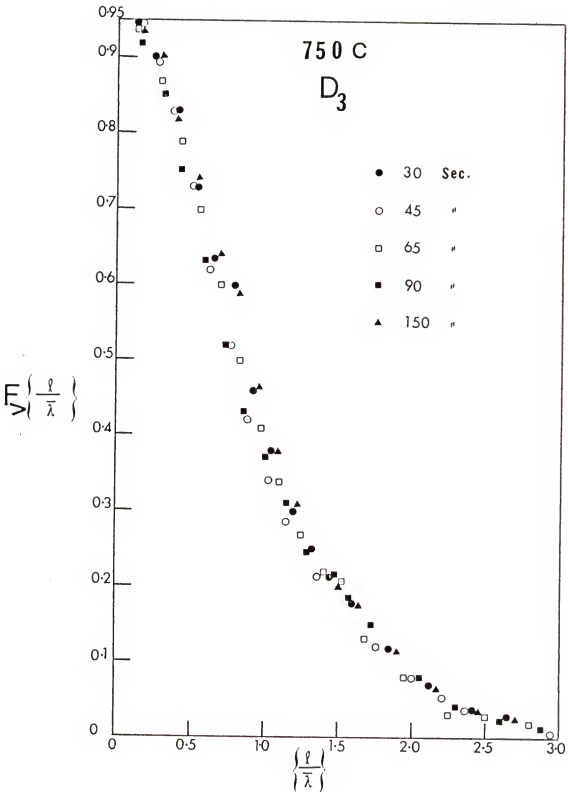


Figure 6.22. A graph of inverse cumulative frequency function,  $F_{\geq}(\ell)$ , vs.  $\ell/\bar{\lambda}$ , at various times during the austenitization of the starting structure  $D_3$  at  $750^\circ\text{C}$ .

very simple manner in terms of the geometry of the starting structure.

#### 6.4.1 Data Processing of the Detailed Quantitative Microscopic Measurements Made on the D<sub>3</sub> Samples Austenitized at 750°C

- (1) Time variation of the volume fraction of austenite:

A plot of  $\log\{V_V^Y/(1-V_V^Y)\}$  vs.  $\log t$  is shown in Figure 6.23. The plot linear and the straight line has a slope of 2.25. Thus the following equation describes the time variation of the volume fraction of austenite:

$$\frac{V_V^Y}{1-V_V^Y} = B_1^Y t^{2.25} \quad (6.16)$$

where  $B_1^Y = 5.75 \times 10^{-5}$  per (sec)<sup>2.25</sup> at 750°C. Note that  $B_1^Y$  is expected to change with the austenitizing temperature. The conventional plot of  $\log\{\ln(1/(1-V_V^Y))\}$  vs.  $\log t$  was found to be non-linear which may be due to the non-random impingement. This is not surprising, because austenite is not randomly distributed in the matrix and it grows preferentially along the ferrite grain boundaries.

- (2) Relationship between the volume fraction and surface area of austenite:

A plot of  $\{S_V^Y/(1-V_V^Y)\}$  vs.  $V_V^Y$  is shown in Figure 6.24.

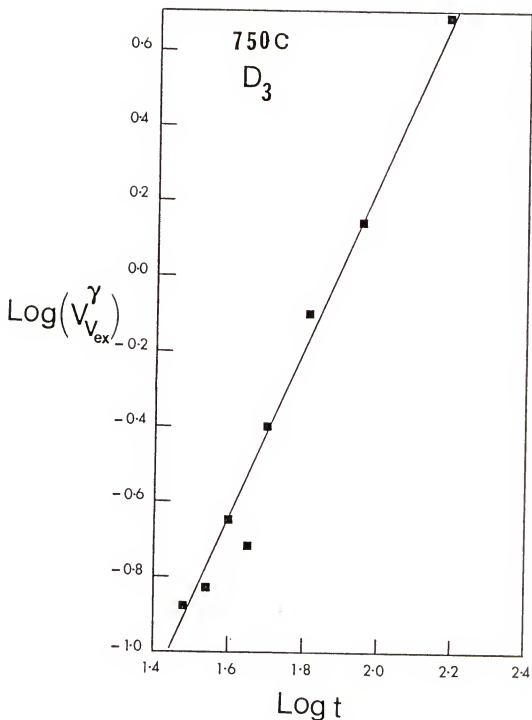


Figure 6.23. A graph of  $\text{Log}(V_{\text{ex}}^{\gamma}/1-V_{\text{ex}}^{\gamma})$  vs.  $\text{Log } t$  during the austenitization of the starting structure D<sub>3</sub> at 750°C.

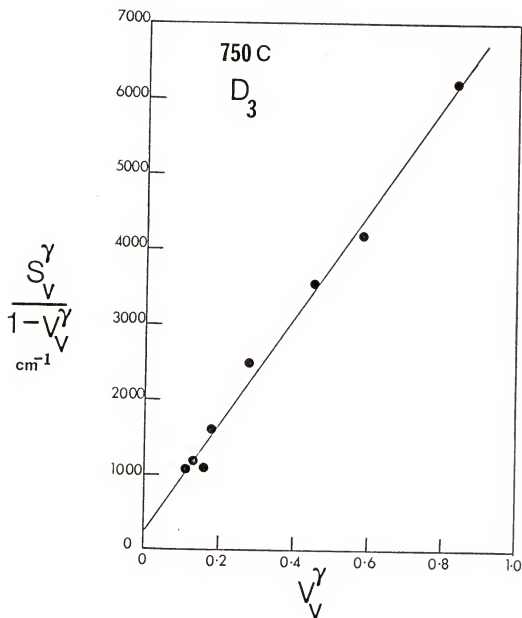


Figure 6.24. A graph of  $(S_V^\gamma/1-V_V^\gamma)$  vs.  $V_V^\gamma$  during the austenitization of the starting structure D<sub>3</sub> at 750°C.

The behavior is linear. The following equation describes the relationship between the volume fraction of austenite and its surface area during the process.

$$\frac{S_V^Y}{(1-V_V^Y)} = B_2 V_V^Y + B_3 \quad (6.17)$$

where  $B_2 = 7100$  per-cm and  $B_3 = 250$  per-cm. Combining equations (6.16) and (6.17), together with the definition of the surface area averaged interface velocity of austenite,  $\bar{v}_S^Y$ , gives the following result:

$$\bar{v}_S^Y \approx \frac{3.16 \times 10^{-4}}{t} \text{ cm/sec} \quad (6.18)$$

### 6.5 Data Analysis:

It was observed that 80% of the spherodized cementite volume was situated at the ferrite grain edges.

This spherodized cementite can be in the form of

- (1) complete grain edge network,
- (2) discrete particles situated at the ferrite grain edges

or

- (3) incomplete grain edge network.

Only 53% of the ferrite grain edge length was occupied by the spherodized cementite, so the spherodized cementite can not be in the form of a complete grain edge network.



Thus, the first case (i.e. the possibility of complete grain edge network) can be rejected. Let us consider the second possibility. If the spherodized cementite is in the form of discrete particles of the same shape, then the three dimensional particle size distribution can be evaluated as follows.

Combining equations (6.13), (6.14) and (6.15) gives

$$N_{L>}(\ell, t) = \frac{S_V^C(t)}{2} \phi[\ell/\bar{\lambda}^C] \quad (6.19)$$

By definition

$$n_L(\ell, t) = -\frac{dN_{L>}(\ell, t)}{d\ell}$$

Thus,

$$n_L(\ell, t) = \frac{S_V^C(t)}{\bar{\lambda}^C(t)} \cdot \left\{ -\frac{1}{2} \frac{d\{\phi(\ell/\bar{\lambda}^C)\}}{d\{\ell/\bar{\lambda}^C\}} \right\} \quad (6.20)$$

Combining equations (6.20) and (2.10) yields

$$n_V(\ell, t) = \frac{S_V^C(t)}{\{\bar{\lambda}^C(t)\}^3} \cdot \frac{-1}{2K} \frac{d}{d(\ell/\bar{\lambda}^C)} \left[ \frac{\bar{\lambda}^C}{\ell} \cdot \frac{d\phi(\ell/\bar{\lambda}^C)}{d(\ell/\bar{\lambda}^C)} \right] \quad (6.21)$$

where  $n_V(\ell, t)$  is the P.S.D. function and  $K$  is a shape factor. The second factor on the right-hand side of this equation is a function of  $(\ell/\bar{\lambda}^C)$  only. Let

$$\theta[\ell/\bar{\lambda}^C] = \frac{-1}{2K} \frac{d}{d(\ell/\bar{\lambda}^C)} \left\{ \frac{\bar{\lambda}^C}{\ell} \cdot \frac{d\phi(\ell/\bar{\lambda}^C)}{d(\ell/\bar{\lambda}^C)} \right\} \quad (6.22)$$

Then,

$$n_V(\ell, t) = \frac{S_V^C(t)}{\{\bar{\lambda}^C(t)\}^3} \cdot \theta(\ell/\bar{\lambda}^C) \quad (6.23)$$

Let us define

$$\theta_>(\ell/\bar{\lambda}^C) = \int_{\ell/\bar{\lambda}^C}^{\infty} \theta(\ell/\bar{\lambda}^C) \cdot d(\ell/\bar{\lambda}^C) \quad (6.24)$$

Integration of equation (6.23) gives the following expression for the total number of cementite particles per unit volume,  $N_V^C(t)$ :

$$N_V^C(t) = \frac{\theta_>(0) \cdot S_V^C(t)}{\{\bar{\lambda}^C(t)\}^2} \quad (6.25)$$

where  $\theta_>(0) = \int_0^{\infty} \theta(\ell/\bar{\lambda}^C) \cdot d(\ell/\bar{\lambda}^C)$ . Combining equations (6.25), (6.8) and (6.6) yields

$$N_V^C(t) = \frac{\theta_>(0) S_{V_0}^C \left[ \frac{V_{V_0}^C}{V_V^C} \right]^2 [1.01 \left( \frac{V_V^C}{V_{V_0}^C} \right) + 0.03]^3}{(\bar{\lambda}_0^C)^2} \quad (6.26)$$

During most of the transformation  $V_V^C/V_{V_0}^C \gg 0.03$ . Thus one can approximate

$$N_V^C(t) \approx \frac{4\theta_>(0) V_V^C(t)}{\{\bar{\lambda}_0^C\}^3} \quad (6.27)$$

For a given starting structure,  $\bar{\lambda}_0^C$  is constant because it is the initial value of the mean intercept. Thus equation (6.27) predicts that the total number of cementite

particles per unit volume is directly proportional to its volume fraction during the austenitization process. Equations (6.6), (6.10) and (6.27) give the following result.

$$\begin{aligned}
 N_V^C(t) &= \frac{4\theta_>(0)}{\{\bar{\lambda}_0^C\}^2} V_V^C(t) = \left\{ \frac{4\theta_>(0)}{\{\bar{\lambda}_0^C\}^2} \right\} \left\{ \left( \frac{V_{V0}^C}{S_{V0}^C} \right) S_V^C(t) - 0.35 S_{V0}^C \right\} \\
 &= \left\{ \frac{4\theta_>(0)}{\{\bar{\lambda}_0^C\}^3} \right\} \left\{ \left( \frac{V_{V0}^C}{S_{V0}^C} \right) \left( \frac{S_{V0}^C}{M_{V0}^C} \right) M_V^C(t) - .05 S_{V0}^C \right\} \quad (6.28)
 \end{aligned}$$

Since  $\bar{\lambda}_0^C$ ,  $\theta_>(0)$ ,  $S_{V0}^C$ ,  $V_{V0}^C$  and  $M_{V0}^C$  are constants for a given starting structure, equation (6.28) predicts linear relationships between  $N_V^C(t)$ ,  $V_V^C(t)$ ,  $S_V^C(t)$  and  $M_V^C(t)$ . For a system of discrete particles, this would imply the following.

The growth rate of austenite is extremely large, so that as soon as the austenite grain nucleates on a given cementite particle, the cementite particle dissolves completely in a very short time. Thus the process of cementite dissolution simply consists of removing the cementite particles from the system at a finite rate. If this is so, then  $S_V^{Y-C}$  should be a very small fraction of the total cementite surface area at any given time. This contradicts with the experimental observation (see

Table 6.18) that for  $V_V^Y > 0.28$ ,  $S_V^{Y-C}/S_V^C > 0.5$ . Thus the assumption that the spherodized cementite is in the form of discrete particles of the same shape (at any given time) leads to a contradiction.

If it is assumed that the spherodized cementite is in a form of discrete particles but all the particles do not have the same shape at any given time, then it is not possible to evaluate the three dimensional particle size distribution from the distribution of intercepts and equation (6.27) is not valid. However, linear relationships between  $V_V^C$ ,  $S_V^C$  and  $M_V^C$  are an experimental observation and this behavior cannot be explained if the particles dissolve by a three dimensional dissolution geometry. It may be possible to explain a part of the experimental behavior, if it is further assumed that the cementite particles have a long, thin shape and they dissolve in a one dimensional fashion. However, this assumption is not much different from the assumption that cementite is in the form of an incomplete grain edge network. Furthermore, if it is assumed that "spherodized" cementite is in the form of an incomplete grain edge network, then it is possible to explain all the experimental observations in a simple manner. Thus it is reasonable to postulate that the "spherodized" cementite is present in the form of an incomplete grain edge network.

Since the network is along the ferrite grain edges, the initial length of ferrite-ferrite-cementite triple lines,  $L_{V_0}^{\alpha\alpha C}$ , should be equal to three times the length of the network,  $L_{V_0}^C$ . Thus,

$$L_{V_0}^{\alpha\alpha C} = 3L_{V_0}^C \quad (6.29)$$

The initial total curvature of such a network is given by [122]

$$M_{V_0}^C = \pi L_{V_0}^C \quad (6.30)$$

Combining equations (6.29) and (6.30) gives

$$M_{V_0}^C \approx L_{V_0}^{\alpha\alpha C} \quad (6.31)$$

For the initial structure of batch  $D_3$  (see Table 6.16)

$$M_{V_0}^C = 3.94 \times 10^6 \text{ cm/cm}^3$$

and

$$L_{V_0}^{\alpha\alpha C} = 4.17 \times 10^6 \text{ cm/cm}^3$$

Thus equation (6.31) is satisfied.

The geometrical description of cementite as an incomplete grain edge network explains observations made on the starting structures. These observations are as follows.

- (1) Almost all the cementite particles are observed

on the ferrite grain edges, and quantitatively 30% of the cementite volume is situated along the ferrite grain edges.

(2) Although the cementite is situated on the ferrite grain edges, only 53% of the ferrite grain edge length is occupied by cementite.

(3) Cementite particles which appear discrete on a section are interconnected in the third dimension (qualitative serial sectioning evidence).

$$(4) \quad M_{V_0}^C \approx L_{V_0}^C$$

This geometrical description will now be used to explain the observations made on the cementite phase during the austenitization process.

Since the cementite is assumed to be in the form of an incomplete network, its maximum dimension along a cross-section may be assumed to be much less than the length of each separate part. (Note that this is not an independent assumption.) It will be further assumed that the cementite network dissolves in a one dimensional manner, such that its length decreases with time while the cross-sectional area remains essentially constant. Let  $L_V(t)$  be the length of the network at time  $t$ . The volume fraction of cementite,  $V_V^C(t)$ , is given by

$$V_V^C(t) = \{\text{Average cross-sectional area}\} \cdot L_V(t) \quad (6.32)$$

During most of the transformation, the surface area,  $S_V^C(t)$ , is given by

$$S_V^C(t) = \{\text{Average cross-sectional perimeter}\} L_V(t) \quad (6.33)$$

During a one dimensional dissolution, the average cross-sectional area and the average cross-sectional perimeter does not change with time. Thus,

$$\frac{V_{V0}^C}{S_{V0}^C} = \frac{(\text{Average cross-sectional area})}{(\text{Average cross-sectional perimeter})} \quad (6.34)$$

Combining equations (6.32) to (6.34) yields

$$\frac{S_V^C(t)}{S_{V0}^C} = \frac{V_V^C(t)}{V_{V0}^C} \quad (6.35)$$

Equation (6.35) predicted by the model is very similar to the empirical equation (6.6) which describes the experimental behavior. The only difference between the equation (6.35) and (6.6) is the non-zero intercept of 0.03. This is not surprising because equation (6.35) is not valid near the end of the transformation.

DeHoff [32] has shown that the total curvature of a tubule network is directly proportional to its length. Thus,

$$M_V^C(t) = K_M \cdot L_V(t) \quad (6.36)$$

where  $K_M$  is a shape factor.

From equations (6.33) and (6.36)

$$\frac{S_{V0}^C}{M_{V0}^C} = \frac{\{\text{Average cross-sectional perimeter}\}}{K_M} \quad (6.37)$$

Combining equations (6.33), (6.36) and (6.37) yields

$$\frac{M_V^C(t)}{M_{V0}^C} = \frac{S_V^C(t)}{S_{V0}^C} \quad (6.38)$$

Equation (6.38), predicted by the model, is very similar to the empirical equation (6.10) which describes the experimental behavior. The only difference between the two equations is the non-zero intercept of 0.02 in the equation (6.10). Again, this is not surprising because equation (6.38) is not valid near the end of the transformation.

The behavior of the distribution of linear intercepts of the cementite phase will now be analyzed. Since the cementite is in the form of a tubule network, a large number of the intersections of such a network with the plane of polish are expected to be along its cross-section (i.e. perpendicular to the tubule axis). Thus, the distribution of linear intercepts has a major contribution from the intercepts from the cross-section of the network. The change in the intercept distribution func-



tion with the austenitizing time is due to the change in the average dimension of the cross-section and the change in the length of the network itself. If the length of the network is decreased simply by removing some parts of the network (as in the case of one dimensional dissolution), then this will decrease the total number of intercepts (the decrease will be proportional to decrease in the surface area of the network). However, as the length of the network decreases, the frequency of intercepts will not change significantly. Thus, the frequency function is expected to be time invariant for a given starting structure. The observed experimental behavior is thus explained by the model.

#### 6.5.1 Analysis of the Global Properties of Austenite

It is observed that the austenite growth is inhibited across ferrite grain boundaries. This may be due to an orientation relationship between the austenite and ferrite grains. Judd and Paxton [120] found that the austenite grains have  $\{110\}_{\alpha}$  habit plane. The same orientation relationship was observed by Grozier, Paxton and Mullins [123] in the Fe-N system. The presence of an orientation relationship between the austenite and ferrite grains may also explain the observation that cementite is

not completely covered with austenite til about 50% transformation. It was also observed that the austenite grains grow preferentially along the ferrite grain boundaries. These observations suggest a plate-like growth of austenite along the ferrite grain boundaries. Thus, it is reasonable to assume that the austenite grows in a two dimensional manner along the ferrite grain boundaries. The extended volume fraction of austenite, for such a two dimensional plate-like growth, is given by

$$V_{ex}^{\gamma}(t) = \Delta \int_0^t A(t, \tau) \dot{N}(\tau) d\tau \quad (6.39)$$

where

$\Delta$  = thickness of the austenite plates

$A(t, \tau)$  = area of the flat surface of a plate  
nucleated at time  $\tau$

$t$  = total time for which the transformation  
has progressed

$\dot{N}(t)$  = extended nucleation rate of austenite

Note that for two dimensional growth the plate thickness,  $\Delta$ , does not change with time. Furthermore, for a given plate,  $\Delta$  is expected to be much smaller than the average dimension along the flat surfaces, soon after nucleation. Thus, one can write the following expression for the

extended surface area,  $S_{V_{ex}}^Y(t)$ , of austenite:

$$S_{V_{ex}}^Y(t) = 2 \int_0^t A(t, \tau) \dot{N}(\tau) d\tau \quad (6.40)$$

Combining equations (6.39) and (6.40) gives

$$V_{V_{ex}}^Y(t) = \frac{\Delta}{Z} S_{V_{ex}}^Y(t) \quad (6.41)$$

The relationship between the real volume fraction,  $V_V^Y(t)$ , and surface area,  $S_V^Y(t)$ , is given by the empirical equation (6.17) and it is as follows:

$$S_V^Y(t) = [1 - V_V^Y(t)] [B_2 V_V^Y(t) + B_3] \quad (6.15)$$

where  $B_2 = 7100 \text{ cm}^2/\text{cm}^3$  and  $B_3 = 250 \text{ cm}^2/\text{cm}^3$ . Equations (6.41) and (6.15) can now be used to evaluate the impingement function,  $\psi(V_V)$ . The procedure is described in section 3.5. The result is as follows:

$$\psi(V_V^Y) = (1 - V_V^Y)^2 \quad (6.42)$$

Also,

$$dV_V^Y = \psi(V_V^Y) dV_{V_{ex}}^Y$$

Thus,

$$\frac{V_V^Y(t)}{1 - V_V^Y(t)} = V_{V_{ex}}^Y(t) \quad (6.43)$$

Furthermore,

$$S_V^Y(t) = \psi(V_V^Y) \cdot S_{V_{ex}}^Y(t)$$

Hence,

$$\frac{S_V^Y(t)}{[1 - \bar{v}_V^Y(t)]^2} = S_{V_{ex}}^Y(t) \quad (6.44)$$

Using equations (6.43) and (6.44) together with the definition of the surface area averaged interface velocity gives

$$\bar{v}_S^Y = (\bar{v}_S^Y)_{ex} \quad (6.45)$$

In order to make quantitative predictions regarding the time variation of the global properties of austenite, a kinetic model will now be developed. The assumptions are as follows.

(1) The nucleation rate of austenite,  $\dot{N}(t)$ , can be described by the following functional form:

$$\dot{N}(t) = b_N t^m \quad (6.46)$$

where  $b_N$  is the kinetic parameter and it depends on temperature. The exponent  $m$  is a constant. For a constant nucleation rate,  $m = 0$ . If the nucleation rate increases with time, then  $m > 0$ . If the nucleation rate decreases with time, then  $m < 0$ . A large negative value of  $m$  would indicate site saturation.

(2) The two dimensional growth of austenite plates occurs (by definition) due to increase in the area of

their flat surfaces. In order to have a simple but flexible model, the following functional form is assumed to describe the rate of change of the area of flat surfaces,  $A(t, \tau)$ , of a plate nucleated at time  $\tau$ .

$$\left[\frac{dA}{dt}\right]_{\tau} = \frac{nb_G}{A^{n-1}} \quad (6.47)$$

or

$$A(t, \tau) = A(t - \tau) = b_G^{1/n} (t - \tau)^{1/n} \quad (6.48)$$

For a plate of circular shape and  $n = 1$ , equation (6.47) describes semi-infinite diffusion controlled growth. Note that  $b_G$  is a kinetic parameter that depends on temperature. The constant  $n$  is determined by the rate controlling mechanism.

Combining equations (6.48), (6.39) and (6.43) gives

$$\frac{V_V^Y(t)}{(1 - V_V^Y(t))} = \{\Delta b_N b_G^{1/n} \alpha_{mn}\} t^{(m + \frac{1}{n} + 1)} \quad (6.49)$$

where

$$\alpha_{mn} = \int_0^1 u^m [1 - u]^{1/n} du \quad (6.50)$$

Note that  $\alpha_{mn}$  is just a number and its value depends on  $m$  and  $n$ . Let

$$B_1^Y = \Delta b_N b_G^{1/n} \alpha_{mn} \quad (6.51)$$

Then,

$$\frac{V_V^Y(t)}{1-V_V^Y(t)} = B_1^Y t^{(m+\frac{1}{n}+1)} \quad (6.52)$$

Note that  $B_1^Y$  is independent of time but it depends on the temperature.

Equation (6.52), derived from the model, is very similar to the empirical equation (6.16) which describes the experimental behavior (see Figure 6.23). For comparison, equation (6.16) is rewritten as follows:

$$\frac{V_V^Y(t)}{1-V_V^Y(t)} = B_1^Y t^{2.25} \quad (6.16)$$

where  $B_1^Y = 5.75 \times 10^{-5} \text{ l/sec}^{2.25}$  at  $750^\circ\text{C}$ . Comparing equations (6.52) and (6.16) gives

$$m + \frac{1}{n} = 1.25 \quad (6.53)$$

and, at  $750^\circ\text{C}$ ,

$$\Delta b_N b_G^{1/n} \alpha_{mn} = 5.75 \times 10^{-5} \text{ l/(sec)}^{2.25} \quad (6.54)$$

Combining equations (6.48), (6.40), (6.44) and (6.53) gives

$$\frac{S_V^Y(t)}{[1-V_V^Y(t)]^Z} = S_{V_{ex}}^Y(t) = (2b_N b_G^{1/n} \alpha_{mn}) t^{2.25} \quad (6.55)$$

Thus, the model predicts that a plot of  $\log S_{V_{ex}}^Y(t)$  vs.

$\log t$  should be linear with a slope of 2.25. Such a plot for the experimental data is shown in Figure 6.25. The behavior is linear. The slope of the straight line is 2.16 which is very near to the value of 2.25 predicted by the model. The intercept of this plot gives

$$2b_N b_G^{1/n} \alpha_{mn} = 0.72 \quad (6.56)$$

Substituting equation (6.56) into (6.54) yields

$$\Delta = 1.6 \times 10^{-4} \text{ cm} \quad (6.57)$$

It is now possible to evaluate the surface area averaged interface velocity from the model. Using equations (6.55), (6.16) and (6.45) and the definition of  $\bar{v}_S$  gives

$$\bar{v}_S = \frac{1.8 \times 10^{-4}}{t} \text{ cm/sec} \quad (6.58)$$

Equation (6.58) is very similar to equation (6.18) obtained from the empirical equations (6.16) and (6.17).

The extended length of the  $\alpha\alpha\gamma$  triple lines,  $L_{V_{ex}}(t)$ , is given by

$$L_{V_{ex}}^{\alpha\alpha\gamma}(t) = K_L \int_0^t \{A(t, \tau)\}^{1/2} N(\tau) d\tau \quad (6.59)$$

where  $K_L$  is a shape factor, determined by the equation of the perimeter of the flat surfaces.

If the perimeter of the flat surfaces can be approxi-

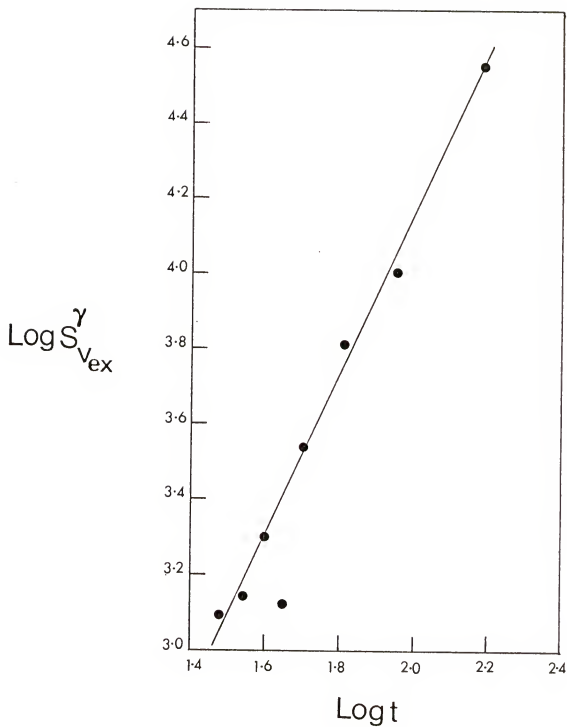


Figure 6.25. A graph of  $\text{Log } (S_{vex}^{\gamma})$  vs.  $\text{Log } t$  during the austenitization of the starting structure D<sub>3</sub> at 750°C.



mated by a circle, then  $K_L$  is equal to 3.54; for a square perimeter the value is 4.9. Combining equations (6.59), (6.48) and (6.46) gives

$$L_{V_{ex}}^{\alpha\alpha\gamma}(t) = \{K_L b_N b_G^{1/2n} \alpha_{m2n}\} t^{(m+\frac{1}{2n}+1)} \quad (6.60)$$

where

$$\alpha_{m2n} = \int_0^1 u^m [1-u]^{1/2n} du \quad (6.61)$$

Note that  $\alpha_{m2n}$  is just a number. Again,

$$L_V^{\alpha\alpha\gamma}(t) = (1-V_V^\gamma)^2 L_{V_{ex}}^{\alpha\alpha\gamma}(t) \quad (6.62)$$

Thus,

$$\frac{L_V^{\alpha\alpha\gamma}(t)}{[1-V_V^\gamma(t)]^2} = L_{V_{ex}}^{\alpha\alpha\gamma}(t) = \{K_L b_N b_G^{1/2n} \alpha_{m2n}\} t^{(m+\frac{1}{2n}+1)} \quad (6.63)$$

The model predicts that a plot of  $\text{Log}\{L_{V_{ex}}^{\alpha\alpha\gamma}(t)\}$  vs.  $\log t$  should be linear. Such a plot for the experimental data is shown in Figure 6.26. The plot is linear, as predicted by the model. The slope of the plot is 1.75. Thus,

$$m + \frac{1}{2n} + 1 = 1.75 \quad (6.64)$$

The intercept of the plot gives

$$K_L b_N b_G^{1/2n} \alpha_{m2n} = 2.344 \times 10^3 \quad (6.65)$$

Equations (6.64) and (6.53) give the following results.

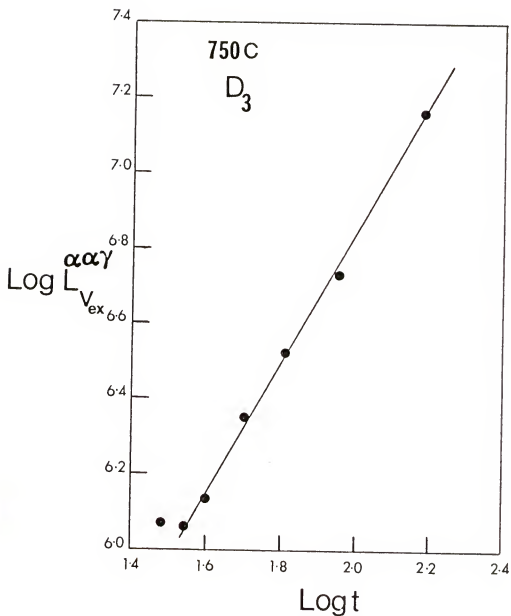


Figure 6.26. A graph of  $\text{Log } (L_{V_{ex}}^{\alpha\alpha\gamma})$  vs.  $\text{Log } t$  during the austenitization of the starting structure D<sub>3</sub> at 750°C.

$$\begin{aligned} n &= 1.0 \\ m &= 0.25 \end{aligned} \quad (6.66)$$

Since the values of  $m$  and  $n$  are now known,

$$\begin{aligned} \alpha_{mn} &= \alpha_{0.25,1} = \int_0^1 u^{0.25} (1-u) du = 0.36 \\ \{ \alpha_{m2n} &= \alpha_{0.25,2} = \int_0^1 u^{0.25} (1-u)^{1/2} du \approx 0.5 \} \end{aligned} \quad (6.67)$$

It is now possible to evaluate  $b_N$  and  $b_G$  if the value of the shape factor,  $K_L$ , is known. As indicated earlier,  $K_L$  is equal to 3.54 for a circle and 4.9 for a square. For an ellipse, the value of  $K_L$  varies from 3.54 to 7.95 as the axial ratio varies from one to ten. Thus, the choice of the value of  $K_L$  does not seem to have a significant effect on the calculated values of  $b_N$  and  $b_G$ . Accordingly, it will be assumed that  $K_L$  is equal to 3.54. Using this value of  $K_L$  together with the equations (6.65), (6.54) and (6.67) gives

$$\begin{aligned} b_N &= 1.8 \times 10^6 \\ \{ b_G &= 5.7 \times 10^{-7} \} \end{aligned} \quad (6.68)$$

All the parameters of the model are now known and their values at 750°C are as follows:

$$\begin{aligned}
m &= 0.25 \\
n &= 1.0 \\
\left\{ \begin{array}{l} \Delta = 1.6 \times 10^{-4} \text{ cm} \\ K_L = 3.54 \end{array} \right. & \quad (6.69) \\
b_N &= 1.8 \times 10^6 \text{ (cm)}^{-3} \cdot \text{(sec)}^{-5/4} \\
b_G &= 5.7 \times 10^{-7} \text{ cm}^2/\text{sec}
\end{aligned}$$

It is now possible to predict the coverage of the ferrite grain boundaries by the austenite grains. Since the austenite growth occurs in a two dimensional fashion along the ferrite grain boundaries, the "extended" coverage of the ferrite grain boundaries should be approximately equal to half of the extended surface area of the austenite plates. Thus,

$$\frac{S_{V_0}^{\alpha\alpha} - S_V^{\alpha\alpha}}{(1-V_V^Y)^2} = [b_N b_G^{\alpha_{0.25,1}}] t^{2.25} \quad (6.70)$$

Substituting the values of the parameters  $b_N$ ,  $b_G$  and  $\alpha_{0.25,1}$  gives

$$\frac{S_{V_0}^{\alpha\alpha} - S_V^{\alpha\alpha}}{(1-V_V^Y)^2} = 0.36 t^{2.25} \quad (6.71)$$

or

$$\log \left\{ \frac{S_{V_0}^{\alpha\alpha} - S_V^{\alpha\alpha}}{(1-V_V^Y)^2} \right\} = 2.25 \log t - 0.44 \quad (6.72)$$

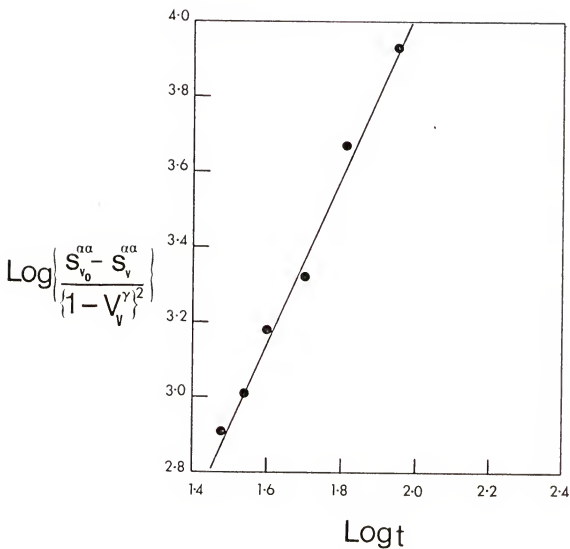


Figure 6.27. A graph of  $\text{Log} \left[ \frac{S_v^{\alpha\alpha} - S_v^{\alpha\alpha}}{(1 - V_v^{\gamma})^2} \right]$  vs.  $\text{Log } t$  during the austenitization of the starting structure D<sub>3</sub> at 750°C.

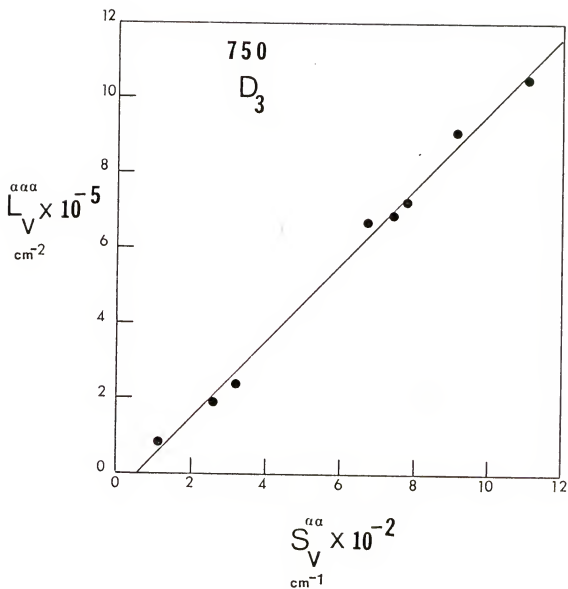


Figure 6.28. A graph of  $L_V^{\alpha\alpha}$  vs.  $S_V^{\alpha\alpha}$  during the austenitization of the starting structure D<sub>3</sub> at 750°C.

The model predicts that a plot of  $\log\{S_V^{\alpha\alpha} - S_V^{\alpha\alpha} / (1 - V_V^Y)^2\}$  vs.  $\log t$  should be linear with a slope of 2.25 and the intercept should be -0.44. Such a plot for the experimental data is shown in Figure 6.27. The plot is linear with the slope of 2.26 and the intercept of -0.48. Thus the agreement between the prediction of the model and the experimental behavior is very good.

The present model assumes that the austenite growth occurs predominantly along the ferrite grain boundaries. In such a case, the length of the ferrite grain edges consumed by the austenite grains should be directly proportional to the area of the ferrite grain boundaries consumed by austenite. Thus, the length of the ferrite grain edges,  $L_V^{\alpha\alpha}(t)$ , should vary linearly with the surface area of the ferrite grain boundaries,  $S_V^{\alpha\alpha}(t)$ , during the process. Figure 6.28 shows a plot of  $L_V^{\alpha\alpha}(t)$  vs.  $S_V^{\alpha\alpha}(t)$  for the experimental data. The behavior is linear, as predicted by the model.

The model developed in this section explains the experimentally observed behavior during the austenitization process.

## 6.6 Conclusions:

(1) "Spherodized" cementite is in the form of an incomplete grain edge network.

(2) During the austenitization process the dissolution of the cementite network takes place in a one dimensional manner.

(3) Austenite growth occurs along the ferrite grain boundaries.

(4) Austenite grains grow in a two dimensional fashion. The rate of growth of an austenite plate can be described by the rate of change of the area of its flat surfaces. The mathematical form is as follows:

$$\left(\frac{dA}{dt}\right)_\tau = b_G$$

where A is the area of the flat surface of an austenite plate. The parameter  $b_G$  is independent of time but it depends on the austenitizing temperature. At 750°C,  $b_G$  is equal to  $5.7 \times 10^{-7} \text{ cm}^2/\text{sec}$ .

(5) The nucleation rate of austenite increases with time and it can be described by the following functional form:

$$\dot{N}(t) = b_N t^{1/4}$$

where the kinetic parameter,  $b_N$ , is a function of temperature but independent of time. At 750°C,  $b_N$  is equal to  $1.8 \times 10^6 \text{ per cm}^3 (\text{sec})^{1.25}$ .

(6) The approach developed in the third chapter has been successfully used to interpret the experimental data.



It is interesting to note that the approach successfully explains the experimentally observed behavior of nine independent stereological properties in a quantitative manner. To the best knowledge of the author, this has never been done before and it clearly demonstrates the potential and practical feasibility of the approach.

## CHAPTER VII CONCLUSIONS AND SUMMARY

(1) It is possible to evaluate the global properties of an evolving microstructure from a given description of the local variables. The approach provides a means for a systematic analysis of the quantitative microscopic data on the kinetics of phase transformations.

(2) A flexible but simple model has been developed to evaluate the global properties of a growing phase during a phase transformation.

(3) A technique has been developed to deduce the nucleation rate and growth rate from the time variation of the global properties.

(4) The effects of various growth geometries on the kinematics of phase transformations have been explored in detail. It is shown that the hyperbolic time dependence of the average interface velocities (observed in recrystallization studies) may be just due to the two or one dimensional nature of the growth process.

(5) Impingement equations have been developed for non-random impingement. A phenomenological approach has been developed to evaluate the impingement function for two dimensional and one dimensional growth processes.

(6) A generalized continuity equation has been derived.

(7) An algorithm is developed for the prediction of the evolution of the size distribution during a dissolution process.

(8) The theoretical analysis is applied to the experimental data of other research workers on the kinetics of the recrystallization process. Every qualitative and quantitative experimental observation is explained by using the present approach. It is concluded that the recrystallized grain size (as reported by the line intercept count) will be independent of the annealing temperature if the recrystallized regions grow in a two dimensional or one dimensional manner.

(9) The kinetics of austenitization of a pearlitic structure was studied at three temperatures. The volume fraction and surface area of austenite was measured at various times during the process. The nucleation rate and growth rate of austenite was deduced from the observed time variation of the volume fraction and surface area of austenite. It is concluded that the process takes place by a constant nucleation rate and constant growth rate of austenite.

(10) A detailed quantitative microscopic investi-

gation was carried out on the austenitization of three different spherodized cementite structures. The experiments were done at three austenitizing temperatures.

(11) The "spherodized" cementite is shown to be present in the form of an incomplete grain edge network. During the austenitization process the cementite network dissolves in a one dimensional manner. The austenite grows by a two dimensional growth along the ferrite grain boundaries. The local growth rate of austenite can be described by a parabolic time law. The nucleation rate of austenite increases with the austenitizing time and it is directly proportional to  $t^{\frac{1}{4}}$ .

(12) The present approach is successfully applied to explain the experimentally observed behavior of nine independent stereological properties during the austenitization of the "spherodized" cementite structures.

## BIBLIOGRAPHY

- [1] R. L. Cairns: Met. Trans., 1974, Vol. 5, p. 1677.
- [2] F. V. Nolfi, P. G. Shewmon and J. S. Foster: Trans. Met. Soc. AIME, 1969, Vol. 245, p. 1427.
- [3] D. E. Coates: Met. Trans., 1972, Vol. 3, p. 1203.
- [4] F. S. Ham: Quart. Appl. Math., 1959, Vol. 17, p. 137.
- [5] G. Horvay and J. W. Cahn: Acta. Met., 1961, Vol. 9, p. 695.
- [6] C. Zener: J. Appl. Phys., 1949, Vol. 20, p. 950.
- [7] F. C. Frank: Proc. Roy. Soc., 1950, Vol. A201, p. 586.
- [8] B. Aaron et al.: J. Appl. Phys., 1970, Vol. 41, p. 4404.
- [9] G. Meyrick and G. W. Powell: Annual Reviews of Materials Science, 1973, Vol. III, p. 327.
- [10] G. R. Purdy: Metallography, 1975, Vol. 8, p. 131.
- [11] H. I. Aaronson, H. B. Aaron and K. R. Kinsman: Metallography, 1971, Vol. 4, p. 1.
- [12] F. Chayes: Mineral. Mag. (London), 1953, Vol. 30, p. 147.
- [13] A. Johannsen: J. Geol., 1919, Vol. 27, p. 276.
- [14] A. D. Hally: Quart. J. Micr. Sci., 1964, Vol. 105, p. 503.
- [15] H. Elias and J. C. Sherrick: Morphology of the Liver, 1968, Academic Press (New York).

- [16] D. A. Aboav and T. G. Langdon: Metallography, 1969, Vol. 1, p. 333.
- [17] G. W. Lord and T. F. Willis: ASTM Bulletin, 1951, Vol. 177, p. 56.
- [18] J. H. Steel, Jr., G. Ifju and J. A. Johnson: Proceedings of Fourth International Congress for Stereology (edited by E. E. Underwood), NBS Publication, 1976, p. 245.
- [19] A. Delesse: Ann. des. Mines., 1848, Vol. 13, p. 379.
- [20] R. T. DeHoff and F. N. Rhines: Quantitative Microscopy, McGraw-Hill, 1968.
- [21] J. E. Hilliard: Volume Fraction Analysis by Quantitative Metallography, Rep. No. 61-RL-2652 M, General Electric Research Lab., March, 1961.
- [22] S. A. Saltykov: Stereometric Metallography, Second Edition, 1958, Metallurgizdat, Moscow, 1958.
- [23] E. R. Weibel: Morphometry of the Human Lung, 1963, Springer-Verlag (Berlin), p. 12.
- [24] F. Chayes: Pertographic Modal Analysis, 1956, John Wiley (New York), pp. 5, 14, 29.
- [25] A. Rosiwal: Verhandl. der K. K. Gelogischen Reichanstalt, 1898, Vol. 516, p. 143.
- [26] E. E. Underwood: Quantitative Stereology, 1970, Addison-Wesley Publishing Co.
- [27] P. A. P. Moran and M. G. Kendall: Geometric Probabilities, 1963, Hafner (New York).
- [28] C. S. Smith and L. Guttman: Trans. Met. Soc. AIME, 1953, Vol. 197, p. 81.
- [29] J. E. Hilliard: Trans. Met. Soc. AIME, 1962, Vol. 224, p. 1201.
- [30] J. E. Hilliard: Proceedings of Second International Congress for Stereology (Edited by H. Elias), 1967, Springer Verlag (New York), p. 219.

- [31] D. J. Struik: Lectures on Classical Differential Geometry, 1950, Addison-Wesley (New York).
- [32] R. T. DeHoff: Private communication.
- [33] F. N. Rhines, R. T. DeHoff and R. A. Rummel: Topological Model for a Sintering Process, AEC Contract No. AT-(40-1)-2851, Annual Report, 1962.
- [34] R. T. DeHoff: Trans. Met. Soc. AIME, 1967, Vol. 239, p. 617.
- [35] J. W. Cahn: Trans. Met. Soc. AIME, 1967, Vol. 239, p. 611.
- [36] R. T. DeHoff: Quantitative Determination of the Structure Property Relationships in Nuclear Fuel Element Materials, AEC Contract No. AT-(40-1)-4212, Final Report, 1975.
- [37] D. Harker and E. A. Parker: Trans. Met. Soc. AIME, 1945, Vol. 34, p. 156.
- [38] S. D. Wicksell: Biometrika, 1925, Vol. 17, p. 84.
- [39] E. Scheil: Z. Metallk., 1935, Vol. 27, p. 199.
- [40] E. Scheil: Z. Anorg. Allgem. Chem., 1931, Vol. 201, p. 259.
- [41] H. A. Schwartz: Metal Alloys, 1934, Vol. 5, p. 139.
- [42] R. V. Churchill: Operational Mathematics, McGraw-Hill Company, 1958.
- [43] R. T. DeHoff: Trans. Met. Soc. AIME, 1962, Vol. 224, p. 474.
- [44] Cruz Orive: to be published in Journal of Applied Physics.
- [45] R. T. DeHoff and S. M. Gehl: Proceedings of the Fourth International Congress for Stereology (Edited by E. E. Underwood), NBS Publication, 1976, p. 29.

- [46] S. D. Wicksell: Biometrika, 1926, Vol. 18, p. 151.
- [47] W. A. Johnson: Metal Prog., 1946, Vol. 49, p. 87.
- [48] H. D. Lewis, K. L. Walters and K. A. Johnson: Metallography, 1973, Vol. 6, p. 93.
- [49] A. G. Spektor: Zavod. Lab., 1950, Vol. 16(2), p. 173.
- [50] J. W. Cahn and R. L. Fullman: Trans. Met. Soc. AIME, 1956, Vol. 206, p. 610.
- [51] R. T. DeHoff and P. Bousquet: Journal of Microscopy, 1970, Vol. 92(2), p. 119.
- [52] H. E. Exner and H. L. Lucas: Metallography, 1971, Vol. 4, p. 325.
- [53] H. Itoh: Metallography, 1970, Vol. 4, p. 407.
- [54] H. E. Exner: Z. Metallk., 1966, Vol. 57, p. 755.
- [55] W. L. Nicholson: Biometrika, 1970, Vol. 57, p. 273.
- [56] R. M. Diwan: Ph.D. Thesis, University of Florida, 1974.
- [57] J. W. Woodhead: Metallography, 1968, Vol. 1, p. 35.
- [58] R. T. DeHoff: Trans. Met. Soc. AIME, 1971, Vol. 2, p. 521.
- [59] R. W. Heckel and R. L. Degregrio: Trans. Met. Soc. AIME, 1965, Vol. 223, p. 2001.
- [60] H. Kahn and L. A. Girifalco: J. Phys. Chem. Solids, 1975, Vol. 36, p. 919.
- [61] T. Mukherjee, W. E. Stumpf, C. M. Sellers and W. C. McTegart: J.I.S.I., 1969, Vol. 207, p. 621.
- [62] I. M. Lifshitz and V. V. Slyozov: J. Phys. Chem. Solids, 1961, Vol. 19, p. 35.



- [63] A. J. Markworth: Metallography, 1970, Vol. 3, p. 197.
- [64] F. G. Yost: Met. Trans., 1975, Vol. 6A, p. 1607.
- [65] A. G. Spektor: Plant. Lab., 1949, Vol. 15, no. 7.
- [66] A. G. Spektor: Plant. Lab., 1956, Vol. 22, no. 12.
- [67] R. T. DeHoff: "The Dynamics of Microstructural Change" in Treatise on Materials Science and Technology, Vol. 1, Academic Press (New York), 1972, p. 247.
- [68] J. W. Cahn: Trans. Met. Soc. AIME, 1967, 1967, Vol. 239, p. 611.
- [69] A. N. Kolmogorov: Bull. Acad. Sci. USSR, 1937, no. 3.
- [70] M. Avrami: J. Chem. Phys., 1939, Vol. 7, p. 1103.
- [71] W. A. Johnson and R. F. Mehl: Trans. Met. Soc. AIME, 1939, Vol. 135, p. 416.
- [72] J. P. Serra: Proceedings of Fourth International Congress for Stereology (Edited by E. E. Underwood), NBS Publication, 1976, p. 83.
- [73] J. W. Cahn and W. C. Hagel: Acta Met., 1963, Vol. 11, p. 561.
- [74] R. L. Fullman: Trans. Met. Soc. AIME, 1953, Vol. 197, p. 447.
- [75] J. E. Hilliard: "Applications of Quantitative Metallography in the Recrystallization Studies" in Recrystallization Grain Growth and Textures, ASM Publication, 1966.
- [76] S. Chandrasekhar: Rev. Mod. Phys., 1943, Vol. 15, p. 674.
- [77] P. Hertz: Math. Ann., 1909, Vol. 67, p. 387.
- [78] J. L. Meijering: Phil. Res. Rep., 1953, Vol. 8, p. 270.

- [79] G. R. Speich and R. M. Fisher: "Recrystallization of a rapidly heated 3½% Silicon Steel" in Recrystallization, Grain Growth and Textures, ASM Publication, 1966, p. 563.
- [80] R. V. Churchill: Operational Mathematics, McGraw-Hill, 1972, p. 3.
- [81] ibid, p. 14.
- [82] ibid, p. 45.
- [83] ibid, p. 53.
- [84] Brice Carnahan, H. A. Luther and J. O. Wilkes: Applied Numerical Methods, John Wiley and Sons, Inc. (New York), 1969, p. 138.
- [85] N. F. Mott: Proc. Phys. Soc., 1948, Vol. 60, p. 391.
- [86] D. Turnbull: Trans. Met. Soc. AIME, 1951, Vol. 191, p. 661.
- [87] R. A. Vandermeer and P. Gordon: Trans. Met. Soc. AIME, 1959, Vol. 215, p. 577.
- [88] W. C. Leslie: Trans. Met. Soc. AIME, 1961, Vol. 221, p. 752.
- [89] E. P. Abrahamson and B. S. Blakeney: Trans. Met. Soc. AIME, 1960, Vol. 218, p. 1101.
- [90] M. Hillert: Acta Met., 1971, Vol. 19, p. 769.
- [91] D. Turnbull: Acta Met., 1955, Vol. 3, p. 55.
- [92] A. T. English and W. A. Backofen: Trans. Met. Soc. AIME, 1964, Vol. 230, p. 396.
- [93] W. C. Leslie, F. J. Plecity and J. T. Michalak: Trans. Met. Soc. AIME, 1961, Vol. 221, p. 691.
- [94] W. C. Leslie, F. J. Plecity and F. W. Aul: Trans. Met. Soc. AIME, 1961, Vol. 221, p. 982.

- [95] Recrystallization, Grain Growth and Textures, ASM Monograph, 1966.
- [96] L. Himmel: Recovery and Recrystallization of Metals, AIME and Interscience Publishers, Inc. (New York), 1963.
- [97] R. F. Mehl: "Recrystallization" in ASM Metals Handbook, ASM, Metals Park, Ohio, 1948.
- [98] P. Gordon and R. A. Vandermeer: Trans. Met. Soc. AIME, 1962, Vol. 224, p. 917.
- [99] K. Lücke and K. Detert: Acta Met., 1957, vol. 5, p. 629.
- [100] K. T. Aust and J. W. Rutter: Trans. Met. Soc. AIME, 1959, Vol. 215, p. 119.
- [101] J. W. Cahn: Acta Met., 1962, Vol. 10, p. 789.
- [102] P. Gordon: Energetics in Metallurgical Phenomena, Vol. 1, New York, 1962, p. 207.
- [103] J. W. Cahn: Acta Met., 1956, Vol. 4, p. 449.
- [104] J. W. Cahn and W. Hagel in Decomposition of Austenite by Diffusional Processes, Interscience (New York), 1960.
- [105] G. A. Roberts and R. F. Mehl: Trans. Met. Soc. AIME, Vol. 31, p. 613.
- [106] G. R. Speich and A. Szirmai: Trans. Met. Soc. AIME, 1969, Vol. 245, p. 1063.
- [107] B. Karlson: Z. Metallk., 1972, Vol. 63, p. 160.
- [108] E. Ereemeev: Russ. Met., 1969, Vol. 3, p. 85.
- [109] Shushi Kinoshita and Takeshi Veda: Trans. Iron Steel Inst. of Japan, 1974, Vol. 14, p. 411.
- [110] S. F. Dirnfield and B. M. Korevaar: 14<sup>th</sup> Int. Colloq. on Heat Treating, 1972, p. 10.


- [111] J. Orlich: Traitmet Thermique, 1974, Vol. 90, p. 69.
- [112] V. V. Burdin: Phys. Met. and Metall., 1973, Vol. 35(3), p. 94.
- [113] H. W. Paxton: Transformation and Hardenability in Steels, published by Molybdenum Corp., 1967, p. 3.
- [114] W. H. Brandt: J. Appl. Phys., 1945, Vol. 16, p. 139.
- [115] C. Zener: Trans. Met. Soc. AIME, 1946, Vol. 167, p. 550.
- [116] G. R. Speich and M. J. Richards: Trans. Met. Soc. AIME, 1969, Vol. 245, p. 1073.
- [117] E. C. Bain: Functions of Alloying Elements in Steels, ASM Publication, 1939, p. 101.
- [118] G. Molinder: Acta Met., 1956, Vol. 4, p. 565.
- [119] S. Neidzweidz, Y. Partom, A. Taub and B. Weiss: ASM Trans. Quart., 1965, Vol. 58, p. 253.
- [120] R. R. Judd and H. W. Paxton: Trans. Met. Soc. AIME, 1968, Vol. 242, p. 206.
- [121] A. Sauveur: Metallography and Heat Treatment of Iron and Steel, McGraw-Hill Publishing Co., 1935, p. 482.
- [122] R. T. DeHoff: Private communication.
- [123] J. D. Grozier, H. W. Paxton and W. W. Mullins: Trans. Met. Soc. AIME, 1965, Vol. 233, p. 130.

## BIOGRAPHICAL SKETCH


Arun Mahadeo Gokhale was born on April 28, 1948 in Baroda, India. The author began his undergraduate work at the Indian Institute of Technology, Kanpur, in July, 1965, and received a degree of Bachelor of Technology in Metallurgical Engineering in June, 1970. He joined the Department of Metallurgical Engineering at the Indian Institute of Technology, Kanpur, in July 1970, as a post graduate student and received a degree of Master of Technology in Metallurgical Engineering in June, 1972. He joined the Department of Materials Science and Engineering at the University of Florida in September, 1972, to pursue the degree of Doctor of Philosophy.

The author is married to the former Sulabha Joshi from Baroda.


I certify that I have read this study and that in my opinion it conforms to acceptable standards of scholarly presentation and is fully adequate, in scope and quality, as a dissertation for the degree of Doctor of Philosophy.

  
Robert T. DeHoff / Chairman  
Professor of Materials Science  
and Engineering

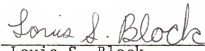
I certify that I have read this study and that in my opinion it conforms to acceptable standards of scholarly presentation and is fully adequate, in scope and quality, as a dissertation for the degree of Doctor of Philosophy.

  
John J. Hren  
Professor of Materials Science  
and Engineering


I certify that I have read this study and that in my opinion it conforms to acceptable standards of scholarly presentation and is fully adequate, in scope and quality, as a dissertation for the degree of Doctor of Philosophy.

  
Albert G. Guy  
Professor of Materials Science  
and Engineering

I certify that I have read this study and that in my opinion it conforms to acceptable standards of scholarly presentation and is fully adequate, in scope and quality, as a dissertation for the degree of Doctor of Philosophy.


  
Louis S. Block  
Professor of Mathematics

I certify that I have read this study and that in my opinion it conforms to acceptable standards of scholarly presentation and is fully adequate, in scope and quality, as a dissertation for the degree of Doctor of Philosophy.

  
Robert W. Gould  
Professor of Materials Science  
and Engineering

This dissertation was submitted to the Graduate Faculty of the College of Engineering and to the Graduate Council, and was accepted as partial fulfillment of the requirements for the degree of Doctor of Philosophy.

March, 1977

  
Dean, College of Engineering

\_\_\_\_\_  
Dean, Graduate School